Chem Soc Rev

REVIEW ARTICLE

View Article Online
View Journal | View Issue

Cite this: *Chem. Soc. Rev.*, 2019, **48**, 1194

Barium titanate at the nanoscale: controlled synthesis and dielectric and ferroelectric properties

Beibei Jiang, James Iocozzia, Lei Zhao, Hefeng Zhang, Yeu-Wei Harn, Yihuang Chen and Zhiqun Lin *

Received 31st August 2018

DOI: 10.1039/c8cs00583d

rsc.li/chem-soc-rev

The current trend in the miniaturization of electronic devices has driven the investigation into many nanostructured materials. The ferroelectric material barium titanate ($BaTiO_3$) has garnered considerable attention over the past decade owing to its excellent dielectric and ferroelectric properties. This has led to significant progress in synthetic techniques that yield high quality $BaTiO_3$ nanocrystals (NCs) with well-defined morphologies (*e.g.*, nanoparticles, nanorods, nanocubes and nanowires) and controlled crystal phases (*e.g.*, cubic, tetragonal and multi-phase). The ability to produce nanoscale $BaTiO_3$ with controlled properties enables theoretical and experimental studies on the intriguing yet complex dielectric properties of individual $BaTiO_3$ NCs as well as $BaTiO_3$/polymer nanocomposites. Compared with polymer-free individual $BaTiO_3$ NCs, $BaTiO_3$/polymer nanocomposites possess several advantages. The polymeric component enables simple solution processibility, high breakdown strength and light weight for device scalability. The $BaTiO_3$ component enables a high dielectric constant. In this review, we highlight recent advances in the synthesis of high-quality $BaTiO_3$ NCs *via* a variety of chemical approaches including organometallic, solvothermal/hydrothermal, templating, molten salt, and sol–gel methods. We also summarize the dielectric and ferroelectric properties of individual $BaTiO_3$ NCs and devices based on $BaTiO_3$ NCs *via* theoretical modeling and experimental piezoresponse force microscopy (PFM) studies. In addition, viable synthetic strategies for novel $BaTiO_3$/polymer nanocomposites and their structure–composition–performance relationship are discussed. Lastly, a perspective on the future direction of nanostructured $BaTiO_3$-based materials is presented.

School of Materials Science and Engineering, Georgia Institute of Technology, Atlanta, GA 30332, USA. E-mail: zhiqun.lin@mse.gatech.edu

Beibei Jiang

Dr Beibei Jiang received her PhD in Materials Science and Engineering from the Georgia Institute of Technology in December 2016 under the guidance of Professor Zhiqun Lin. Her dissertation research at Georgia Tech is focused on designing polymer-enabled functional polymer–inorganic nanocomposites for improving the performance of Li-ion batteries, capacitors, and ferroelectric devices. Her research interest is focused on analyzing the failure mechanisms of various types of devices including Li-ion batteries, capacitors and thin film transistors as well as designing and synthesizing new materials and new structures for improving the stability of material structure, interface, and overall device structure. These efforts aim to improve the overall performance and prevent the failure of energy devices.

James Iocozzia

Dr James Iocozzia received his PhD in Materials Science and Engineering from the Georgia Institute of Technology in August 2018 under the guidance of Professor Zhiqun Lin. His research interests include nanocomposites, block copolymers and hyperbranched polymer systems for the development of functional hard and soft organic/inorganic nanomaterials in the areas of drug delivery, electronics, energy and stimuli-responsive materials. James has authored or co-authored more than 30 papers in the fields of polymers and energy materials.

1. Introduction

Owing to its excellent dielectric and ferroelectric properties, $BaTiO_3$ is one of the most extensively studied ferroeletric materials and is currently utilized in a wide variety of fields including multilayer capacitors,[1–3] transducers,[4–8] actuators,[8–10] electro-optical devices,[11–13] electromechanical devices,[14–17] dynamic random-access memory,[18–21] field-effect transistors,[22–25] and thermistors,[26–29] among others. Since the discovery of $BaTiO_3$ ferroelectricity by Wul and Goldman in 1945, the bulk physical properties and crystal structure of $BaTiO_3$ have been intensely investigated.[30–33] Bulk $BaTiO_3$ primarily exists in four crystal phases including cubic, tetragonal, orthorhombic, and rhombohedral (Fig. 1).[30] At high temperatures ($T > 120$ °C), it possesses the classic perovskite structure (*i.e.*, cubic phase), in which Ba^{2+} and O^{2-} ions together form the FCC lattice while the smaller Ti^{4+} cation resides in the octahedral interstitial sites, forming $[TiO_6]$ in the FCC array. This cubic phase structure is highly symmetric with the cation and anion centers coinciding with each other, leading to no polarization in the crystal structure and thus no ferroelectricity (*i.e.*, paraelectric). When T is lowered to below 120 °C, the cubic symmetric structure turns to a nonsymmetric structure, accompanied with the deviation of the cation center from the anion center, resulting in a net spontaneous polarization in the crystal structure and the transition from paraelectric to ferroelectric phase (Fig. 1). When T is between 120 °C and 5 °C, $BaTiO_3$ exhibits the tetragonal structure where the Ti^{4+} cation deviates from the center of the $[TiO_6]$ octahedron, leading to a net polarization along the [001] edge direction due to the displacement of the cation center from the anion center.

Lei Zhao

Dr Lei Zhao is a senior scientist in Baker Hughes, Inc., specialized in advanced composite materials for oil and gas industry application. He holds a PhD degree in materials science and engineering from Iowa State University. Lei has published over 20 papers in materials science journals in the area of polymer science and nanostructured materials, and filed 20 patents on carbon composite materials and metallic composites used in downhole seal and joining. Before joining Baker Hughes in 2013, he worked in Argonne National laboratory as a post doc in developing metallic nanocomposite materials for next generation electric vehicles.

Hefeng Zhang

Dr Hefeng Zhang received his PhD in Polymer Chemistry and Physics under the supervision of Professor Junpo He at Fudan University in 2012 where he worked on the precision synthesis and characterization of non-linear polymers. He pursued postdoctoral work on polyethylene molecular engineering under the direction of Professor Nikos Hadjichristidis at King Abdullah University of Science and Technology (2012–2015) and uniform nanomaterial synthesis under the guidance of Professor Zhiqun Lin at the Georgia Institute of Technology (2015–2016). In 2017, Hefeng Zhang joined Shantou University as a professor. His research interests include well-defined complex polymer synthesis, inorganic nanomaterial–polymer hybrid fabrication, natural polymer modification and organocatalysis.

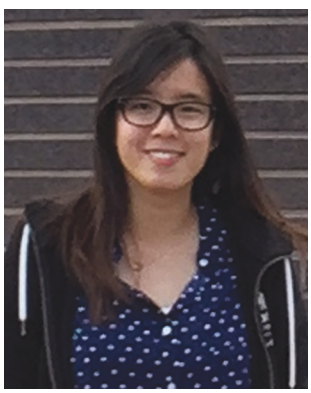

Yeu-Wei Harn

Yeu-Wei Harn received her bachelor's degree in a double specialty program of Management and Technology with double specialties in materials science and engineering as well as quantitative finance in 2013 and her master degree in materials science and engineering in 2015, both from the National Tsing Hua University, Taiwan. She joined the Georgia Institute of Technology to pursue her PhD in materials science and is currently working as a graduate researcher under Professor Zhiqun Lin. Her work focuses on using soft star-like block copolymers as templates to synthesize nanoparticles and the subsequent investigation of their properties.

Yihuang Chen

Dr Yihuang Chen is a postdoctoral fellow in Professor Zhiqun Lin's group at the Georgia Institute of Technology. He received his PhD in Materials Science and Engineering from the South China University of Technology in 2017. Previously, he was a visiting graduate student in Professor Zhiqun Lin's group from 2014. His research interests center on the synthesis of responsive polymers, functional polymer brushes and polymer/inorganic nanocrystal hybrids.

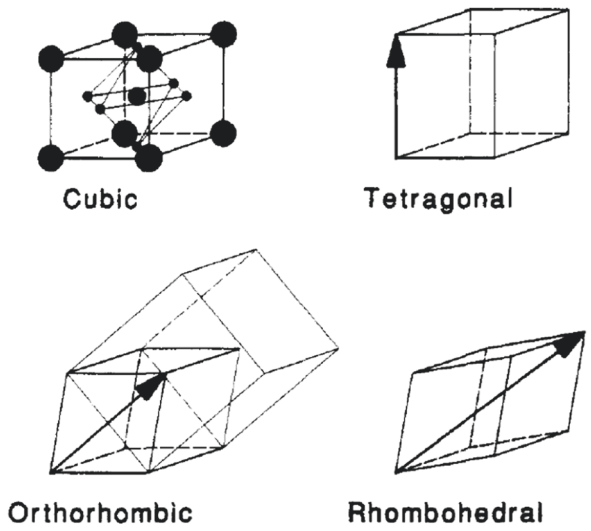

Fig. 1 Schematic representation of the four different crystalline structures of $BaTiO_3$. Among them, the cubic phase is paraelectric, while the tetragonal, orthorhombic and rhombohedral phases are ferroelectric. Reproduced with permission.[30] Copyright 1993, American Chemical Society.

With further cooling to between 5 °C and −90 °C, the structure converts to the orthorhombic phase, which can be regarded as the elongation of the cubic unit cell along the [011] face diagonal direction. Lastly, onset of the rhombohedral phase occurs at $T < -90$ °C, which corresponds to the elongation of the cubic unit cell along the [111] body diagonal direction. Distortions along these directions result in nonsymmetry in the crystal structure with the cation center deviating from the anion center, leading to ferroelectric phases with a net spontaneous polarization. Research on nanoscopic ferroelectric $BaTiO_3$ synthesis and property investigation has received much attention. The ability to manipulate the properties of nanostructured ferroelectric materials is essential to developing molecular electronics such as random access memory[34] and logic circuitry.[35,36] Similar to many well-established nanocrystals (NCs) systems (*e.g.*, quantum dots,[37–40] and magnetic NCs[41–43]), $BaTiO_3$ NCs behave differently from both their bulk counterparts and their dielectric and ferroelectric properties exhibit heavy dependency on the crystal size (*i.e.*, size effect).[44–47] Owing to the rapid progress in advanced synthetic techniques for producing myriad high-quality NCs with controllable structures and dimension, both theoretical and experimental studies are made possible for studying the effect of structure and dimension on dielectric and ferroelectric properties. To date, a diverse group of $BaTiO_3$ nanostructures (*e.g.*, nanodots,[48,49] nanoparticles,[50] nanobowls,[51] nanorods,[52] nanocubes,[53] and nanowires[54]) with different crystalline phases (*e.g.*, cubic,[55,56] tetragonal,[28] or multi-crystalline[57]) have been produced through various chemical approaches (*e.g.* organometallic,[49,54] solvothermal/hydrothermal,[48,51–53] templating,[55–57] molten salt,[55,58] and sol–gel methods[59,60]). In addition, a lot of developments have been made in the exploration of the effects of the size, shape, microstructure, and surface conditions (*e.g.* surface defects and capping ligands) of $BaTiO_3$ NCs on their dielectric and ferroelectric properties with the utilization of many advanced characterization methods such as piezoresponse force microscopy (PFM),[61–63] neutron scattering,[64–67] and electron microscopy.[68–71] To further elucidate the underlying mechanism of the dielectric and ferroelectric behavior of $BaTiO_3$ at the nanoscale, several models have been proposed.[72–74] Moreover, the practical application of $BaTiO_3$/polymer nanocomposites requires that the $BaTiO_3$ NCs can be homogeneously dispersed within the polymer matrix without phase separation or particle agglomeration. This has triggered recent significant research efforts into the development of surface modification techniques that enable high-quality $BaTiO_3$/polymer nanocomposites with uniform dispersion and favorable morphology as compared to traditional simple mixing approaches.

This review aims to summarize the recent achievements in the following aspects of $BaTiO_3$ nanomaterial research: chemical synthesis of individual $BaTiO_3$ NCs, ferroelectric properties of individual $BaTiO_3$ NCs by PFM characterization, $BaTiO_3$ thin film preparation and characterization, $BaTiO_3$-based organic/inorganic nanocomposites and their dielectric performance. Within each part, a representative sampling of examples are provided to illustrate (1) $BaTiO_3$ NCs with well-defined morphologies and chemical compositions enabled by controlled synthesis; (2) the structure–property relationship (*i.e.*, how the crystal structure, shape, and processing history affect the dielectric and ferroelectric properties); (3) chemical strategies to disperse $BaTiO_3$ NCs in polymer matrices for use in electronic devices. An outlook on how to further optimize the morphology of $BaTiO_3$ NCs and improve the dielectric performance of $BaTiO_3$ NCs and $BaTiO_3$/polymer nanocomposites is also presented.

Zhiqun Lin

Zhiqun Lin is a Professor in the School of Materials Science and Engineering at the Georgia Institute of Technology. He received his PhD in Polymer Science and Engineering from the University of Massachusetts, Amherst in 2002. His research interests include polymer-based nanocomposites, block copolymers, polymer blends, conjugated polymers, quantum dots (rods, tetrapods and wires), functional nanocrystals (metallic, magnetic, semiconducting, ferroelectric, multiferroic, upconversion and thermoelectric) of different architectures (plain, core/shell, hollow and Janus), solar cells, LEDs, batteries, photocatalysis, electrocatalysis, thermoelectrics, hierarchically structured and assembled materials, and surface and interfacial properties.

2. The structure–property relationship of nanoscale $BaTiO_3$

A reduction of system size into the nanoscale regime typically enhances the effect of microstructure, composition, stress,

defect concentration and surface composition on the type and intensity of ferroelectric dipoles. This is due primarily to the fact that these dipoles have a length scale of only a few angstroms (*i.e.*, the separation distance between the positive and negative charges of an elementary dipole), leading to unique dielectric and ferroelectric properties in $BaTiO_3$ NCs.[28,75,76] In this context, understanding and ultimately manipulating the dielectric properties through structure or phase design at the nanoscale is of prime importance for the practical application of this interesting material in various types of next generation micro and nano devices that rely on dielectric materials. Various strategies for obtaining desirable dielectric properties have been investigated. Among them, changing the size, shape and surface modification of $BaTiO_3$ NCs stand out as the most effective and widely studied strategies. Strategies of these types are the focus of this section.

2.1. $BaTiO_3$ nanocrystals of different shapes

$BaTiO_3$ nanostructures have attracted much attention because of their dielectric and ferroelectric properties can be modified by controlling their size and shape.[77] Among them, isotropic zero-dimensional (0D) $BaTiO_3$ nanoparticles of different sizes stands out as the most common form for practical applications because of the simplicity in their synthesis. In the case of one-dimensional $BaTiO_3$ (1D) nanostructures, there exist some difficulties in achieving simultaneous control for both their nanostructures and compositions because of the complexity in achieving stoichiometric ternary compound.[78–80] However, 1D $BaTiO_3$ nanostructures exhibit unique dielectric and ferroelectric properties attributed by their confinement in the radical direction, which win them wide research interest.[81–85] In addition, 1D $BaTiO_3$ nanostructures, which retain wire-like connectivity promising for efficient transport of electrons and photons, are promising building blocks for realizing miniaturizing devices.[54,86,87]

2.2. Size and shape effects

Size effects of the dielectric properties indicate a strong correlation between particle size and dielectric properties. As particle size decreases in the micrometer range, dielectric constant first increases significantly, reaching to a maximum value ($\sim$6000) at some particle size, and finally decreases when further decreasing particle size to below the micrometer range, as shown in Fig. 2a.[88,89] The particle size, where dielectric constant reaches maximum, depends heavily on the synthesis methods and process histories. For example, maximum dielectric constant (ε') of 6079 was achieved for $BaTiO_3$ ceramics prepared by two-step sintering method with the particle size of approximately 1 μm.[90] Another change accompanying the grain/particle size decrease is a reduction in the Curie temperature (T_C), which is the transition temperature between tetragonal and cubic phases (Fig. 2b). As a result, the room-temperature tetragonal distortion and hence ferroelectricity is gradually reduced with decreasing particle size. The critical size below which the room-temperature ferroelectricity of $BaTiO_3$ nanoparticles disappears varies greatly with the synthesis methods and is normally in the range of 10–100 nm.[46] Other factors, such as microstructure, composition, stress, defect concentration and interfacial effects, can also affect the critical size of ferroelectricity in $BaTiO_3$ nanocrystals.[44–47,91] However, many of these factors are likely interrelated with each other, which make it difficult to isolate their individual effects or separate with the intrinsic size effect. As a result, various models have been developed to explain the size effect,[92,93] though no agreement on accepted models exists. The only widely accepted point is that the size effect not only originates from the intrinsic atomic-scale polarization, but is also determined by the extrinsic nature of the material which is strongly related to processing history and the crystallinity of the NCs.[46] As most of these models are reviewed extensively in other literature,[94–96] here we focus primarily on the most recent and popular model, the "core–shell" model, with the goal of providing a clear illustration on the complex ferroelectric phase transition and dielectric properties which will be covered in the Materials synthesis (Section 3) and Single-crystal characterization (Section 4) parts. This model, evidenced by various structure characterization techniques, was initially proposed by Tsurumi *et al.*,[75,76] and is found to match well to the experimentally observed dielectric properties.

This model divides the $BaTiO_3$ particle into three regions: an inner core in tetragonal phase, an intermediate gradient lattice strain layer (GLSL), and a surface layer in cubic phase. In stark contrast to the conventional two layer model that contains only

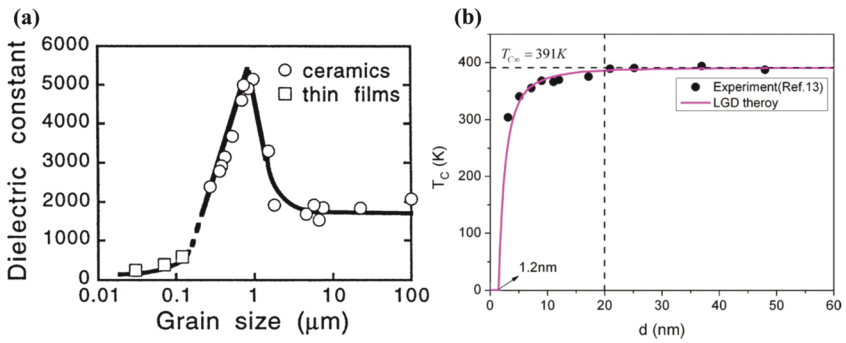

Fig. 2 (a) Dielectric constant of $BaTiO_3$ ceramics and thin films for samples with different grain size. Reproduced with permission.[88] Copyright 1998, IOP Publishing Ltd; (b) size effect of the Curie temperature. Reproduced with permission.[89] Copyright 2008, American Institute of Physics.

an inner core (tetragonal phase) and surface layer (cubic phase),[75,76] the extra GLSL layer, whose lattice parameters and atomic positions can change continuously, was introduced to account for the lattice mismatch between the inner tetragonal phase and the surface cubic phase.[75,76] In this model, the surface cubic layer remains a constant thickness of 10–15 nm, independent of particle size, while the other regions change their thickness with particle size.[75,76] When the $BaTiO_3$ particle size drops to a critical size where the tetragonal core doesn't exist, the ferroelectricity of $BaTiO_3$ disappears as well. This model can also be used to explain the size effect of dielectric permittivity. It is widely believed that the permittivity of ferroelectric $BaTiO_3$ (tetragonal core) is higher than that of paraelectric $BaTiO_3$ (surface cubic layer).[76] The transition GLSL layer exhibits the similar permittivity with the tetragonal phase.[75,76] As a consequence of the size-dependent volume fraction of ferroelectric phase and paraelectric phase, the dielectric constant displays strong size-dependence as well (see example in Fig. 2a). Many reports have supported this model and it agrees well with experimental measurements.[73,97,98]

Theoretically, the size-dependent ferroelectricity and the disappearance of ferroelectricity at lower dimensions can be well-explained by the depolarization effect. Depolarization fields in ferroelectric materials arise from incomplete compensation for the ferroelectric polarization charges.[99,100] As shown in Fig. 3a, for a ferroelectric material with polarization p, a total surface charge density (σ) of $\sigma = p{\cdot}n$ is induced (where p is the polarization vector and n is the unit normal to the surface) due to the discontinuities of polarization near the vicinity of the surface.[101] As a result, a depolarization field oriented in the opposite direction of the spontaneous polarization is produced inside the ferroelectric material, which reduce the ferroelectricity of the material (Fig. 3b).[102] However, the surface charges are unstable if they are not compensated by external screening electrodes, as a result, a net depolarization field (E_d) develops and can be described by the following equation:[99] $E_{dep} = -\frac{P}{\varepsilon_F}\left(\frac{2\varepsilon_F/l}{2\varepsilon_F/l + \varepsilon_e/l_s}\right)$, where ε_F and ε_e represent the dielectric constant of the ferroelectric material and the screening electrode, respectively; l_s and l denote the screening length and the thickness of the ferroelectric film, respectively. In the case where the ferroelectric material is sandwiched between two perfect metallic electrodes, *i.e.* $\varepsilon_e \rightarrow \infty$, the surface charges can be completely compensated, so no net depolarization field will be introduced ($E_d \rightarrow 0$). On the other hand, when partially compensated, the depolarization field is not fully cancelled, as described by the above equation. It is clear from the equation that, only in the limit when $l \rightarrow \infty$ or $l_s \rightarrow 0$, the depolarization field vanishes. However, for extremely small dimension when $l \rightarrow 0$ and at relatively large screening lengths, a significant depolarization field will build up, resulting in the disappearance of ferroelectricity at small dimensions.

In addition to size, the shape of $BaTiO_3$ NCs can also influence their dielectric and ferroelectric properties (*i.e.* shape effect).[103] For example, 10 nm diameter $BaTiO_3$ nanoparticles tend to have suppressed ferroelectricity at room temperature due to the decreased Curie temperature, while 1D $BaTiO_3$ nanowires with 10 nm diameter retain their ferroelectric properties.[77] In contrast to 0D nanostructures, 1D nanostructures tend to be influenced by extrinsic strains which are generated during the fabrication process. Depending on the types of strain produced in $BaTiO_3$ nanostructures, they can either enhance the polarization or suppress it.[103]

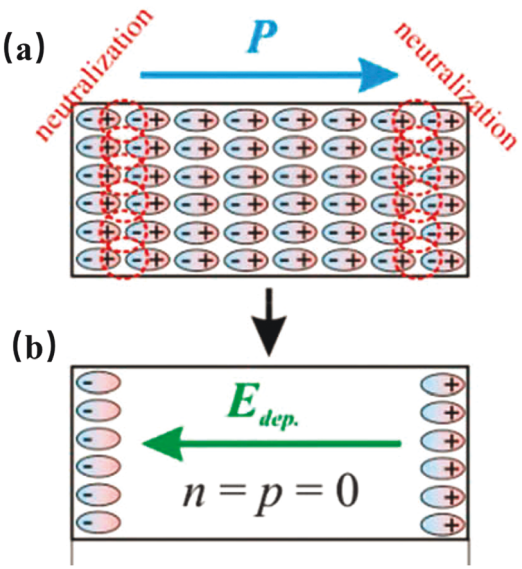

Fig. 3 (a) Schematic representation of an uncompensated ferroelectric material with fixed surface charges. (b) Schematic representation of the depolarization field inside the ferroelectric material induced by the surface charge with the depolarization field pointing against the direction of self-polarization *P*. Reproduced with permission.[102] Copyright 2015, the Owner Societies.

2.3. Surface effects

Depending on the preparation method, the surface of as-prepared $BaTiO_3$ NCs can be covered with different molecular adsorbates, such as hydroxyl groups (OH) if prepared by sol–gel or hydrothermal techniques, or carbonaceous species if synthesized from various precursor routes.[104] More importantly, most of these atomic or molecular adsorbates can better stabilize the ferroelectricity of nanoscale $BaTiO_3$.[105] In this regard, many efforts have been made to tailor the surface of $BaTiO_3$ NCs for manipulating their dielectric and ferroelectric properties. To date, surface modification has been widely achieved through chemical bonding with surface ligands[104,106] and coatings.[107] In one study, the *n*-hexylphosphonic acid (HPA)-functionalized $BaTiO_3$ NCs possess improved dielectric constant but displayed decreased sensitivity to temperature and frequency in comparison to unmodified $BaTiO_3$ NCs.[104] Another study involving coating of a manganese (Mn) layer on 40 nm $BaTiO_3$ nanoparticles demonstrates that surface coating can preserve the ferroelectricity of extremely small particles, enabling them to adopt a pure tetragonal ferroelectric phase.[107] Transmission electron microscopy (TEM) observations show that the Mn coating produces an amorphous phase and hence cause some strain near the grain boundary of the samples, which is

believed to be the main cause of the increased tetragonality and the preservation of ferroelectricity below the critical size of unmodified particles.[75,76]

3. Synthesis of $BaTiO_3$ NC *via* chemical methods

Currently, most $BaTiO_3$ materials used in industrial applications are still prepared by conventional solid-state reactions which require high temperatures (above 1000 °C), and the resulting $BaTiO_3$ materials are normally polycrystalline with uncontrolled morphologies that are not suitable for advanced applications.[108–113] Alternatively, a controlled synthetic scheme could produce highly crystalline nanoparticles with a monodisperse size distribution for targeted performance properties and applications. It would also enable systematic variation of their size and shape, making it possible to study the size-dependent and shape-dependent properties. Finally, controlling the crystalline phase so that $BaTiO_3$ can readily switch between the paraelectric and ferroelectric phases is also important for designing advanced materials for devices.[114] Satisfying all the requirements noted above, chemical approaches are an accepted alternative to the traditional solid-state approach. Owing to the more uniform mixing between barium and titanium cations, chemical methods are able to yield stoichiometric NCs with well-controlled size, morphology and crystallinity. This preserves the dielectric properties while maintaining a low reaction temperature and reduced energy consumption.[115,116] The elimination of high temperature processes cuts the cost of fabrication and makes it much easier to scale up.[117,118] A large number of synthetic methods fall into the category of chemical approaches, including organo-metallic,[39] solvothermal/hydrothermal,[51,53] and template methods.[55,56] Thus, chemical methods offer the most flexible approach to obtain high quality $BaTiO_3$ NCs with well controlled morphology (*e.g.*, nanodots, nanorods, nanocubes, and nanowires) and crystal structure (*e.g.*, cubic or tetragonal). All of these methods are covered in subsequent sections. Within each category, representative examples are provided to illustrate the general synthetic strategy and NC growth mechanism.

3.1. Formation mechanism of $BaTiO_3$

The controlled growth of $BaTiO_3$ with desired morphology requires a good understanding of the nucleation and crystallization mechanism. A lot of factors, including the rate of nuclei formation, the rate of crystalline growth, and agglomeration of crystals can contribute to the overall particle growth process and the size distribution of $BaTiO_3$ particles.[119] Both classical and nonclassical crystal nucleation and growth processes have been used to describe the nucleation of many chemical systems.[120] In a classical crystal nucleation and growth process, ions and molecules firstly aggregate together to reach a supersaturated state which triggers the nucleation process. Once the nucleus reaches some critical size, crystal growth can occur.[121] The nonclassical theory differs from the classical theory in that the crystals may grow from mesoscale solid species instead of nuclei.

In general, several different theories have been proposed to describe the nucleation and growth process, including the Lamer burst nucleation mechanism,[122,123] Ostwald ripening,[124] Finke–Watzky two step mechanism, coalescence and oriented attachment and intraparticle growth. The Lamer mechanism proposes that a "burst-nucleation" process takes place instantly once there is a large amount of free monomers in the solution, which leads to the quick consumption of free monomers and stops the nucleation process. The remaining free monomers in solution then diffuse to the nucleus leading to crystal growth.[120] The Ostwald ripening mechanism describes the growth of particles by dissolving smaller particles since they have higher surface energy and hence higher solution solubility.[120,124] The dissolved particles diffuse and redeposit on the surface of larger particles, making them into much bigger ones.

The dominating nucleation and growth mechanism of $BaTiO_3$ varies a lot for different growth methods. Even for the same growth method, no agreement has been reached regarding the growth mechanism.[121] In following Sections 3.2–3.6, various soft chemical growth methods of $BaTiO_3$ NCs are discussed, with growth mechanisms for some growth methods also covered.

3.2. Organometallic methods

Organometallic methods (also known as the hot injection methods) use organometallic precursors possessing a fixed stoichiometric ratio of the metal cations dissolved in some organic solvent. It provides an ideal environment for controlling NCs growth because the nucleation process and the subsequent growth processes are separated. In a typical organometallic process, as depicted in Fig. 4, the organometallic precursors are quickly injected into the reaction system at a high temperature, leading to rapid nucleation. The temperature drops after injection of precursors and the growth process starts to occur. Surfactants or stabilizing agents are usually present in this crystal growth process for controlling the morphology of the resulting NCs.[38] So far, this method has achieved great success in synthesizing a rich variety of NCs, including semiconductor[37–39] and metal oxide[125–127] types, and is widely regarded as the best approach for controlling both the size and morphology of the resulting NCs.[128]

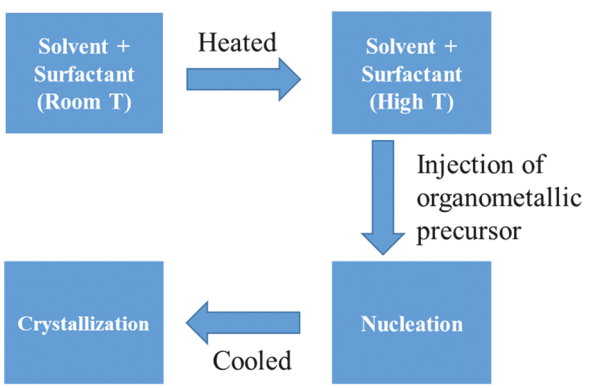

Fig. 4 A simple graphical representation of typical organometallic method, which separates the nucleation process and growth process.

In a typical procedure for synthesizing $BaTiO_3$ NCs, a moisture-sensitive bimetallic alkoxide, for example, barium titanium ethyl hexano-isopropoxide ($BaTi(OR)_6$), is injected into mixed solvents of diphenyl ether and oleic acid at 140 °C under argon or nitrogen atmosphere. Diphenyl ether is the solvent while oleic acid serves as the stabilizing agent for enabling the transfer of particles to nonpolar solvents and preventing their aggregation. The bimetallic alkoxide precursors with equal amounts of Ba and Ti ions provide the correct stoichiometry (*i.e.*, Ba to Ti ratio) in the resulting product.[49] Hydrogen peroxide is further injected into the system once it is cooled to 100 °C to trigger the hydrolysis of the precursor and the formation of uniform $BaTiO_3$ nanoparticles with a diameter of 8 nm. By increasing the precursor/oleic acid ratio or adding more peroxide solution to the system, larger nanoparticles (9–12 nm) can be created. Lowering the ratio reduces the particle diameter to 4–6 nm. In addition, the resulting $BaTiO_3$ nanoparticles self-assembled into regular superlattice structures owing to the strong van der Waals or dipolar interactions between particles.

Since the first successful reports of nearly monodisperse NCs produced by this hydrolysis method, it has been limited to the preparation of isotropic 0D sphere-like morphologies. However, anisotropic 1D nanostructures (*e.g.* nanowires, nanorods, nanotubes) are more promising building-blocks for realizing advanced devices because of their wire-like connectivity which enables efficient transfer of heat, stress, and charge.[54] The first report of preparing $BaTiO_3$ nanorods by this method is quite similar to that of forming isotropic $BaTiO_3$ nanoparticles, with similar mixed solution of diphenyl ether and oleic acid containing the bimetallic alkoxide precursor ($BaTi[OCH(CH_3)_2]_6$) as precursor, and the hydrolysis were trigged by the injection of hydrogen peroxide. Anisotropic growth of resulting nuclei into nanorods is achieved through slow precursor decomposition and crystallization at a high temperature (280 °C) within a micelle structure formed by the precursor and oleic acid. Furthermore, the resulting nanorods are of cubic phase, according to the XRD pattern shown in the inset of Fig. 5, and each nanorod is a single crystal.

Although the organo-metallic approach is successful at producing NCs of the highest quality, its broad utilization in industry is limited largely owing to scale-up issues, the exotic reagents, and the use of expensive and highly toxic organometallic precursors. In addition, the consumption of large amounts of organic solvent further complicates its use due to environmental concerns.[129] Therefore, more environmentally-friendly and more cost-effective methods are desirable for industrial applications.

3.3. Solvothermal/hydrothermal growth

Solvothermal/hydrothermal methods are also powerful tools for the controlled syntheses of various nanomaterials.[130–136] They have received the most interest because they can produce high quality crystalline powders at low temperatures in one-step reactions.[119,121,137] The solvothermal/hydrothermal reactions occur by sealing organic or aqueous solutions in an autoclave and increasing the solvent temperature to a desired reaction temperature higher than the normal boiling point of the solvent due to the pressure buildup during heating within the autoclave. As a result, crystalline powders with nanoscopic morphologies can be formed, accompanied by some unexpected reactions.[138] Normally, these nanoscopic morphologies formed during the solvothermal/hydrothermal reactions can be easily controlled by varying the reaction parameters, solvents, precursors,[139–142] capping reagents/surfactants,[143–145] reaction temperature,[146,147] pH,[148–150] and the Ba/Ti ratio. Furthermore, these NCs are difficult to form by many other conventional methods.

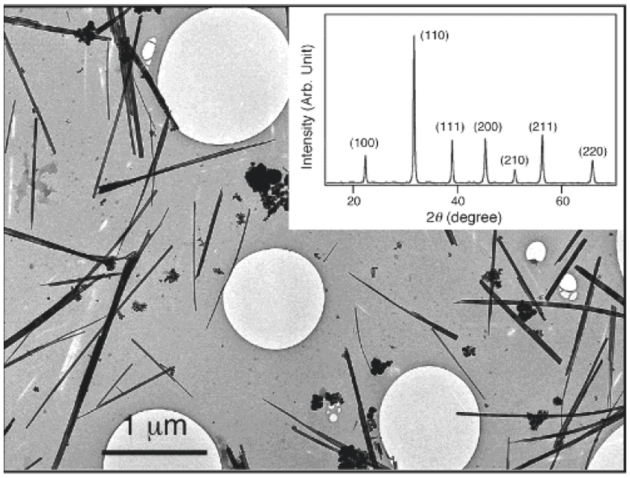

Fig. 5 TEM image of $BaTiO_3$ nanorods synthesized by a thermal decomposition method. Inset: Powder XRD pattern of the randomly-oriented $BaTiO_3$ nanorods. Reproduced with permission.[54] Copyright 2002, American Chemical Society.

3.3.1. Hydrothermal methods. The hydrothermal synthesis of $BaTiO_3$ is a low cost, one-step reaction process involving an aqueous medium under strong alkaline conditions. In the early period of producing $BaTiO_3$ for pigment applications, $BaTiO_3$ was widely prepared by reacting $Ba(OH)_2$ with TiO_2 at the boiling point of water under hydrothermal conditions.[137] Later, other groups extended this method to producing $BaTiO_3$ NCs or thin films for electronic applications.[151,152]

Various titanium precursors including titanium oxide (TiO_2), titanium tetrachloride ($TiCl_4$), titanium alkoxide or titanium oxide gel, and barium precursors have been used to produce $BaTiO_3$ NCs with desired sizes and shapes. In a study of hydrothermally producing $BaTiO_3$ NCs by two different sets of starting materials,[153] the $BaTiO_3$ NCs (sample A) produced using titanium hydroxide ($Ti(OH)_4$) and barium hydroxide ($Ba(OH)_2{\cdot}8H_2O$) as precursors exhibited uniform size ($D \sim 65$ nm) and shape with narrow size distribution (Fig. 6a), while sample B prepared using titanium dioxide (TiO_2) and barium hydroxide are less uniform (Fig. 6b). The comparison also indicated that the internal strain in the as-prepared $BaTiO_3$ NCs was higher in particles of sample B than sample A. However, in neither case were the stresses sufficient enough to induce the cubic-to-tetragonal phase transition, leaving both sample A and B to exhibit a metastable

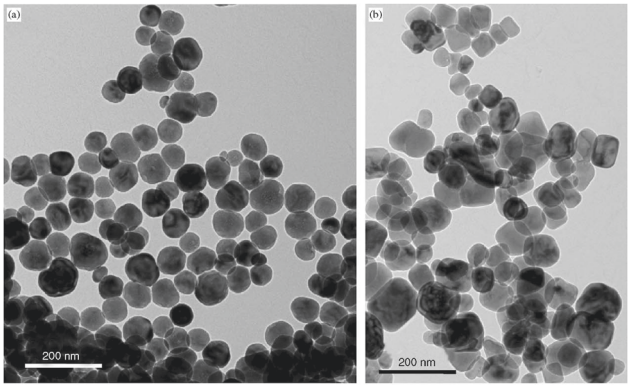

Fig. 6 TEM images of $BaTiO_3$ nanocrystals with different morphologies synthesized under the same hydrothermal conditions but with different starting materials. (a) Sample A produced with titanium hydroxide ($Ti(OH)_4$) and barium hydroxide ($Ba(OH)_2$)·$8H_2O$ as starting materials. (b) Sample B produced from titanium dioxide (TiO_2) and barium hydroxide ($Ba(OH)_2$)·$8H_2O$. Reproduced with permission.[153] Copyright 2005, Elsevier.

cubic phase.[154,155] In addition, the as-prepared $BaTiO_3$ powders prepared from this hydrothermal method exhibited a high concentration of lattice defects of OH^- and cation vacancies. These induce some strain within the metastable cubic phase and caused some tetragonality.[154,155] By varying the concentrations of the lattice OH^- through changing the reaction parameters, properties such as stoichiometry (Ba/Ti ratio), defects, size and shape can be varied.[154]

The hydrothermal growth of anisotropic 1D $BaTiO_3$ nanostructures can be achieved by varying the reaction parameters or adding surfactants. For example, a seed-induced hydrothermal reaction between equimolar $Ba(OH)_2$ and TiO_2 particles was utilized to synthesize $BaTiO_3$ nanowires (Fig. 7a and b).[48] As shown in the graphical representation of growing $BaTiO_3$ nanowires from TiO_2 nanoparticles (Fig. 7c), TiO_2 particles acted as seeds for the redeposition of dissolved $Ba(OH)_2$ particles and the subsequent growth of anisotropic $BaTiO_3$. By controlling the pH and temperature of the system, higher aspect ratio nanowires can be achieved.

The hydrothermal method is also capable of producing other intriguing nanostructures, owning to its unique reaction conditions. For example, novel bowl-like $BaTiO_3$ nanoparticles were obtained by hydrothermal reaction between $Ba(OH)_2$·$8H_2O$ and TiO_2 at 180 °C for 72 hours. The Ba/Ti molar ratio in this reaction was altered to give a greater amount of Ba precursor.[51] As shown in Fig. 8a–c, both scanning electron microscope (SEM) and TEM confirm the bowl-like morphology of the resulting $BaTiO_3$ nanoparticles (D = 100–200 nm) which had a concave center.

The growth mechanism of hydrothermally produced nanostructured $BaTiO_3$ varies greatly by using different starting materials. Recently, a novel ion-exchange reaction mechanism was utilized for producing $BaTiO_3$ nanowires.[52] In this study, alkali-metal titanate precursors, such as $Na_2Ti_3O_7$ nanowires and $K_2Ti_4O_9$ nanowhiskers experienced ion-exchange and conversion with $Ba(OH)_2$, producing $BaTiO_3$ nanowires. Since the resulting $BaTiO_3$ nanowires preserve the relative size and shape

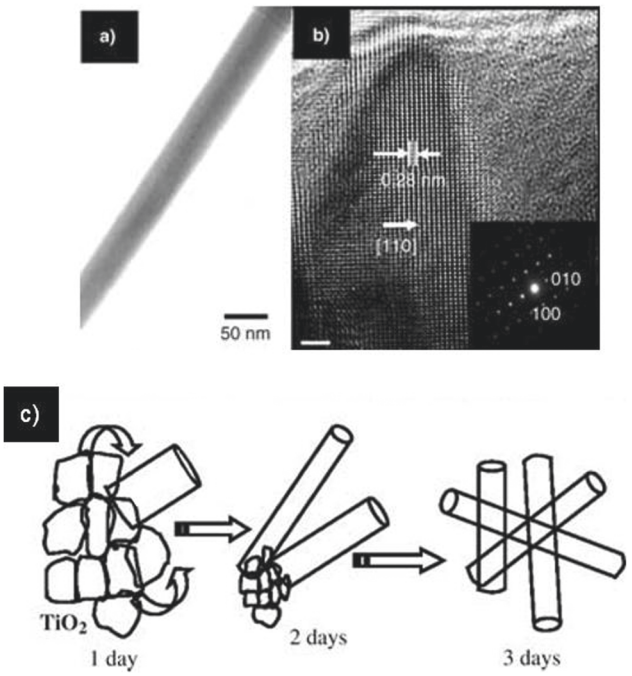

Fig. 7 (a) Typical TEM image of a $BaTiO_3$ nanowire; (b) HRTEM image of the tip of a $BaTiO_3$ nanowire, the clear lattice fringes indicate that the entire $BaTiO_3$ nanowire is a single crystal. Scale bar equals 2 nm. (c) A graphical representation of the growth mechanism of $BaTiO_3$ nanowires produced from TiO_2 nanoparticles *via* a hydrothermal method. Reproduced with permission.[48] Copyright 2005, Wiley.

of the Ti precursor (*i.e.* the $K_2Ti_4O_9$ nanowhiskers, $Na_2Ti_3O_7$ nanowires), $BaTiO_3$ nanowires produced from $K_2Ti_4O_9$ nanowhiskers (Fig. 9d) are much longer than those obtained from $Na_2Ti_3O_7$ nanowires (Fig. 9c).

In addition, different $BaTiO_3$ formation mechanisms due to the different titanium precursors also influence the number of defects in the resulting $BaTiO_3$ NCs.[156] It was found that $BaTiO_3$ nanopowders synthesized using TiO_2 nanoparticles have higher tetragonality (c/a = 1.0081) than those synthesized using titanium isopropoxide (c/a = 1.0070). Despite these differences, they exhibited similar sizes and shapes. This is because when using TiO_2 as the titanium precursor during the hydrothermal synthesis, the resulting $BaTiO_3$ specimens exhibited less OH^- or Ba vacancy defects, leading to higher tetragonality.[156]

The size and shape of hydrothermally-produced $BaTiO_3$ NCs can be controlled by adding surfactants and controlling the preferred growth facets. In a study, oleic acid was used as a surfactant for producing cube-like $BaTiO_3$ NCs (Fig. 10a–f).[53] During the hydrothermal reaction, oleic acid was adsorbed to the formed $BaTiO_3$ nanocrystals creating a hydrophobic surface which further leads to the growth of low index facets such as (100) planes in $BaTiO_3$ NCs. This is because these facets are nonpolar and thus more stable than higher index planes such as (110) and (111).[53,157]

In addition to 0D and 1D $BaTiO_3$ NCs, 2D conformal $BaTiO_3$ films can also be produced by scalable hydrothermal method. When hydrothermally growing conformal $BaTiO_3$ thin films,

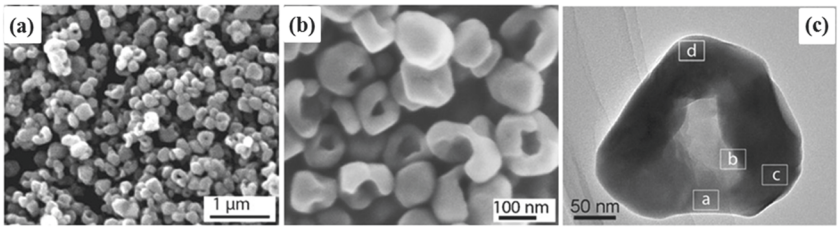

Fig. 8 (a and b) SEM images of bowl-like $BaTiO_3$ nanoparticles with concave centers; (c) HRTEM image of a bowl-like $BaTiO_3$ nanoparticle which shows an empty center. Reproduced with permission.[51] Copyright 2010, Springer.

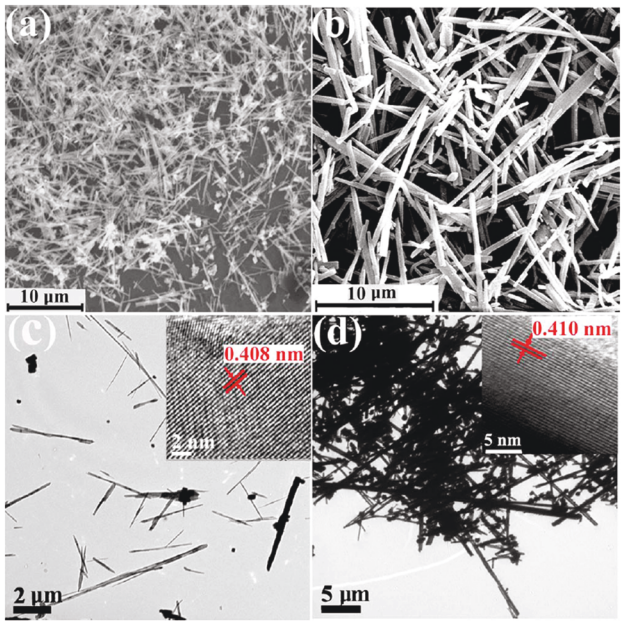

Fig. 9 SEM images of (a) $Na_2Ti_3O_7$ nanowires and (b) $K_2Ti_4O_9$ nanowhiskers sacrificial templates for producing $BaTiO_3$ nanowires. (c) TEM image of hydrothermally prepared $BaTiO_3$ nanowires prepared using $Na_2Ti_3O_7$ nanowire templates (inset: HRTEM image shows the lattice fringes of the templated $BaTiO_3$ nanowires); (d) TEM images of $BaTiO_3$ nanowires prepared using $K_2Ti_4O_9$ nanowhiskers as templates (inset: HRTEM image showing the lattice fringes of $BaTiO_3$). Reproduced with permission.[52] Copyright 2009, American Institute of Physics.

rutile TiO_2 is the most commonly used Ti precursor as rutile TiO_2 can be uniformly grown over all substrate surfaces regardless of their dimension or geometry.[158] Moreover, it also functions as template for controlling the morphology of the resulting $BaTiO_3$ films. Fig. 11a–e depict the strategy involving two hydrothermal reactions to grow conformal textured $BaTiO_3$ films and the corresponding SEM images. As illustrated, an array of TiO_2 nanowires (NWs) ranging in length from 2 to 8 μm were first grown on a FTO-coated silicon wafers by a hydrothermal process at 180 °C. Afterwards, the conformal TiO_2 NW arrays were converted into conformal $BaTiO_3$ thin films during the second hydrothermal reaction at 240 °C, where TiO_2 was first dissolved to form $Ti(OH)_4$ that reacted with Ba^{2+} ions and then deposited a layer of $BaTiO_3$ particles on the surface of TiO_2 NWs. As the process continued, $BaTiO_3$ crystals grew, converting the conformal TiO_2 arrays into continuous and crack-free $BaTiO_3$ films. The thickness of the resulting $BaTiO_3$ films is directly related to the thickness of the TiO_2 NWs.[158] Compared with most of the current methods for the conformal deposition of $BaTiO_3$ films, such as metal–organic chemical vapor deposition (MOCVD) and atomic layer deposition (ALD), hydrothermal methods possess the advantages of easy controllability, easy scalability, and cost-effectiveness. Moreover, hydrothermal approach with optimized reaction conditions described above is capable of improving the performance and storage capacity of the resulting electronic devices.

3.3.2. Solvothermal methods. Similar to the hydrothermal method, the solvothermal method refers to reactions in a sealed autoclave using nonaqueous solvents. In a typical procedure of solvothermally producing $BaTiO_3$ nanoparticles in the presence of anhydrous benzyl alcohol as the solvent, the dissolved metallic barium reacts with titanium isopropoxide at temperatures between 200 and 220 °C *via* a mechanism involving C–C (carbon–carbon) bond formation.[159,160] The resulting $BaTiO_3$ nanoparticles are single crystals with diameters ranging from 4–5 nm (Fig. 12a–c). Because of the elimination of halide precursors and other inorganics such as alkali metal ions, this method is capable of producing extremely high-purity samples.

Another facile solvothermal method of using barium hydroxide monohydrate ($Ba(OH)_2{\cdot}H_2O$) and titanium butoxide ($Ti[O(CH_2)_3{\cdot}CH_3]_4$) as starting materials has recently been developed.[161] The particle size of solvothermally produced $BaTiO_3$ nanoparticles can be controlled by the mixed solvents of diethanolamine (DEA) and triethanolamine (TEA) since the organic amines increase the number of nucleation sites, leading to a reduction in particle size. In addition, the $BaTiO_3$ nanoparticles synthesized by this solvothermal method showed some tetragonality which could be potentially used for miniaturized devices that require ferroelectric response or large dielectric constants.

3.4. Template-assisted methods

Template-assisted methods involve the directed crystallization of NCs within a specific area of a template. Such methods are simple and efficient for fabricating nanostructures with well-controlled morphologies.[162–165] Templating methods are typically low cost, easily reproducible, large yields, environmentally benign, and flexible. To date, a large number of $BaTiO_3$ nanostructures including nanodots, nanotubes and nanotube arrays have been reported by this approach with either a "hard template" (*e.g.*, anodic aluminum oxide (AAO) and TiO_2) or "soft template" (*e.g.*, polymers, peptides and biomaterials).

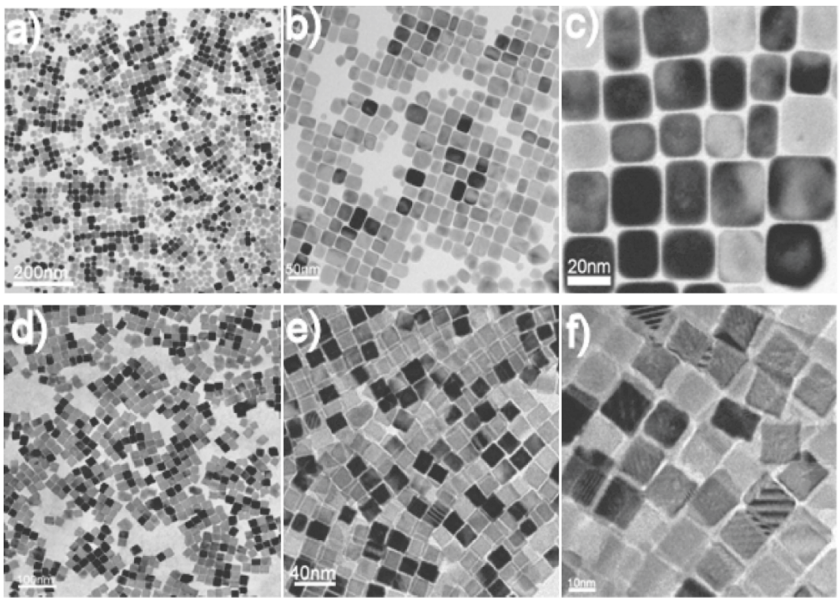

Fig. 10 TEM images of (a–c) cubelike and (d) cubic $BaTiO_3$ nanoparticles with each forming monolayers due to the assembly of $BaTiO_3$ nanoparticles; (e and f) $BaTiO_3$ nanoparticles assembled into bilayer structures at different magnifications. Reproduced with permission.[53] Copyright 2010, American Chemical Society.

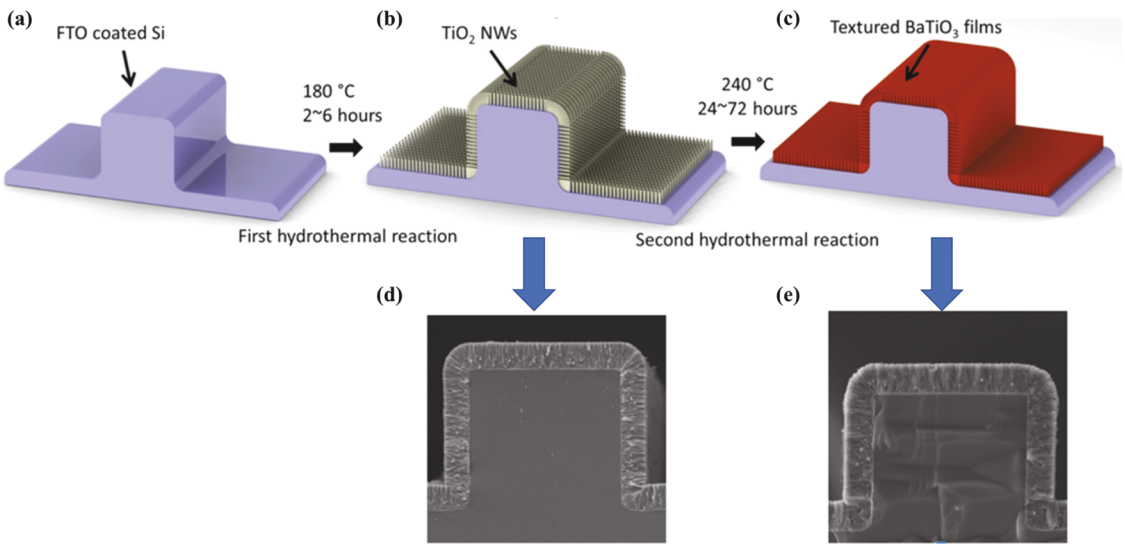

Fig. 11 (a–c) Schematic illustration of the strategy to grow conformal $BaTiO_3$ films. SEM images of (d) conformal TiO_2 NW arrays on FTO coated silicon wafers and (e) conformal $BaTiO_3$ films.[158] Copyright 2016, American Chemical Society.

3.4.1. Hard templating. Nanofabrication of ordered structures using a negative template which has 1D holes or channels, such as porous anodic aluminum oxide (AAO) membranes or track-etched polycarbonate, has received much attention due to its ability to produce a large number of ordered structures without the need for expensive or extreme conditions.[166–169] Typically, the porous templates are immersed in the precursor solutions, followed by the evaporation of solvents under high temperature, which triggers the growth of crystals along the surface of the porous template. The nanostructures are finally produced by selectively removing the template either by dissolution or calcination at elevated temperature.[170] The dimensions and array pattern of produced NCs can be easily tuned by varying the reaction conditions, such as precursor concentration, pH, immersion time, temperature, pore structure and surface properties.[171,172] In a study of growing 1D $BaTiO_3$ nanostructures with AAO as a structure-directing template from aqueous solutions, stoichiometric $BaTiO_3$ nanotubes over large areas were successfully produced under near-ambient conditions (Fig. 13).[172] In this study, the precursor solution with controlled concentration and pH was made by dissolving $Ba(NO_3)_2$ and $(NH_4)_2TiF_6$ in an aqueous acidic solution.

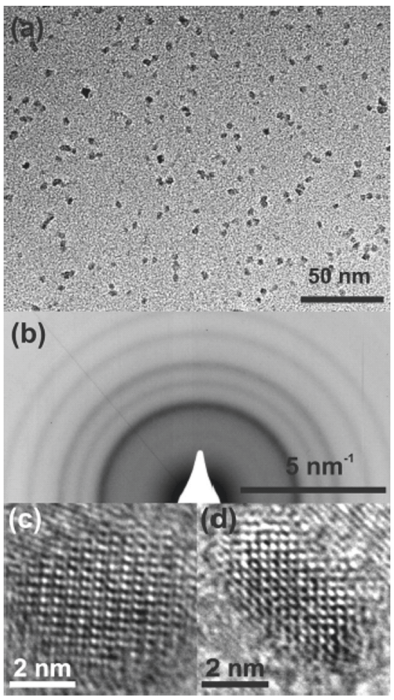

Fig. 12 (a) TEM image of synthesized $BaTiO_3$ nanoparticles exhibiting good uniformity and no aggregation; (b) selected area electron diffraction (SAED) of synthesized $BaTiO_3$ nanoparticles; (c and d) HRTEM images of individual $BaTiO_3$ nanoparticles confirming that each isolated nanoparticle is a single crystal. Reproduced with permission.[159] Copyright 2004, American Chemical Society.

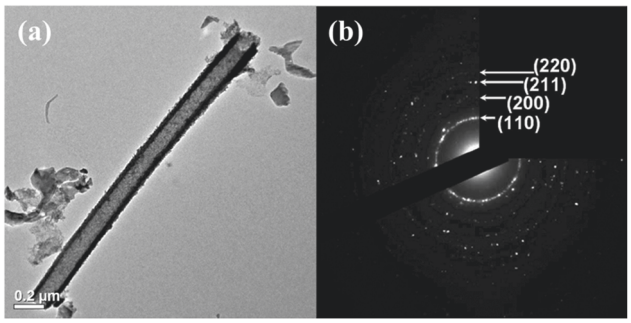

Fig. 13 (a) Bright-field TEM image, and (b) selected area electron diffraction (SAED) of an isolated $BaTiO_3$ nanotube fabricated from an AAO template under near-ambient conditions. Reproduced with permission.[172] Copyright 2009, American Chemical Society.

Through the liquid-phase deposition and hydrolysis of cations, nanotubes with thinner tube walls were produced. The AAO template was modified by (octadecyl)trichlorosilane (OTS) to make it hydrophobic so as to decrease the overall deposition rate and suppress pore blocking. The obtained $BaTiO_3$ nanotubes were around 250 nm in diameter and 2.5 μm in length. Even longer and more stoichiometrically balanced $BaTiO_3$ nanotubes can be obtained by adjusting the dimensions of the AAO template. A similar method was also reported for growing $BaTiO_3$ nanoshell tubes with controllable wall thickness.[171] An extra wetting process was introduced and driven by the reduced surface energy of the system under ambient conditions. This allowed the incoming polymeric precursor to form a thin layer on the wall and crystallize into $BaTiO_3$ nanoshell tubes with a shell thickness of 100 nm and controllable aspect ratio (over 50). After annealing at high temperature, the $BaTiO_3$ nanotubes displayed ferroelectric switching properties.

In addition to AAO templates, other templates have also been used to direct the growth of nanostructured $BaTiO_3$ NCs. For example, track-etched hydrophilic polycarbonates (PC) were proved to be effective templates for producing $BaTiO_3$ nanorods.[173] In this approach, a combination of sol–gel processing and electrophoretic deposition was utilized in which the Pt mesh anode was immersed in the precursor sol while the PC membrane was attached to the aluminum cathode and placed on top of the precursor sol. After applying a 5 V potential between the electrodes, the $BaTiO_3$ nanorods begin to grow, yielding denser oxide nanorods with improved quality compared to other methods without the electrophoretic deposition process.

In contrast to negative templates which have voids or holes for precursor filling, positive templates (shape of desired structure to be templated) such as 1D TiO_2 nanostructures and their arrays can be directly convert into 1D $BaTiO_3$ nanostructures because they serve as both precursors and physical templates.[93,174] For example, Li *et al.*[93] produced single crystalline $BaTiO_3$ nanotube arrays using a hydrothermal method with TiO_2 nanotube array as templates. During the reaction process, the TiO_2 nanotube arrays reacted with the dissolved Ba ions in the solution while producing $BaTiO_3$ nanotubes that preserve the original shape of the TiO_2 template. TEM results (Fig. 14a and b) of randomly selected top-view of $BaTiO_3$ nanotubes confirmed the identical crystallographic orientations of the produced $BaTiO_3$, indicating that all $BaTiO_3$ nanotubes have identical crystallographic orientation during their growth. XRD pattern (Fig. 14c) of $BaTiO_3$ nanotube arrays further indicated the high purity of $BaTiO_3$ nanotubes, suggesting that the TiO_2 nanotube templates had been completely converted into $BaTiO_3$ nanotubes.[174,175]

Besides 1D mesoporous structures (*i.e.*, AAO or TiO_2 tubes), 0D spherical nanoparticles can also be used as templates. A representative example reports the use of colloidal arrays of polystyrene (PS) spheres as templates for producing macroporous $BaTiO_3$ structures.[176] In brief, the $BaTiO_3$ precursors were allowed to penetrate through the voids in a 3D ordered PS template formed by assembling 726 nm PS spheres into planar ordered arrays. Through solidification and subsequent calcination, an array of macroporous $BaTiO_3$ was formed while retaining the long-range order of the PS colloidal array template, exhibiting an ordered hexagonal close-packed structure (Fig. 15). Another similar study of utilizing colloidal PMMA particles as templates produced hollow $BaTiO_3$ spheres.[56] In this example, multilayered colloidal titanate spheres were prepared by depositing the titanium precursors on the colloidal template, followed by dissolution of the PMMA template in tetrahydrofuran (THF) for producing hollow titanate spheres. Finally, the hollow titanate spheres served as the new template and were converted into hollow $BaTiO_3$ spheres by reaction with $Ba(OH)_2$ solution under hydrothermal conditions. The resulting hollow $BaTiO_3$ spheres

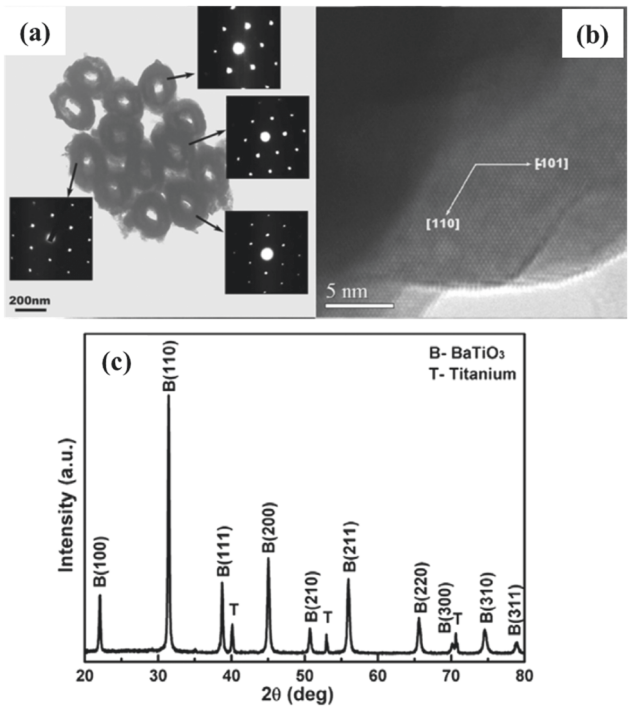

Fig. 14 (a) Top-view TEM images of $BaTiO_3$ nanotubes with SAED patterns in the insets; (b) HRTEM image of $BaTiO_3$ nanotube; (c) XRD pattern of $BaTiO_3$ nanotube arrays.[93] Copyright 2009, IOP science.

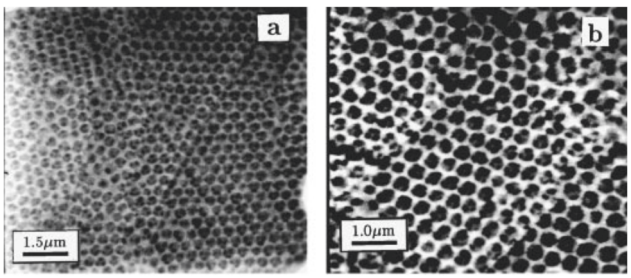

Fig. 15 (a and b) SEM images of macroporous $BaTiO_3$ layers produced using ordered arrays of PS spheres as templates. Reproduced with permission.[176] Copyright 2000, Royal Society of Chemistry.

displayed a well-defined size and shape conforming to the PMMA template (Fig. 16). In addition, by controlling the number of layers deposited onto the PMMA template, the wall thickness of the hollow $BaTiO_3$ spheres can also be varied. The results indicate that they have a well-defined diameter dictated by the diameter of the template and uniform wall thickness controlled by the number of layers deposited.

3.4.2. Soft templating. As discussed in Section 2, one of the main challenges is to produce high quality $BaTiO_3$ NCs of tetragonal crystalline structure (ferroelectric phase with high dielectric permittivity) at low temperature. Most of the $BaTiO_3$ NCs obtained so far, especially those below 10 nm, are in the cubic phase because it is the thermodynamically stable phase at room temperature due to size effects.[75,76] To convert the cubic phase into the ferroelectric tetragonal phase, extra steps such as post-annealing at high temperature are usually required.

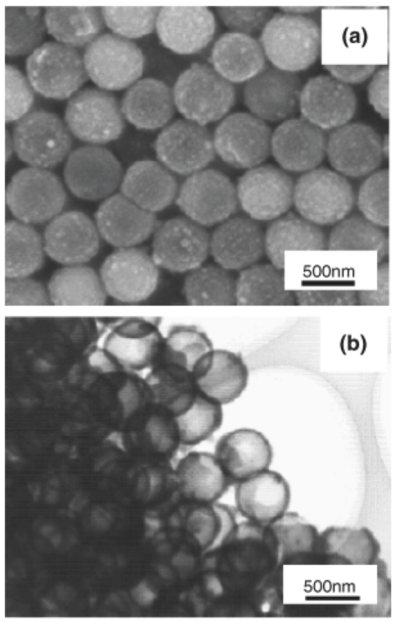

Fig. 16 (a) TEM micrographs of PMMA spheres coated with titanate nanoparticles; (b) SEM image of hollow $BaTiO_3$ spheres. Reproduced with permission.[56] Copyright 2006, Wiley.

These extra steps increase the complexity and cost of production and often lead to many other problems, such as nanoparticle aggregation and coarsening.[57,177] The first example of tetragonal $BaTiO_3$ nanoparticles produced at room temperature was made by Yang *et al.*[57] In this study, a peptide nanoring template self-assembled into a structure with some cavities in the center which can load the bimetallic precursor $BaTi(O_2CC_7H_{15})$-$[OCH(CH_3)_2]_5$ and allow the precursor to hydrolyze and crystallize into $BaTiO_3$ nanoparticles (Fig. 17a). By adjusting the pH value, the cavity size of the nanorings varies between 6 and 12 nm. This enables a flexible tailoring of the diameter of the resulting

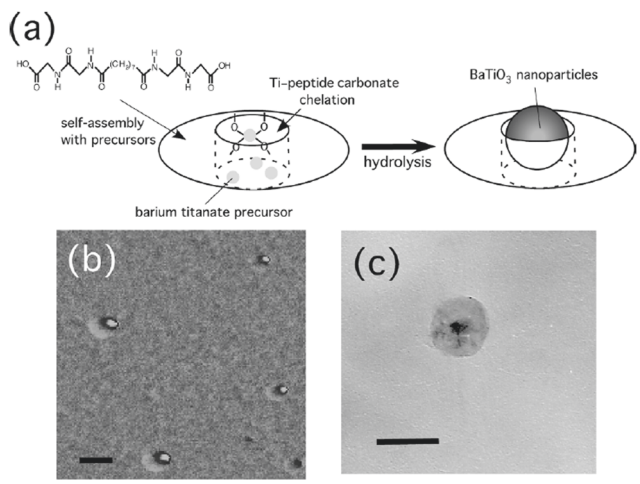

Fig. 17 (a) Illustration of the growth process for $BaTiO_3$ nanoparticles using self-assembled peptide templates; (b) AFM and (c) TEM images showing $BaTiO_3$ nanoparticles inside the peptide nanoring template (scale bars for (b) and (c) are 50 nm and 60 nm, respectively). Reproduced with permission.[57] Copyright 2006, Wiley.

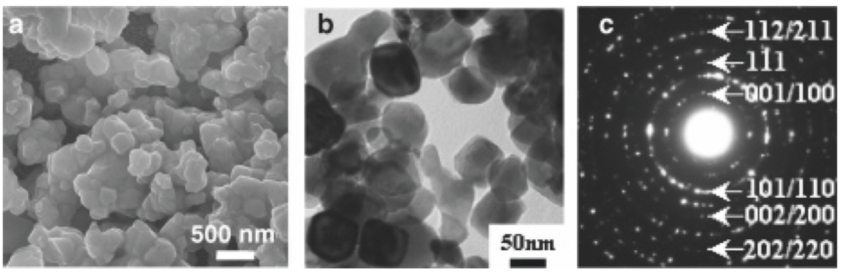

Fig. 18 (a) SEM and (b) TEM images of $BaTiO_3$ nanoparticles, (c) SAED pattern of the precipitated $BaTiO_3$ nanoparticles. Reproduced with permission.[28] Copyright 2008, American Chemical Society.

$BaTiO_3$ nanoparticles. Surprisingly, the resulting $BaTiO_3$ nanoparticles exhibit some ferroelectricity which seems to contradict the core–shell model which states that the $BaTiO_3$ particles are supposed to be a pure cubic structure around 12 nm (Section 2).[75,76] Further analysis indicates that the high surface tension within the peptide cavities and the unique surface chemical features of the obtained $BaTiO_3$ nanoparticles due to the use of peptide template contribute to the observed unusual tetragonal phase at room temperature in such small $BaTiO_3$ nanoparticles. Therefore, it is possible to control the crystal structure of $BaTiO_3$ NCs by modifying their surface properties.[57]

Other soft templates such as peptides isolated by bacteriophages (viruses) were also used to produce tetragonal $BaTiO_3$ NCs at room temperature.[28] In a typical approach, peptides carried by two unique phages were added to the aqueous precursor solution, they rapidly induce the formation of tetragonal $BaTiO_3$ nanoparticles after an incubation step at pH = 6.8 for 2 h (Fig. 18a–c). The resulting $BaTiO_3$ NCs (50–100 nm) quickly precipitated and aggregated into larger clusters (0.3–0.5 μm in size). In a more recent work, researchers demonstrated that genetically engineered M13 virus can serve as a biotemplate for producing tetragonal $BaTiO_3$ nanoparticles at room template. More importantly, the resulting nanoparticles exhibit higher crystallinity and smaller sizes (10–30 nm in size).[178]

Despite lots of progress in producing 0D and 1D $BaTiO_3$ NCs, it remains a challenge to produce well-controlled three-dimensional (3D) $BaTiO_3$ nanostructures.[177,179] Recently, a bottom-up templating approach was developed for producing 3D $BaTiO_3$ nanostructures and other compounds with multiple components.[177] In a typical procedure, the 3D morpho helenor butterfly wing bio-organic template was coated with titania-bearing precursors in a computer-controlled layer-by-layer sol–gel process. The coated 3D templates were further heated to 450 °C to convert the precursor coating into nanocrystalline titania while preserved the 3D scales of the bio-organic wing template. In the following hydrothermal reaction, the pyrolyzed scales were converted into 3D nanocrystalline $BaTiO_3$ by the reaction between titania and barium acetate. As shown in the SEM images in Fig. 19, the butterfly morphology was successfully preserved and transferred into the $BaTiO_3$ NCs.

In addition to natural bio-organic templates, rationally-designed polymers have also been explored as templates for controlling the morphology of nanocrystals. Recently, Lin *et al.* proposed a novel generalizable templating approach to synthesize

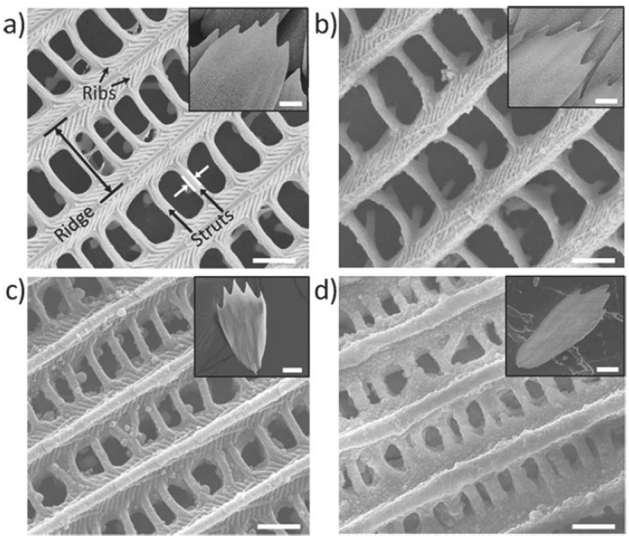

Fig. 19 SEM images of the wing scales from the morpho helenor butterfly wing at various stages of conversion: (a) the untreated morpho helenor butterfly wing as the starting template, (b) the scale coated with titania-bearing precursors, (c) the coated scale after pyrolysis, and (d) the final $BaTiO_3$ scale obtained by hydrothermal reaction. The insets show the low magnification images of each corresponding scale. Scale bars represent 1 mm in (a–d) and 20 mm in the insets. Reproduced with permission.[177] Copyright 2010, Wiley.

monodisperse colloidal nanocrystals, such as $BaTiO_3$, with controllable sizes and shapes.[50,180] The templates used are a series of star-like block co-polymers prepared by sequential atom transfer radical polymerization (ATRP) and copper-catalysed azide–alkyne cyclo additions (CuAAC). The templates include star-like poly(acrylic acid)-*block*-polystyrene (PAA-*b*-PS) and poly(acrylic acid)-*block*-poly(vinylidene fluoride) (PAA-*b*-PVDF). The precursors preferentially incorporate into the space occupied by the PAA blocks in star-like PAA-*b*-PS and PAA-*b*-PVDF. The coordination bonding between the metal-containing precursors and the carboxylic acid functional groups of PAA at elevated temperatures (180 °C) led to the selective formation of $BaTiO_3$ nanocrystals capped by PS and PVDF, respectively. As shown in Fig. 20b, the PVDF-capped $BaTiO_3$ nanoparticles are single crystals. They are highly uniform with diameters around 10 nm. The size of the $BaTiO_3$ nanoparticles can be easily tuned by changing the molecular weight of the inner PAA block where the crystal selectively grows. In addition, the covalently tethered

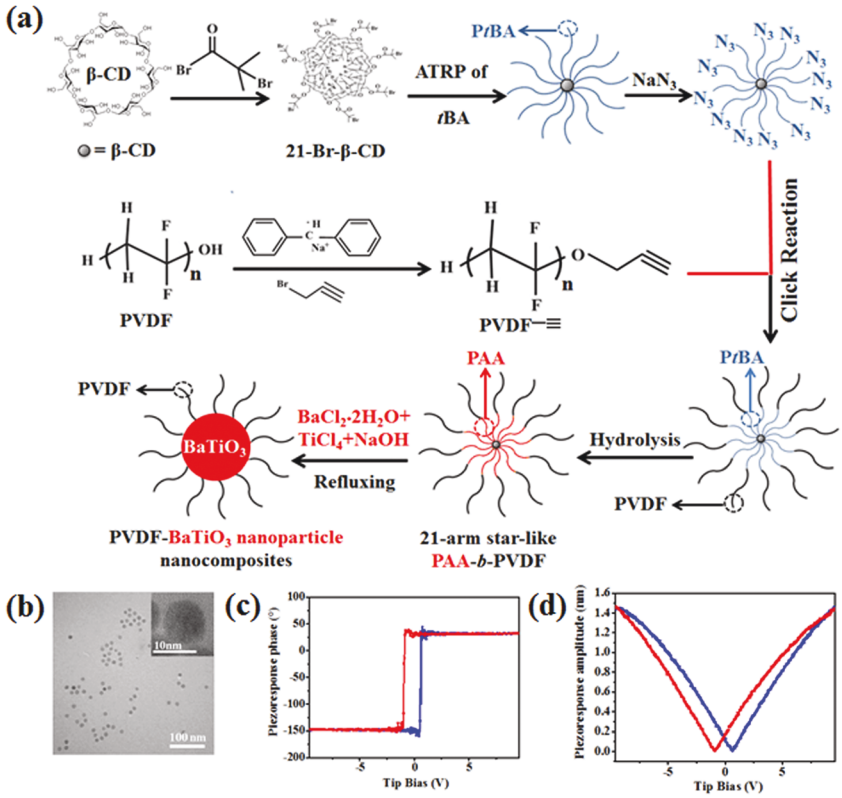

Fig. 20 (a) Scheme of the synthetic strategy for preparing $BaTiO_3$ nanoparticles by the nanoreactor approach. The amphiphilic star-like PAA-*b*-PVDF copolymer serves as the nanoreactor. (b) TEM images of templated $BaTiO_3$ nanoparticles demonstrating good uniformity with average diameters of 10 nm; (c and d) PFM results of individual $BaTiO_3$ nanoparticles with measured hysteresis loops signifying the switching behavior of the ferroelectric $BaTiO_3$ nanoparticles.[50] Copyright 2015, American Chemical Society.

polymer ligands on the surface of the $BaTiO_3$ nanoparticles (either PS or PVDF) facilitate easy dispersion of $BaTiO_3$ in organic solvents. The $BaTiO_3$ nanoparticles (D = 10 nm) prepared by this templating method exist in the ferroelectric tetragonal phase. This was further supported by piezoelectric force microscopy (PFM) (as shown in Fig. 20c and d). This flexible star-like copolymer templating approach can also be used to make nanocrystals of different structures (spherical, core@shell and hollow) by varying the type and number of polymer blocks. This approach has also proven effective in templating a wide assortment of functional nanocrystals for various applications.[180–185]

3.5. Molten salt methods

Nearly all of the methods discussed above are based on solution processes which yield relatively small quantities of materials and in many cases involve the use of extremely toxic and unstable precursors. In this context, developing gram-scale, environmentally-friendly methods with reproducible shape control is highly desirable for industrial and practical applications. The molten salt method utilizes molten salts as the solvent to grow NCs. It is one of the most efficient methods to address the issues of scalability and toxicity and has been shown to successfully grow various metal oxides.[186–188] In this approach, molten salt plays a critical role in the whole process as a reaction medium in which reactants dissolve and precipitate to produce the NCs in large quantities. The surface and interfacial energy balance between the constituents and the molten salt influences the morphology and overall shape of the resulting nanocrystals.[58]

In a seminal work, Wong *et al.* reported a simple, large-scale solid-state reaction for preparing single-crystal $BaTiO_3$ nanostructures in molten NaCl at 820 °C in the presence of a non-ionic surfactant.[189] The procedure is simple. Typically, barium oxalate (depending on the desired nanostructure), TiO_2, NaCl, and NP-9 (nonylphenyl ether surfactant) are mixed. The mixture is then placed in a quartz crucible, inserted into a quartz tube, annealed at high temperature, and subsequently cooled to room temperature. $BaTiO_3$ NCs are obtained by simply washing away the salt with water. TEM images of the center region of one of the $BaTiO_3$ nanowires are shown in Fig. 21. While a thin amorphous layer exists on the outer nanowire surface, the images clearly show that the $BaTiO_3$ nanowires are uniform and homogeneous. The 2-D lattice fringes confirm that the nanowire is crystalline with no defects or dislocations. Energy-dispersive X-ray spectroscopy (EDS) analysis (Fig. 21c) from different positions along the nanowires showed that the chemical composition of the nanowires is identical and the nanowires are essentially composed of Ba, Ti, and O. Moreover, the SAED patterns taken from different positions along the same nanowires are also identical. This indicates that the

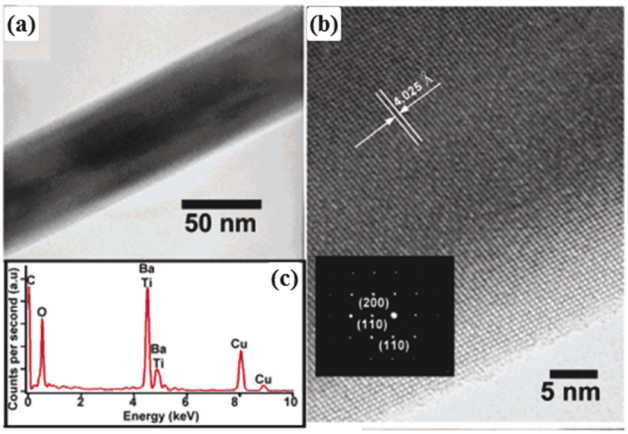

Fig. 21 (a) TEM and (b) HRTEM images of a single $BaTiO_3$ nanowire, the inset in (b) displays the selected area electron diffraction (SAED) pattern of the $BaTiO_3$ nanowire; (c) EDS spectrum of the as-prepared $BaTiO_3$ nanowires. Reproduced with permission.[189] Copyright 2003, American Chemical Society.

$BaTiO_3$ nanowires are single crystals. Due to its simplicity and generalizability, this method can likely be extended to the large-scale synthesis (gram quantity) of other important ferroelectric systems at the nanoscale such as $PbTiO_3$ and $BaZrO_3$.

The synthesis of other well-defined $BaTiO_3$ nanostructures, including spheres, cubes and rods, is also reported by employing a molten-salt synthesis method using $BaO/BaCO_3$ and TiO_2 in a NaCl–KCl molten salt mixture.[58] Three different morphologies were obtained with different barium precursors and shaped titanium precursors (spheres, rods and cubes). Spheres were synthesized by reacting $BaCO_3$ with spherical TiO_2. The cube and rod shapes were synthesized when BaO or $BaCO_3$ barium precursors reacted with rod-shaped TiO_2 as shown in the SEM images in Fig. 22. XRD results show no impurity peaks in the tetragonal phase nanostructures. In addition, the products are found to have the same shapes as the starting TiO_2 nanostructures (*i.e.*, spherical TiO_2 resulted in spherical $BaTiO_3$ while rod-shaped TiO_2 formed rod-shaped $BaTiO_3$). The shape of the products can thus be modified by changing the shape of the precursors. The growth mechanism for the cube and rod shapes is proposed in Fig. 23. (1) When the barium precursor dissolves faster than the titanium precursor (upper panel in Fig. 23), $BaCO_3$ dissociates and dissolves in the molten salt upon further heating. It then coats the TiO_2 nanostructures forming the shell. The barium precursors then react with the TiO_2 to form $BaTiO_3$ rods. (2) When the barium precursor dissolves slower than the titanium precursor (lower panel in Fig. 23), the rod shaped TiO_2 nanostructures can break apart prior to BaO dissolution. The reaction continues to occur in these smaller pieces leading to the formation of $BaTiO_3$ cubes.[58]

Recently, $BaTiO_3$ nanostrips were also synthesized in a surfactant-free molten salt process.[190] This surfactant-free approach is simple, general, and applicable to the growth of a number of 1D perovskite materials including $BaTiO_3$. In a typical procedure,

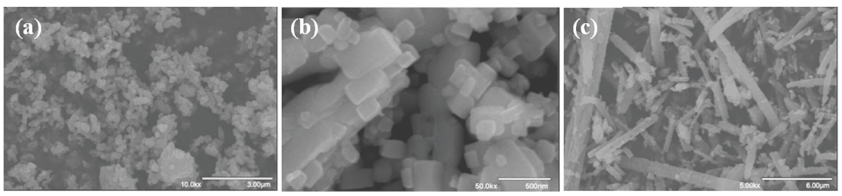

Fig. 22 SEM images of three different products: (a) spherical, (b) cubic, and (c) rod shaped $BaTiO_3$ nanocrystals synthesized using a surfactant-free molten salt method. Reproduced with permission.[58] Copyright 2009, American Chemical Society.

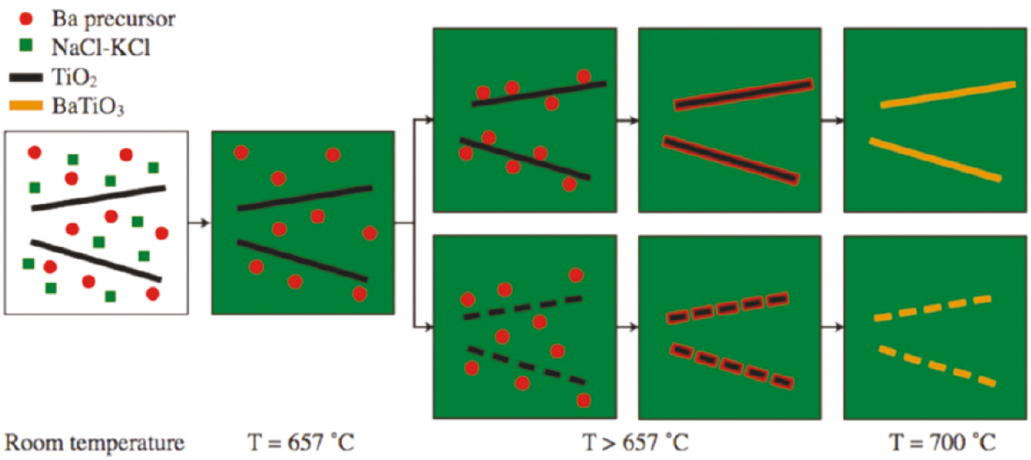

Fig. 23 Proposed synthetic mechanism for rod-shaped and cube-shaped $BaTiO_3$ in a molten salt. The upper panels are for rod-shaped $BaTiO_3$, and the bottom panels are for cube-shaped $BaTiO_3$. The difference in the two mechanisms hinges on the relative rates of dissolution of the barium and titanium precursors. Reproduced with permission.[58] Copyright 2009, American Chemical Society.

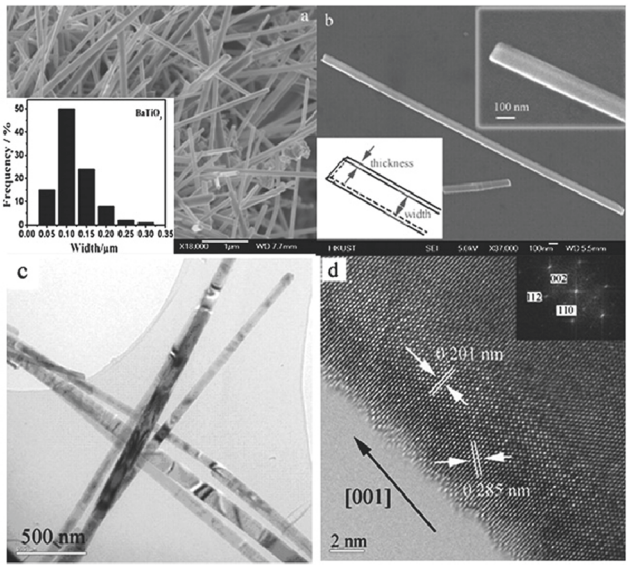

Fig. 24 (a) Low and (b) high magnification SEM images of as-prepared $BaTiO_3$ nanostrips, (c) a typical TEM image of $BaTiO_3$ nanostrips, (d) HRTEM image of a single $BaTiO_3$ nanostrip. Reproduced with permission.[190] Copyright 2009, Royal Society of Chemistry.

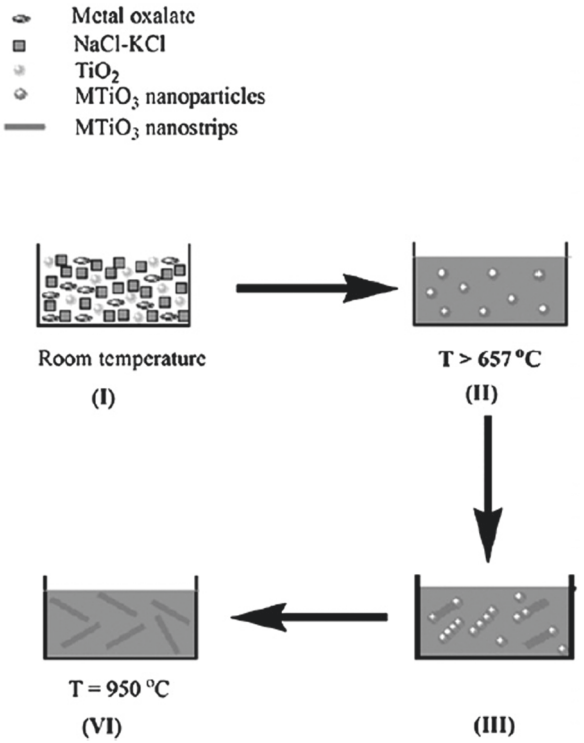

Fig. 25 Growth mechanism for $MTiO_3$ nanostrips (M stands for metal): (I) mixtures are ground at room temperature; (II) NaCl/KCl is melted when the reaction temperature exceeds 657 °C; (III) small crystal seeds aggregate along a polarization axis to form nanostrips; (IV) the perovskite nanostrips are formed at 950 °C. Reproduced with permission.[190] Copyright 2009, Royal Society of Chemistry.

barium oxalate is mixed with TiO_2 and NaCl–KCl. The mixture is then heated to the melting temperature of NaCl–KCl (657 °C) which facilitates the formation of $BaTiO_3$. As the temperature increases, $BaTiO_3$ seeds start to nucleate and grow preferentially along one direction and grow into nanostrips. SEM and TEM images of the as-synthesized $BaTiO_3$ samples are shown in Fig. 24. The resulting $BaTiO_3$ consists of well-defined, straight nanostrips with lengths from a few to tens of micrometers. As shown in the width-distribution histogram of the $BaTiO_3$ nanostrips in the inset of Fig. 24a, the $BaTiO_3$ nanostrips are clearly faceted and have a rectangular cross section with widths and thicknesses in the range of tens of nanometers. High magnification SEM (Fig. 24b) shows a rectangular end on the nanostrip with a width of approximately 120 nm and a thickness of 40 nm. High Resolution Transmission Electron Microscopy (HRTEM) of a single $BaTiO_3$ nanostrip shows lattice fringes, indicating their high crystallinity (Fig. 24d). This study is the first to report on perovskite nanostrips produced by a molten salt process with no added surfactant. A novel mechanism was proposed to explain the crystal growth process (Fig. 25). First, the barium oxalate, TiO_2 and NaCl–KCl powders are mixed together. Second, the molten salt is heated to melt (657 °C) and the reaction system forms a molten solution. At this point, chemical reactions can occur forming barium titanate seeds. Third, as the temperature further increases (950 °C), the seeds start to grow *via* the orientated attachment mechanism. Fourth, with continued growth the structures form into long nanostrips. Furthermore, it was suspected that the merging of the crystal seeds may lead to symmetry breaking along the axis because the individual seeds spontaneously self-polarize along the growth axis through the displacement of Ti^{4+} and O^{2-} ions in different directions.[190]

Compared to other soft chemical methods, the molten salt approach is advantageous due to its simplicity, low cost and high yield. It is the most promising method for industrial scale synthesis, but the resulting materials are usually of lower quality (*i.e.*, morphology and particle size are not well-defined). Moreover, the reaction process requires high temperatures, and the products generally cannot be well-dispersed in organic solvents (the organic ligand is usually decomposed at high temperatures) limiting its application in various areas including biomaterials, organic–inorganic hybrids, and film formation among others.

3.6. Sol–gel methods

The sol–gel approach is an established method for fabricating well-defined inorganic crystals from small molecules. The sol–gel process typically involves the conversion of monomers into a colloidal particle solution (''sol'') through hydrolysis and polymerization of a metal alkoxide which acts as the precursor for the formation of a gel-like system containing liquid and solid phases. After a drying process to remove the liquid phase in the ''sol'' and further calcination, inorganic crystals are obtained.[191–193] Depending on the solvent evaporation rate, temperature, reaction conditions and solvent type, the microstructure of the final products can vary greatly. Compared to other soft-chemical methods, the sol–gel process costs less, and is compatible with continuous manufacturing techniques for the massive production of powders.

As previously shown, most nanocrystal synthesis reactions rely on elevated reaction temperatures for crystallization (>140 °C). The low-temperature synthesis of perovskite nanocrystals is inherently difficult as it requires more complex synthesis techniques involving temperature and spatial precision.[60] Sol–gel techniques enable the nanoscale mixing of reagents which significantly reduces the length scale for diffusion and nucleation of crystalline materials. This enables the reaction temperature to be significantly reduced.[194] Recently, a vapor-diffusion sol–gel route has been presented for making high quality crystalline $BaTiO_3$ nanoparticles at lower temperatures without any templates. For example, $BaTiO_3$ nanoparticles were readily prepared by precisely controlling the $H_2O(g)$/HCl(g) vapor flowed into an organic solution of a bimetallic alkoxide ($BaTi[OCH_2CH(CH_3)OCH_3]_6$) at 16 °C. The controlled catalytic hydrolysis and condensation of the bimetallic alkoxide, as described by the following reaction, provides the required conditions for the nucleation and growth of small, high quality $BaTiO_3$ nanoparticles:

$$BaTi[OCH_2CH(CH_3)OCH_3]_6 + 3H_2O_{(g)} \xrightarrow{HCl_{(g)},\ 16\ ^\circ C} BaTiO_3 + 6HOCH_2CH(CH_3)OCH_3$$

TEM images in Fig. 26a, c and d show an assembly of partially-aggregated quasispherical $BaTiO_3$ NCs due to the absence of surfactants. A selected area electron diffraction pattern (Fig. 26b) supports the cubic structure of $BaTiO_3$ nanoparticles. This was the first to report on the synthesis of small, high quality $BaTiO_3$ nanoparticles at significantly lower temperatures (16 °C).

Other morphologies, such as thin films and fibers, have also been successfully prepared by sol–gel methods.[195,196] Compared with other deposition techniques for fabricating $BaTiO_3$ thin films, sol–gel methods are simpler and do not require high-vacuum levels.[195] It also enables better control of the composition and morphology of the resulting $BaTiO_3$ thin films. In one study, multiple $BaTiO_3$ thin films were deposited on different substrates *via* successive spin coating treatments of a 0.25 M Ba–Ti sol in air. After each layer deposition, films were heated to 350 °C on a hot plate to remove residual organics. The gel films were then decomposed by a heat treatment (600 °C) to form an intermediate crystalline phase of $BaTiO_2CO_3$ with a 5–10 nm grain size. These films are subsequently transformed to polycrystalline thin films with a grain size of 20–60 nm. This work showed that the morphology and dielectric properties of the resulting $BaTiO_3$ films is greatly influenced by the interfacial reactions between $BaTiO_3$ films and different substrate materials. The incorporation of high concentrations of water in the sols suppressed the formation of the intermediate phase enabling the film porosity to be significantly reduced.[195]

It was found that the properties of $BaTiO_3$ films produced by sol–gel techniques showed a heavy dependence on their processing parameters.[197] In one study of fabricating $BaTiO_3$ thin films using titanium isopropoxide ($Ti(OC_3H_7)_4$) as the titanium source with two different barium precursors, the sols were prepared by adding the titanium precursor into the barium precursor and refluxed at 80 °C. The filtered sols were then spin-coated onto different substrates and cured at different temperatures in air. The $BaTiO_3$ thin films prepared from two different barium sources were transparent and crack-free below 600 °C. Films prepared from the barium 2-ethyl hexanoate precursor were found to crystallize around 550 °C into a tetragonal polycrystalline phase. In contrast, films prepared from the barium hydroxide precursor crystallized into the cubic phase at 600 °C. In addition, the films prepared from the ethyl hexanoate precursor had higher porosities due to greater size reduction (*i.e.* shrinking) during heat treatment.[196]

Sol–gel synthesis methods are green and scalable growth techniques for the large production of perovskite nanoparticles (among nanoparticle compositions).[198] The solution-based sol–gel synthesis of $BaTiO_3$ typically relies on the hydrolysis of metal–organic precursors in alcohol-based solvents. It is essential that the concentration of water and metal–organic precursors be well controlled so that the hydrolysis and cross-linking of the metal–organic precursors is slow. This enables the production of uniform and aggregate-free colloidal perovskite nanoparticles that are highly crystalline and pure. This green process can realize a nearly quantitative yield of perovskite nanocrystals and demonstrates its great promise in the fabrication of high performance dielectric thin films potentially in industrial scale quantities.[198]

Researchers have developed a rapid, low-temperature route for the synthesis of nanocrystalline $BaTiO_3$ based on a sol–gel approach.[199] The $BaTiO_3$ sols, $BaTiO_3$ gels, and $BaTiO_3$ precipitates were synthesized *via* the controlled hydrolysis of metal–organic precursors in mixtures of different alcohols and ethylene glycol (EG), diethylene glycol (DEG), triethylene glycol (TEG), or tetraethylene glycol (TTEG) solvents. $BaTiO_3$ nanocrystals were produced with sizes of 2.8 and 5.1 nm in 15 min to 2 h.

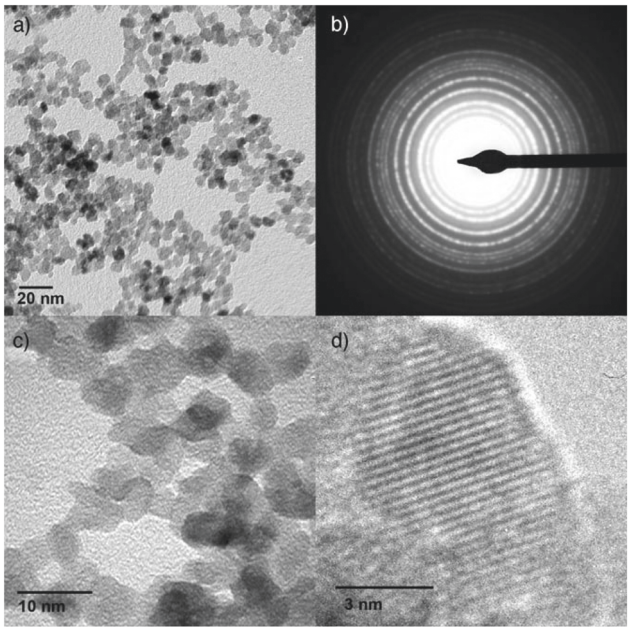

Fig. 26 (a, c and d) TEM images of $BaTiO_3$ nanoparticles formed by a sol–gel approach (different magnifications). (b) SAED pattern of $BaTiO_3$ nanoparticles. Reproduced with permission.[60] Copyright 2006, Wiley.

The small $BaTiO_3$ nanocrystalline sols are suitable for coating, spraying, and printing techniques, making them an economic material for quickly fabricating highly crystalline $BaTiO_3$ thin films.[199]

In one study, the crystal structure of $BaTiO_3$ nanocrystals were converted from amorphous to crystalline morphologies.[200] In the work, small $BaTiO_3$ nanocrystals (less than 10 nm) were grown *via* a vapor diffusion sol–gel method at room temperature. Mixed bimetallic alkoxide precursors dispersed in *n*-butanol/2-methoxypropanol were first transferred to a reaction flask. The flask was then bubbled with an HCl solution in nitrogen gas to produce a $N_2/HCl/H_2O$ vapor across the precursor solution. During the vapor flow, the solution viscosity gradually increased, resulting in an amorphous metal–organic gel. The hydrolysis and condensation of the bimetallic alkoxide $BaTi(OCH_2CHCH_3OCH_3)_6$ caused the solution to gel after 8 h of reaction. After reaction for 12 h, 3–6 nm diameter $BaTiO_3$ nuclei formed in an amorphous metal–organic matrix. These nuclei continued to grow, yielding individual 9 nm diameter $BaTiO_3$ nanocrystals after 30 h. After reaction for 72 h, the amorphous-to-crystalline phase transition was complete, and the resulting 9 nm $BaTiO_3$ nanocrystals possessed a cubic phase.[201] In Table 1, we summarized the results and experimental conditions for synthesizing $BaTiO_3$ nanocrystals by the various synthetic methods addressed herein.

4. Ferroelectric properties of individual $BaTiO_3$ nanostructures

4.1. Ferroelectricity at the nanoscale

Ferroelectricity describes a material possessing a spontaneous electrical polarization that can be switched under the application of an external electric field. This switchable polarization is ideal for use in devices for memory storage (writeable memory) and microelectronics.[202] Nanoscale ferroelectric materials make it possible to design ferroelectric devices that can operate at the atomic scale. However, nanoscale ferroelectric materials behave differently than their bulk ferroelectric counterparts. The characteristic properties of bulk ferroelectrics relate to the macroscopic polarization of domains to achieve energy minimization. In contrast, nanoscale ferroelectrics possess continuous uniform polarization across the whole structure.[202] At the nanoscale, there is a large surface-to-volume ratio. This essentially means that the role of surface effects and surface interactions (*i.e.* interfaces) becomes more important. Consequently, surface effects play an important role in nanoscale ferroelectricity.[203] The direct probing of ferroelectricity in individual $BaTiO_3$ nanostructures is essential for developing their applications in nanoscale devices and understanding the effects of size and surface area on the nanoscale.

4.2. Probing the ferroelectricity of individual $BaTiO_3$ NCs by piezoresponse force microscopy (PFM)

As previously described, the rapid development of electronic devices based on ferroelectric nanomaterials has necessitated the study of ferroelectric properties at the nanoscale. One of the most promising applications is data storage, where the polarization behavior of ferroelectrics is particularly important because the polarizations are both stable and switchable despite the small size. This high density of nanoscale, writeable polarization is essential for storing greater amounts of information in smaller areas (*i.e.* high information storage density): a requirement of all electronic devices.[114] The manipulation of ferroelectric polarization on individual $BaTiO_3$ NCs has been realized *via* piezoresponse force microscopy (PFM). This technique is based on the measurement of the local piezoelectric deformation (*i.e.* physical shape change) of a ferroelectric material caused by an applied external electric field.[204] As shown in a typical PFM setup in Fig. 27a, AC and DC voltages are applied to the sample under detection and the cantilever. The sample expands and contracts in response to the applied electric field, and the oscillation signal of the cantilever are read out as amplitude signal (Fig. 27b) and phase signal (Fig. 27c). The 180 degree phase change (Fig. 27c) signifies the switching behavior of ferroelectric materials. PFM (Fig. 28) can be operated in two modes: vertical PFM mode and lateral PFM mode. In the vertical PFM mode, the locally-induced vertical deformation is measured by the deflection of an AFM cantilever to measure polarization in the normal direction (Fig. 28a). In the lateral PFM mode, the locally-induced shear deformation of the sample is measured by the twisting of the AFM cantilever to measure polarization in the plane (Fig. 28b). In addition to domain visualization, the conductive tip can also be used to modify the initial domain structures (*e.g.* read and write the polarization). By applying a DC voltage larger than the coercive voltage of the ferroelectric sample between the tip and the bottom electrode, a local polarization can be induced.[204] The small size of the PFM probe tip allows local ferroelectric properties to be characterized with high resolution and precision.[62,63,204,205] In this section, a review of recent advances in PFM characterization and the manipulation of different $BaTiO_3$ nanostructures to demonstrate their unique ferroelectric behavior is presented.

In their seminal work, Park *et al.*[86,206] successfully induced and manipulated the electrical polarization of several nanoscale domains in a single crystalline $BaTiO_3$ nanowire by an external electric field. This work demonstrated the presence of ferroelectricity despite the small radial dimension of the nanostructures. The ferroelectric properties of individual $BaTiO_3$ nanowires were investigated using scanning probe microscopy (SPM) (Fig. 29). A voltage (V_{tip}) was applied to the conductive tip in order to induce or ''write'' local electric polarization normal to the nanowire long axis. Next, the written polarization was probed or ''read'' by measuring the shift in the resonance frequency of the SPM cantilever while scanning with a small V_{tip} using electrostatic force microscopy (EFM). As shown in Fig. 29a, the as-deposited nanowires show no obvious EFM contrast. This indicates that pristine nanowires do not exhibit polarization normal to the wire axis. After the writing procedure, a local electric polarization normal to the wire axis was induced. By changing V_{tip} from +10 V to −10 V, the polarization direction could be reversed (Fig. 29a). The written polarizations could be

Table 1 Experimental conditions for the synthesis of $BaTiO_3$ nanocrystals *via* various synthetic methods

Synthesis methods	Precursors	Reaction conditions	Morphologies	Phases	Ref.
Organo-metallic	$BaTi(O_2CC_7H_{15})[OCH(CH_3)_2]_5$	Injected precursors at 140 °C under argon or nitrogen; reacted at 100 °C for over 48 h	8 nm diameter $BaTiO_3$ nanoparticle	Cubic	49
Organo-metallic	$BaTi[OCH(CH_3)_2]_6$	280 °C for 6 h	30 nm diameter $BaTiO_3$ nanorod	Cubic	54
Hydrothermal	$Ba(OH)_2{\cdot}8H_2O$ and anatase TiO_2	1–72 h at 90 °C	Nanoparticle		138
Hydrothermal	$Ba(OH)_2{\cdot}8H_2O$ and rutile TiO_2 powder; Ba/Ti ratio varies from 1.2 to 1.8	160 °C for 3–24 h	40–50 nm diameter nanoparticle	Cubic	152
Hydrothermal	$TiCl_4/Ba(NO_3)_2$	400 °C, 30 MPa, 8 ms	90–260 nm nanoparticle	Cubic	153
Hydrothermal	Sample A: $Ti(OH)_4$ and $Ba(OH)_2{\cdot}8H_2O$ Sample B: TiO_2 and $Ba(OH)_2{\cdot}8H_2O$	100 °C for 5 h	Sample A: average 65 nm nanoparticle Sample B: 80 nm coarse-faceted nanoparticle	Cubic	154
Hydrothermal	$Ba(OH)_2$ and TiO_2 particles	170 °C for 3 days	Nanowires, with diameters of 50–200 nm and lengths from a few to tens of μm	Cubic with tetragonal symmetry	48
Hydrothermal	$Ba(OH)_2{\cdot}8H_2O$ and TiO_2	80 °C for 12 h	Bowl-like structures with 100–200 nm in diameter	Tetragonal	51
Hydrothermal	$Ba(NO_3)_2$ and $Ti(Bu)_4$	135 °C for 18 h	22 nm cube-like $BaTiO_3$	Cubic	53
Solvothermal	Metallic barium and titanium isopropoxide	200 °C for 48 h	4–5 nm nanoparticles	Cubic	161
Solvothermal	$Ba(OH)_2{\cdot}H_2O$ and $Ti[O(CH_2)_3{\cdot}CH_3]_4$	200 °C for 48 h	106.69 nm diameter nanoparticles	Tetragonal	163
Hard templating	Metal acetate $Ba(OAc)_2$ Titanium isopropoxide $Ti(OPri)_4$	700 °C for 6 h	50 μm-long tubes with 200 nm outer diameters	Cubic	174
Hard templating	$Ba(NO_3)_2$ and $(NH_4)_2TiF_6$	Near-ambient conditions for 24 h	$BaTiO_3$ nanotubes with diameter of 250 nm and length of 2.5 μm	Cubic	173
Hard templating	BATIO 9101 polymeric precursor	First anneal in air at 300 °C, then at 850 °C for 1 h for crystallization	$BaTiO_3$ nanotubes with diameters from 50 nm to several micrometers	Tetragonal	201
Hard templating	Titanium(IV) isopropoxide and barium acetate	700 °C for 15–30 min	Nanorods of 125–200 nm in diameter and 10 μm in length		175
Hard templating & hydrothermal	$Ba(OH)_2$ and TiO_2	200 °C for 2 h	Well-ordered arrays of $BaTiO_3$ nanotubes	Tetragonal	176
Hard templating	$Ba(AC)_2$ and $Ti(C_4H_9O)_4$	Solidifying the composite in a vacuum desiccator for 24 h and subsequently calcining the sample at 700 °C	Macroporous $BaTiO_3$ nanoparticles		178
Hard templating & hydrothermal	$Ba(OH)_2$, titanium(IV) bis(ammonium lactate) dihydroxide (TALH)	120 °C for 1 day	Hollow $BaTiO_3$ spheres; diameter dictated by the diameter of the template		56
Soft templating	$BaTi(O_2CC_7H_{15})[OCH(CH_3)_2]$	Irradiated by long-wave UV light (355 nm) for 10 h	6–12 nm diameter $BaTiO_3$ nanoparticles	Tetragonal	57
Soft templating	Titanium(IV) isopropoxide and barium acetate	Heated to 220 °C in a microwave reaction system for 10 h	Heated to 220 °C in a microwave reaction system $BaTiO_3$ butterfly	Tetragonal	179
Soft templating	$TiCl_4$ and $BaCl_4$	180 °C for 2 h	10 nm $BaTiO_3$ nanoparticles	Tetragonal	50
Molten salt	Barium oxalate and anatase TiO_2	Annealed at 820 °C for 3.5 h	$BaTiO_3$ nanotubes	Cubic	117
Molten salt	$BaCO_3$ and TiO_2	700 °C for 1 h	Rod-shaped $BaTiO_3$	Tetragonal	58
Molten salt	Barium oxalate and TiO_2	950 °C for 5 h	$BaTiO_3$ nanostrips	Tetragonal	192
Sol–gel	$BaTi[OCH_2CH(CH_3)OCH_3]_6$	16 °C for 15 h	6 nm $BaTiO_3$ nanoparticles	Cubic	60
Sol–gel	$Ba(OiPr)_2$, $Ti(OiPr)_4$	45–55 °C for 2–10 h	6.6 nm $BaTiO_3$ nanoparticles	Cubic	199

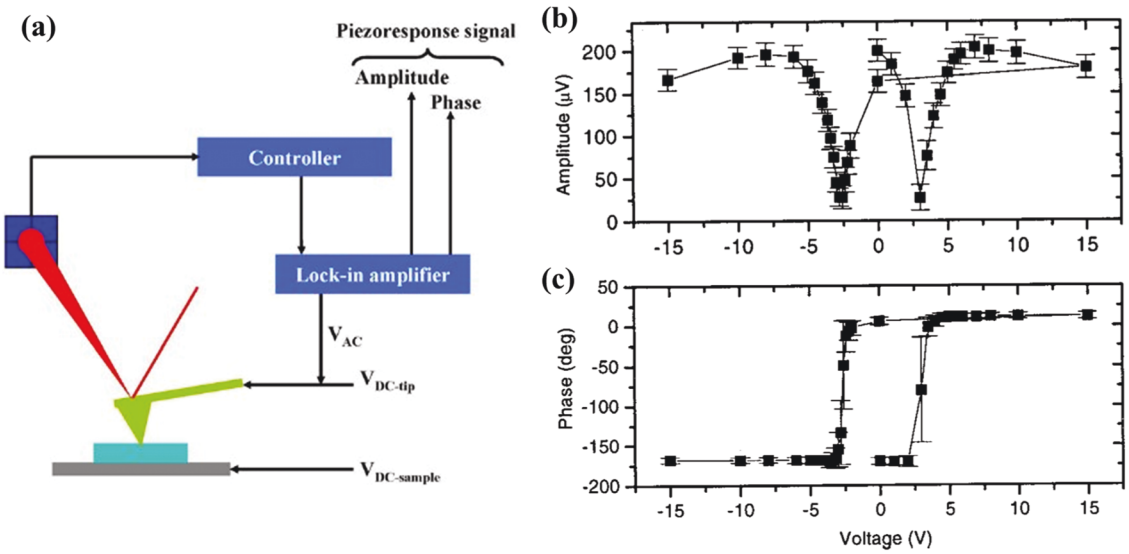

Fig. 27 (a) Schematic representation of PFM setup. (b) Amplitude and (c) phase signals. Reproduced with permission.[257] Copyright 2001, American Institute of Physics.

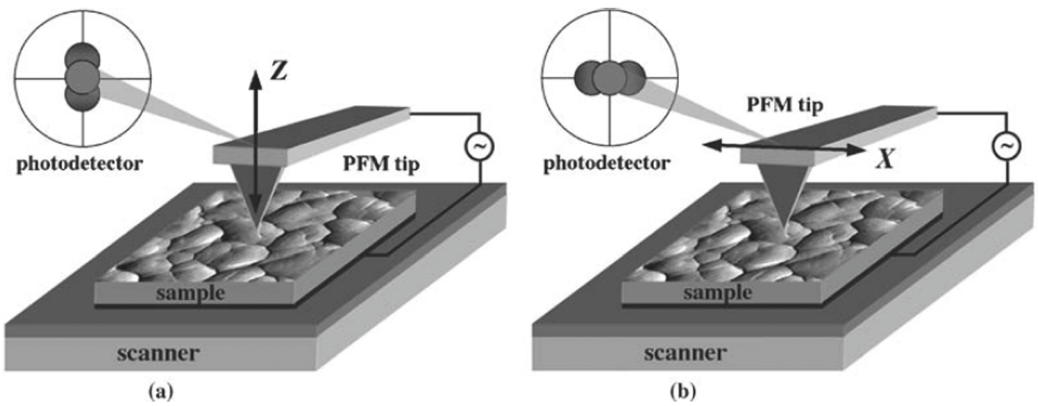

Fig. 28 Schematic of piezoresponse force microscopy (PFM) signal detection in the (a) vertical and (b) lateral mode. Reproduced with permission.[204] Copyright 2006, Springer.

retained for more than 5 days as shown in Fig. 29b. The polarization reversal shown in Fig. 29c indicated a clear memory effect (*i.e.* remanence-to-saturation ratio close to 1) in this ferroelectric nanowire. The EFM images in Fig. 30b–f show multiple polarization domains as small as 100 nm^2 can be induced and manipulated (*i.e.* written, read and rewritten) on a single nanowire. These observations make ferroelectric nanowires an attractive material for future information storage as a memory component. Nanowires may be well-suited for applications in nonvolatile memory (NVM) devices.

Subsequently, Park *et al.* also explored the dependence of the ferroelectric phase transition temperature (T_C) on nanowire diameter (d_{nw}) through variable-temperature scanning probe microscopy.[105] The ferroelectric phase transitions were investigated by measuring the time variation of the EFM signal from individual nanowires as a function of T. As shown in Fig. 31a, a series of EFM images were obtained from a 25 nm diameter nanowire at two different temperatures (below and above T_C). Below T_C, the signal remained stable for more than 7 days. This indicates that the nanowire retained its ferroelectric character. In contrast, above the T_C, the induced polarization was not stable and gradually decayed over time. The T_C obtained as a function of the nanowire diameter (d_{nw}) showed that the T_C in larger diameter nanowires approached that of the bulk material (400 K) but quickly reduced as d_{nw} decreased (Fig. 31b). Based on these measurements, the diameter at which T_C falls below room temperature is roughly 3 nm. In other words, $BaTiO_3$ nanowires must have diameters less than 3 nm to have ferroelectric properties (*i.e.* read–write polarization domains) at room temperature. Extrapolation of the data indicates that nanowires with d_{nw} as small as 0.8 nm can support ferroelectricity, but at temperatures below room temperature. Moreover, the inset of Fig. 31b clearly shows that the reduction of T_C is inversely proportional to d_{nw}. This suggests that the suppression of ferroelectricity is a consequence of a depolarizing field (*i.e.* a field caused by an incomplete balance of surface charges that opposes the

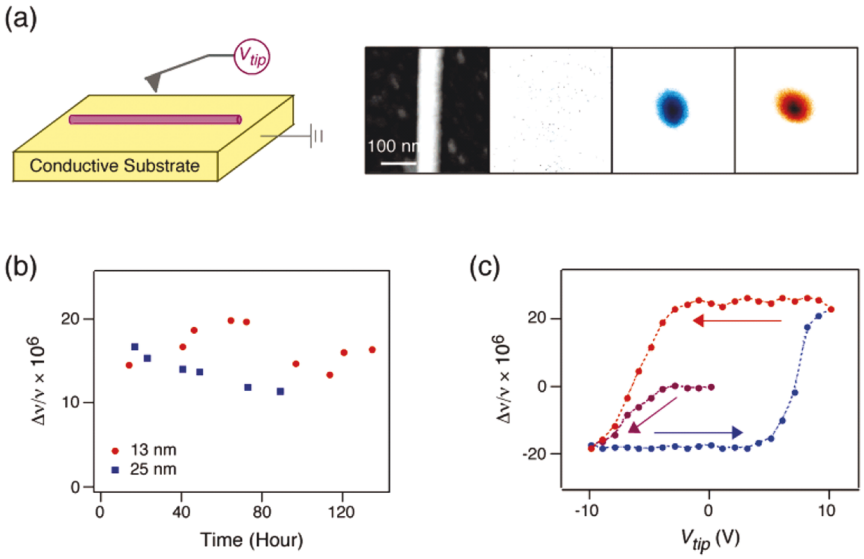

Fig. 29 (a) Schematic diagram of the PFM tip and substrate setup. The panels on the right show a topographic image of a $BaTiO_3$ nanowire and electrostatic force microscopy (EFM) images obtained from the same wire. (b) Plot of the cantilever resonance frequency shift as a function of time for two nanowires with different diameters; 13 nm (circles) and 25 nm (squares). (c) Plot of resonance frequency shift as a function of the writing voltage for a $BaTiO_3$ nanowire with a 15 nm diameter. Reproduced with permission.[206] Copyright 2002, American Chemical Society.

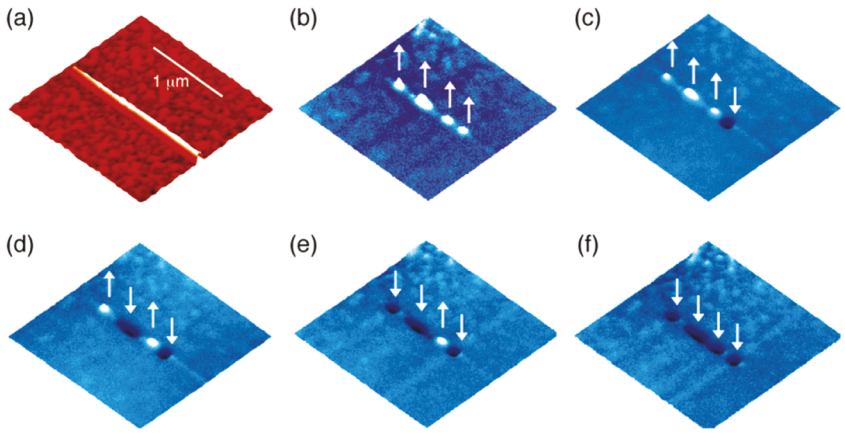

Fig. 30 (a) Three-dimensional image of a single $BaTiO_3$ nanowire, and (b–f) successive EFM images showing four separate polarization domains that can be independently adjusted by an external electric field in a fashion analogous to binary. Reproduced with permission.[206] Copyright 2002, American Chemical Society.

induced polarization) as previously described.[105] When combined with density functional theory (DFT) results for naked and coated $BaTiO_3$ surfaces, it was found that the nanowire ferroelectricity is stabilized by the hydroxyl and carboxyl groups adsorbed to the surface in $BaTiO_3$ nanowire coatings. These adsorbed chemicals can balance the surface charges and stabilize the ferroelectricity. This supports the observation of stable ferroelectric domains in small $BaTiO_3$ nanowires.

Recently, larger crystalline $BaTiO_3$ nanowires (50–80 nm in diameter and 10 μm in length) have also been characterized by piezoforce microscopy techniques.[52] PFM images of $BaTiO_3$ nanowires before and after the poling process are shown in Fig. 32. No obvious contrast can be observed before the poling process, indicating that the original $BaTiO_3$ nanowire shows no polarization (Fig. 32a). After poling *via* application of an external electric field, the PFM readings show two different states with the as-grown state marked "1" and the single-poled state marked "2" (Fig. 32b). The latter indicates the formation of a local polarization domain normal to the wire axis. However, due to presence of internal and external hydroxyl defects and oxygen vacancies (*i.e.* a depolarization field), the induced polarization decayed slowly in air over a day.[52]

In addition to nanowire structures, ferroelectricity in lower dimensional nanostructures can also be detected by PFM probes. Itoh *et al.* directly observed ferroelectricity in $BaTiO_3$ nanoparticles with sizes as small as 25 nm using PFM technique.[207] As shown in Fig. 33a and b, the nanoparticles are tightly aggregated with thickness on the order of a single-particle dimension in the majority of places measured. The hysteresis loops for $BaTiO_3$ nanoparticles with two different sizes (Fig. 33c and d)

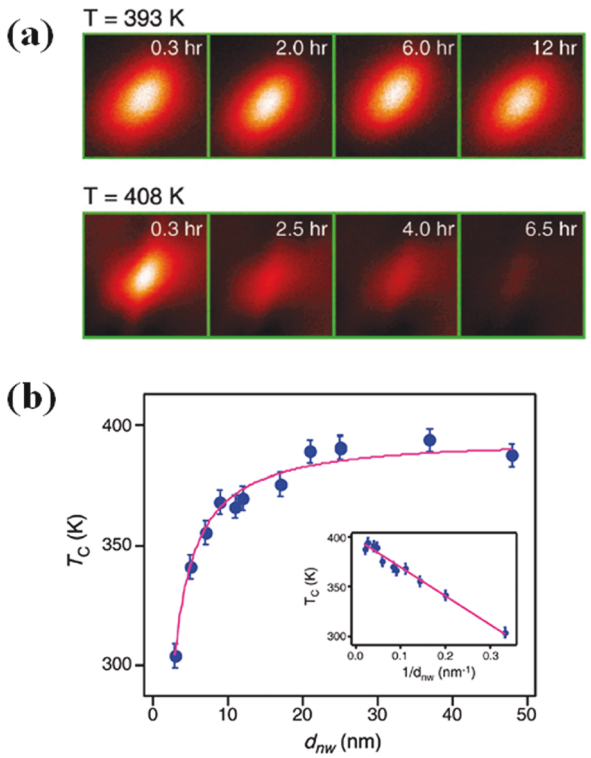

Fig. 31 (a) EFM images over time (size: 300 × 300 nm^2) for a 25 nm diameter nanowire after polarization writing below (393 K) and above (408 K) the phase transition temperature; (b) ferroelectric phase transition temperature (T_C) as a function of nanowire diameter. Reproduced with permission.[105] Copyright 2006, American Chemical Society.

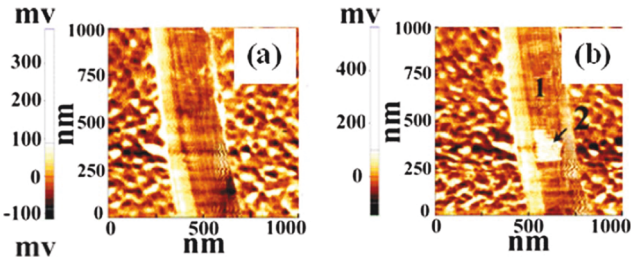

Fig. 32 PFM images of a single $BaTiO_3$ nanowire before (a) and after (b) the poling process (*i.e.* writing step). The PFM signals exhibit two different states with the as-grown state marked as "1" and the single-poled state marked as "2" indicating the presence of a local electric polarization normal to the wire axis. However, due to the existence of bulk hydroxyl defects and oxygen vacancies, the induced polarization slowly decays in air over 12–24 h. Reproduced with permission.[52] Copyright 2009, American Institute of Physics.

unambiguously confirm the ferroelectric component, coexisting with a more dominant paraelectric component. The remnant piezoresponse was smaller in 25 nm particles than that in 35 nm particles. However, the opposite trend was observed for the coercive voltage with the 25 nm particles having a larger value. This observation also supports a clear particle size effect on the ferroelectric properties.

The ferroelectric properties of ordered arrays of $BaTiO_3$ nanodots prepared by pulsed laser deposition (PLD) were also investigated using PFM.[208] As shown in Fig. 34b, the bright regions in the piezoresponse domain image show that the dots have a downward-oriented polarization. The polarization was weak because there was minimal ferroelectric phase (tetragonal) present in the arrays. Despite the weak polarization, the arrays can still be switched by PFM (Fig. 34c and d). There are a few factors that remain to be investigated including improving the uniformity of the templated arrays, and understanding the relationship between polarization and size in these structures.[208]

Nanocrystals with unusual shapes can also be characterized with PFM. For example, the ferroelectricity of bowl-like $BaTiO_3$ nanoparticles synthesized by a hydrothermal method has been investigated by PFM (Fig. 35). The well-defined bowl-like nanoparticles (Fig. 35A) have a uniform size 100–200 nm in diameter including the particle rim (I) and the center depressed area (II) shown. Both the characteristic "butterfly" loops and piezoelectric hysteresis loops were shown in Fig. 35B. The effective piezoelectric coefficient (d_{33}* = 28 pm V^{-1}) is calculated based on the "butterfly" loop. These results clearly show that the polarization remains both switchable and spatially dependent in more unusually-shaped nanocrystals.[51]

In traditional PFM measurements, an oscillatory AC test signal is applied between the probe and a conductive sample substrate to induce a local oscillatory deformation due to the converse piezoelectric effect (Fig. 36a). This setup has limitations whenever a high bias is required for in-plane polarization switching or a sample requires uniform polarization to avoid electric breakdown.[209] To resolve this problem, a new experimental approach has been designed for the study of nanoscale piezoelectric properties in one-dimensional nanowires.[209] As shown in Fig. 36b, a DC bias is applied along the ferroelectric nanowire axis. This provides in-plane polarization control and allows for the investigation of ferroelectric hysteresis and piezoelectric response to shear in nanowires using PFM. Using this new PFM approach, Wang *et al.* successfully showed the ferroelectric and piezoelectric properties of $BaTiO_3$ by measuring the polarization saturation along the long axis of a one-dimensional nanowire.[209] The 180 degree phase change in the square loop (Fig. 36c) and the classical butterfly amplitude loop (Fig. 36d) indicated the existence of polarization along the axial direction of single $BaTiO_3$ nanowire.[209]

To further improve the performance of $BaTiO_3$ nanomaterials, hybrid nanocomposite materials integrating $BaTiO_3$ and polymers with complementary properties have been prepared. These nanocomposites offer the potential for superior performance, processability and scalability far beyond pure $BaTiO_3$ nanostructures. Ferroelectric nanocomposites are the focus of the following sections.

5. Dielectric properties of $BaTiO_3$–polymer nanocomposites

5.1. Theoretical models for the dielectric properties of polymer–ceramic nanocomposites

In a two-phase composite material made of high dielectric constant ceramic fillers and a polymer matrix with a high

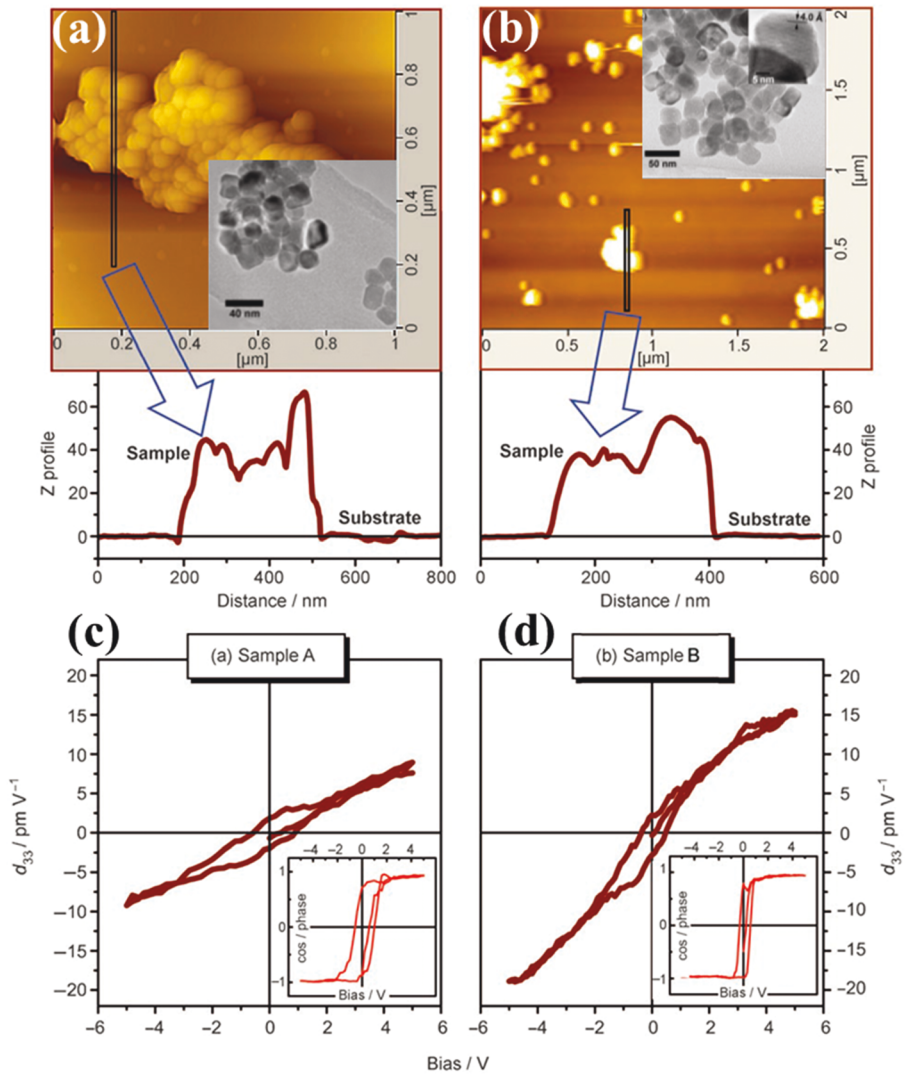

Fig. 33 (a and b) Large-area AFM images along with corresponding thickness profiles of the 25 nm (inset in (a)) and 35 nm (inset in (b)) deposits; (c) and (d) the piezoresponse *versus* bias voltage curves from the two samples with a clear hysteresis component.[207] Copyright 2006, Wiley.

breakdown strength, the filler provides the dielectric properties while the matrix provides mechanical properties. A number of models have been proposed for predicting the dielectric properties of polymer–ceramic composites of various compositions. Depending on the ceramic filler loading and the polymer and ceramic components interaction, three generally accepted models have been developed for explaining the observed properties. These models are the Maxwell–Garnett formulation, the Bruggeman self-consistent effective medium approximation, and the Jaysundere–Smith formulation.[210]

5.1.1. Maxwell–Garnett equation. Consider the mixing condition when ceramic particles of permittivity k_f (where the volume fraction is ϕ_f) are mixed into an isotropic polymer matrix of dielectric permittivity k_m (where the volume fraction is ϕ_m, $\phi_m = 1 - \phi_f$). In this model, the permittivity of the two-component composite (k_c) lies between a lower permittivity ($k_{c,min}$) and an upper permittivity ($k_{c,max}$) value ($k_{c,min} \leq k_c \leq k_{c,max}$) with the two limiting values described by the following equations:[211]

$$k_{c,min} = \frac{k_m k_f}{k_m \phi_f + k_f \phi_m} \quad (1)$$

$$k_{c,max} = k_m \phi_m + k_f \phi_f \quad (2)$$

The lower bound ($k_{c,min}$) is described by a series model in which both the polymer and ceramic components are connected in two dimensional layers to form layers parallel to the electrode films (eqn (1)). The upper permittivity ($k_{c,max}$) corresponds to a parallel model in which each phase is connected in two dimensions where the layers formed are perpendicular to the electrode film.[211] Practical two-phase composites are described by this mixing model in which some average between the two pure arrangements exists. This model is the simplest to understand, however it tends to deviate for larger concentrations of filler. It also doesn't account for the possibility of aggregation of the various components as well as not considering the impact of particle shape on composite permittivity.

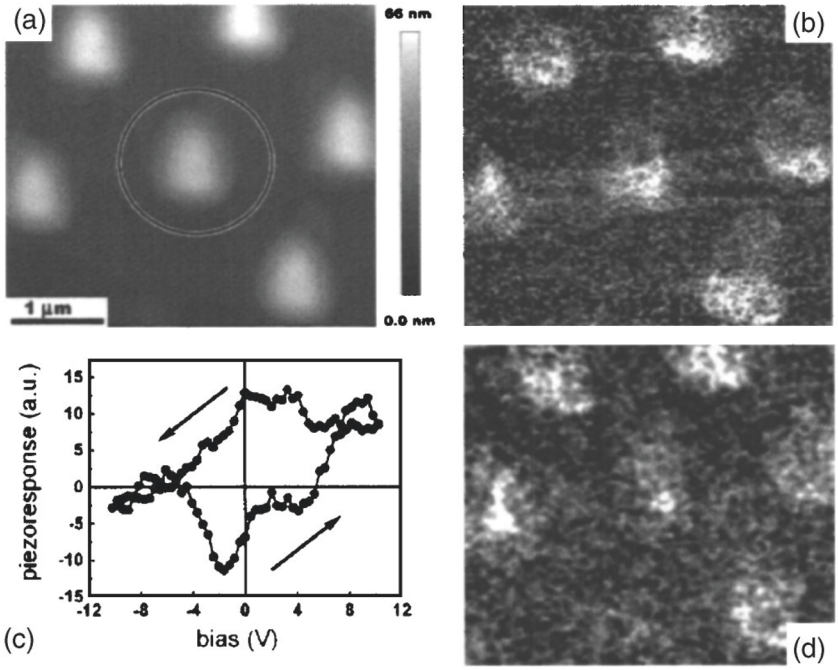

Fig. 34 AFM and PFM characterization of a $BaTiO_3$ nanodot array: (a) topography, (b) ferroelectric domain structure prior to switching, (c) switching piezoresponse hysteresis loop, and (d) ferroelectric domain structure after switching. Reproduced with permission.[208] Copyright 2005, American Institute of Physics.

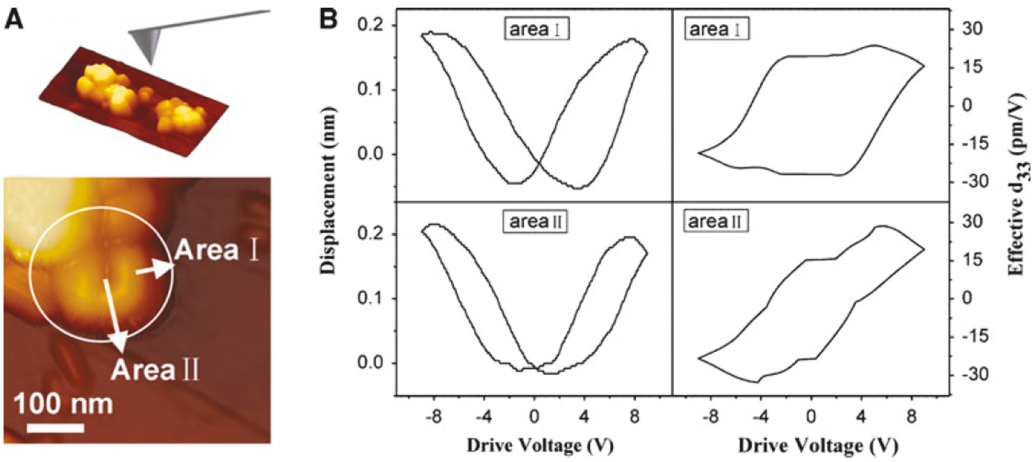

Fig. 35 (A) AFM images of bowl-like $BaTiO_3$ nanoparticles; (B) local piezoelectric displacement-voltage loops and effective piezoelectric coefficient d_{33}* of the bowl-like particles at the edge (area (I)) and in the central concave space (area (II)). Both areas show the characteristic butterfly loops and piezoelectric hysteresis loops. These results demonstrate that the polarization is switchable. Reproduced with permission.[51] Copyright 2010, Springer.

Further efforts to model the dielectric properties of two-phase composites have led to a more accurate equation (the Maxwell–Garnett equation) for predicting the dielectric properties of composites. The Maxwell–Garnett equation is valid for low spherical ceramic filler concentrations and is described by the following equation:[211,212]

$$k_c = k_m\left[1 + \frac{3\phi_f(k_f - k_m)}{(1-\phi_f)(k_f - k_m) + 3k_m}\right] \quad (3)$$

For more general situations when the ceramic particles are not a uniform spherical shape, a modified version of the Maxwell–Garnett equation has been developed. This equation takes into account the geometry of the dispersed filler particles in the polymer matrix and is more accurate in predicting the dielectric properties of two-phase composites. The more general Maxwell–Garnett equation considering the geometry of dispersed particles is described by eqn (4),[211] where the parameter A is the shape-dependent depolarization factor (A = 1/3 for spherical particles, $A > 1/3$ for oblate ellipsoid particles limiting to disc shapes, and $A < 1/3$ for prolate ellipsoid particles limiting to rods).

$$k_c = k_m\left[1 + \frac{\phi_f(k_f - k_m)}{A(1-\phi_f)(k_f - k_m) + k_m}\right], \quad \text{for } \phi_f < 0.1 \quad (4)$$

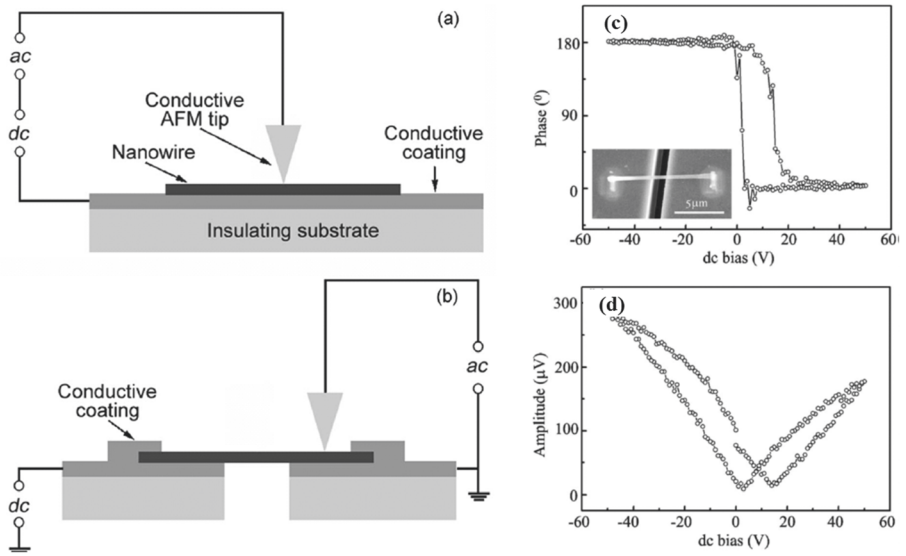

Fig. 36 Schematic of the (a) biasing condition in conventional lateral PFM; (b) axial biasing setup proposed by Wang *et al.*; (c) lateral PFM in-field hysteresis phase loop; (d) lateral PFM in-field hysteresis amplitude loop. Reproduced with permission.[209] Copyright 2006, American Institute of Physics.

The more accurate Maxwell–Garnett equation is also reasonable for composites consisting of a continuum polymer matrix with low concentrations of ferroelectric particle filler ($\phi_f < 0.1$).[213]

5.1.2. Bruggeman self-consistent effective medium approximation. In contrast to the Maxwell–Garnett equation, the Bruggeman self-consistent effective medium approximation treats each phase equally and assumes that all components are randomly mixed together with no requirement for uniformity of the filler particle dispersion within the polymer matrix.[213,214] This theory has been widely used to predict the dielectric and optical properties of composite materials. It provides more accurate property prediction at higher spherical filler content (ϕ_f up to 0.5). Bruggeman's formula is described by eqn (5):[211]

$$\frac{k_f - k_c}{{k_c}^{1/3}} = \frac{(1-\phi_f)(k_f - k_m)}{{k_m}^{1/3}} \quad (\phi_f < 0.5) \tag{5}$$

5.1.3. Jaysundere–Smith equation. In the situation where a low concentration of filler is present in the composite, the interaction between filler particles is too weak due to a large separation distance between neighbors. Thus, this interaction is neglected. However, at higher filler concentrations when the particles are more closely located to one another, neighboring filler particles have the potential to interact with one another and produce internal electrical fields due to local dipole moment formation. Taking into consideration the interaction of local particle dipole interactions, the Jaysundere–Smith equation is described as follows:[211]

$$k_c = \frac{k_m\phi_m + k_f\phi_f \frac{3k_m}{(2k_m + k_f)}\left[1 + 3\phi_f \frac{k_f - k_m}{2k_m + k_f}\right]}{\phi_m + \phi_f \frac{3k_m}{(2k_m + k_f)}\left[1 + 3\phi_f \frac{k_f - k_m}{2k_m + k_f}\right]} \tag{6}$$

5.2. Common strategies for preparing $BaTiO_3$–polymer nanocomposites and their dielectric properties

As the size of electrical devices becomes increasingly smaller, it still necessitates the incorporation of many different components including resistors, capacitors and inductors which are quite large and take up a large area on device substrates. To break this size reduction dilemma while still improving the device performance, much efforts have been made to develop high dielectric constant materials and utilize them in the form of thin films or directly use nanostructured materials to shrink the device size.[215] Because of its high dielectric constant (over a range of 50–6000),[90] $BaTiO_3$ becomes one of the most popular candidate materials for capacitor applications, especially for nanostructured $BaTiO_3$ as their utilization in capacitors can shrink device size while still maintaining a high energy storage capability.[88,216] As the device size reduction demands more from key materials, $BaTiO_3$–polymer nanocomposites have received more attention than pure $BaTiO_3$. This is because the $BaTiO_3$–polymer nanocomposites combine the advantages from each constituent, such as easy processibility and higher breakdown strength from polymer matrices and high dielectric constant from $BaTiO_3$ fillers. As a result of the synergy effect in the nanocomposites, a significant increase in the energy storage density can be achieved.[217]

The choice for polymer matrices is quite broad. However, there are several principles to follow when selecting polymer component, such as high breakdown strength, high dielectric constant, low cost, environmentally friendly, to name a few. In this regard, poly(vinylidenedifluoride) (PVDF) stands out as the most commonly used one, owing to its high breakdown strength of 590 kV mm^{-1} and high dielectric constant of 8.4@1 MHz (a high value among polymers).[106,217] Realizing a high dielectric constant, high breakdown field strength, and low dielectric loss at the same time is not trivial in $BaTiO_3$–polymer composites.

Therefore the best approach is a compromise of these three desired properties by adjusting the volume ratio of each component, the size and shape of the $BaTiO_3$ particles, the crystalline phase of each component, the material interfaces, and the uniformity of the nanocomposites.[210,216] Traditionally, $BaTiO_3$–polymer composite films are prepared *via* physical mixing of a dielectric polymer solution with submicron or micron-sized ferroelectric particles followed by solvent evaporation.[218] This simple, direct mixing method often results in significant aggregation of filler particles due to no compatibilization between the filler and the polymer matrix. This leads to problems in the resulting devices including higher dielectric losses and reduced breakdown strengths as a result of aggregation-induced local depolarization caused by filler exclusion from the matrix.[219]

In order to achieve high dispersion and increased loading of $BaTiO_3$ nanocrystals in polymer matrices, surface functionalization of nanocrystals with surface modifiers (small molecules and polymers) has been investigated.[220] As a result, well-controlled nanocrystal/polymer interfaces can be realized leading to improved dispersions of nanocrystals within polymer matrices. New structures with ultra-small $BaTiO_3$ nanocrystals carried by various inorganic nanostructures have also been developed, for the purpose of further enhancing the dielectric performance of the nanocomposites.[221–223] In addition, polydopamine has been widely utilized as a coating layer onto the nanofiller in order to improve the compability and homogeneity of the nanofiller within the matrix.[224,225] It is generally believed that an ideal and controlled $BaTiO_3$ nanocrystal/polymer interface is required to achieve high permittivity and large dielectric constants while also minimizing the leakage current and improving the energy density. Ideal interfaces should possess a tough insulating layer that prevents direct contact between the dielectric materials of neighboring particles as well as proper surface modification of the particle surfaces to enable their dispersion in a polymer matrix.[226] It has been demonstrated that a tailored interface formed by surface-grafted polymers can significantly reduce dielectric loss because the grafted polymer layer can hinder interfacial transport and effectively restrict particle–particle hot spots.[227]

In this section, we will discuss recent progress in the design and characterization of $BaTiO_3$–polymer nanocomposites that satisfy the above standards with a focus on ''grafting-to'' and ''grafting-from'' strategies. In ''grafting-to'' strategies, the polymer chains are first polymerized by various methods and then attached to the surface of various nanocrystals.[106] In ''grafting-from'' strategies, polymer chains are grown from the surface of nanocrystals functionalized in such a way to initiate polymerization (commonly some form of controlled radical polymerization).[228,229] For each strategy, several representative examples are discussed to summarize the common synthetic routes to nanocomposites and their improved dielectric performance.

5.2.1. ''Grafting-to'' methods. In the ''grafting-to'' method, a polymer is tethered to the surface of a nanocrystal *via* a physical or chemical interaction. This surface modification can increase the dispersion of $BaTiO_3$ NCs in a polymer matrix. Marder, Perry *et al.* performed a systematic investigation of the binding affinity of a variety of functional groups to the surface of $BaTiO_3$ nanoparticles and the compatibilization of the surface-modified $BaTiO_3$ nanoparticles with polymer hosts such as polycarbonate (PC) and poly(vinylidenedifluoride-*co*-hexafluoropropylene) (P(VDF–HFP)).[106] Their results indicated that ligands bearing phosphonic acid functional groups can form a strong, and stable organic shell on $BaTiO_3$ nanoparticles that can improve their dispersion in various polymer matrices. The nanocomposites formed from phosphonic acid-modified $BaTiO_3$ nanoparticles and polymers exhibited high energy-storage capacities as well as high dielectric permittivities and improved dielectric constants. Specifically, (2-[2-(2-methoxyethoxy)ethoxy]-ethyl)phosphonic acid (PEGPA) was coated on $BaTiO_3$ nanoparticles to enable their dispersion in a polycarbonate (PC) matrix. Since PEGPA has a tail composed of ether linkages and an alcohol, it can improve the dispersion of $BaTiO_3$ nanoparticles in polar hydrophilic solutions (Fig. 37a, left). Similarly, pentafluorobenzyl phosphonic acid (PFBPA) was also investigated as it possesses a fluorinated benzyl group that provides improved dispersion in fluorinated elastomers and organic solvents (Fig. 37a, right). Such chemical functionalization of $BaTiO_3$ reduced nanoparticle aggregation. This was supported by the significant reduction in nanoparticle aggregate size which ultimately led to more uniform films with homogeneous nanoparticle dispersions. The frequency-dependent capacitance and loss tangent measurements

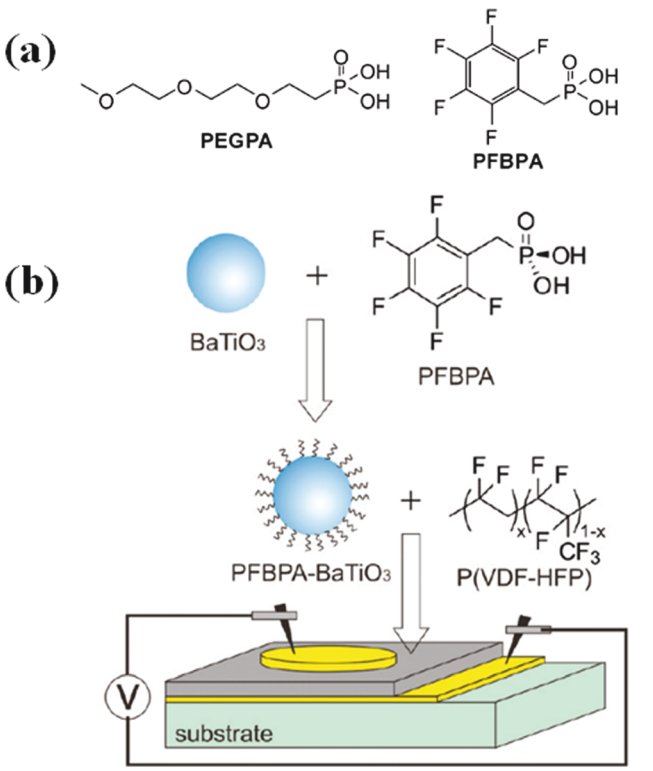

Fig. 37 (a) Molecular structure of (2-[2-(2-methoxyethoxy)ethoxy]ethyl)-phosphonic acid (PEGPA) and pentafluorobenzyl phosphonic acid (PFBPA) surface ligands; (b) schematic illustration of the nanocomposite fabrication process and the layout of the nanocomposite thin film capacitors. Reproduced with permission.[106] Copyright 2007, Wiley.

indicated that the nanocomposites retained a high dielectric constant (ε_r = 37 ± 2 at 1 kHz for 50 vol% PFBPA–$BaTiO_3$ in P(VDF–HFP)) and a large dielectric strength (210 ± 50 kV mm^{-1}) suggesting these materials have a high energy-storage capacity.[106]

In the above work, it was found that the volume fraction of $BaTiO_3$ nanoparticles (the high permittivity component) must be increased beyond 30% in order to increase the nanocomposite permittivity. However, the tradeoff with increasing the $BaTiO_3$ content is that it reduces the dielectric strength of the nanocomposite. Therefore, the $BaTiO_3$ volume fraction in a nanocomposite needs to be optimized to realize the best performance and energy storage density.[230] In this study, phosphonic acid-modified $BaTiO_3$ and poly(vinylidene fluoride-*co*-hexafluoropropylene) (P(VDF–HFP)) were used to investigate the role of high permittivity $BaTiO_3$ nanoparticles on the various dielectric properties of the formed nanocomposites including dielectric loss, permittivity, and breakdown strength (Fig. 37b).[230] The results showed that at lower $BaTiO_3$ volume fractions, measured effective permittivity of the nanocomposites matched well with self-consistent effective medium field (SC-EMT) modeling calculations with a peak relative permittivity of 35. Interestingly, when the volume fraction is greater than 50%, a reduction in the effective permittivity was observed with increasing particle loading. This behavior was found to relate heavily to the porosity of the resulting films. Similarly, the breakdown strength of the films decreased rapidly with 10% $BaTiO_3$ loading and subsequently reduced more with additional nanoparticle loading. These results, in conjunction with model calculations, suggest that the nanoparticle connectivity and path structure within the nanocomposites, as well as the porosity, greatly influence their properties.[230]

As previously discussed, dispersants (*i.e.*, surfactants and capping ligands) can be used to better incorporate fillers ($BaTiO_3$ NCs) into polymer matrices by improving their dispersion. However, most dispersants reported to date react only with the surface of the fillers and are unresponsive to the presence of the polymer matrix (*i.e.* minimal favorable interaction and/or chemical reactivity). Recently, a silane coupling agent was reported to act as a bridge between the fillers and the polymer matrix thus enabling improved compatibility between the two components.[219] The $BaTiO_3$ nanoparticles are functionalized with the coupling agent, γ-aminopropyltriethoxy silane (KH550), in ethanol solution (Fig. 38a). Next they were dispersed in *N*,*N*-dimethylformamide (DMF) which contains the polymer matrix material, *i.e.*, polyvinylidene fluoride (PVDF). The mixture is subsequently formed into nanocomposite films with good dispersion and uniformity, due to the good bonding effect of KH550. In addition, an optimized coupling agent content (~1.0 wt%) was found to increase the compatibility bringing the dielectric loss of the composite below 10^5 Hz, as shown in Fig. 38b and c, the dielectric loss of the nanocomposites is less than 0.05 below 10^5 Hz, making such nanocomposites applicable as a dielectric in capacitors.[219]

In addition to surface modification and physical mixing, a photopolymerization technique has also proven effective in making ceramic/polymer nanocomposites with improved dispersion and uniformity.[231] In a typical experiment, $BaTiO_3$ fillers are added into liquid monomers to form suspensions which are then subjected to UV radiation at ambient temperatures. The photocurable monomers form highly cross-linked polymer networks with integrated particles once photocured. This photopolymerization method has several advantages. First, liquid monomers can readily penetrate into and around the $BaTiO_3$ particles to ensure a highly integrated suspension and subsequent cured matrix. Second, there are a large variety of monomers that can be photocured thus enabling excellent control over the mechanical properties of the composites. The mechanical properties of such materials are typically essential for their practical incorporation into more complex devices.[231] This work used

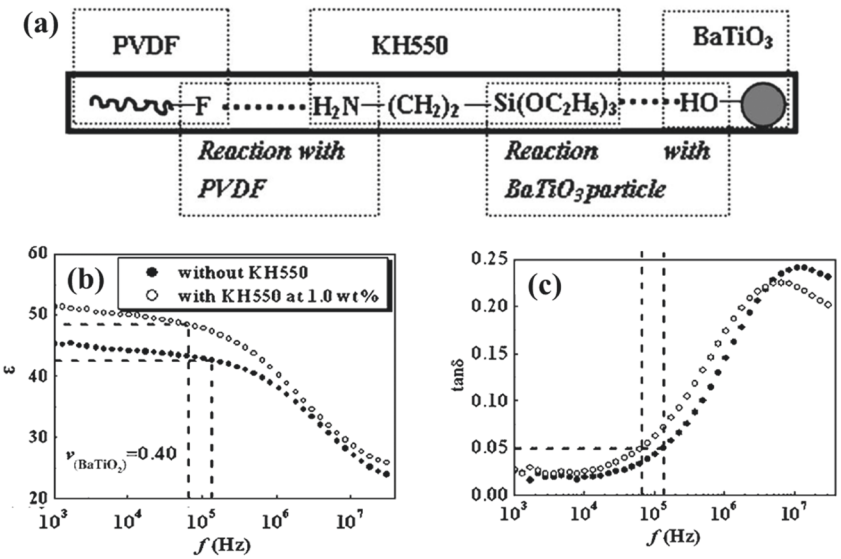

Fig. 38 (a) Schematic illustration of the reaction process between KH550 and both the $BaTiO_3$ nanocrystal surfaces and PVDF matrix. Dependence of (b) the dielectric constant and (c) the loss tangent in the $BaTiO_3$/PVDF composites at 40.0 vol% $BaTiO_3$ on frequency at room temperature. Reproduced with permission.[219] Copyright 2006, American Institute of Physics.

three different photocurable monomers possessing different polarities for use as polymer matrices. These monomers include trimethylolpropane triacrylate (TMPTA), poly(ethylene glycol)-diacrylate (PEGDA), and 1,14-tetradecanediol dimethacrylate (TDDMA). The results showed that polar polymers not only increase the dielectric constant of the composites at low frequencies but also increase the dielectric loss. Moreover, the thermal dependence of the dielectric constant is also heavily dependent on both the polymer polarity and their mobility at low frequencies.

Besides traditional solution-based processes for nanocomposite fabrication, electron beam vapor deposition has also been reported.[232] This approach has the advantage of requiring no solvents and offers rapid fabrication times. The composites are formed on Al-coated Si substrates under high-vacuum using a co-deposition system to produce $BaTiO_3$ nanoparticles dispersed within high dielectric constant polyaniline–polyurethane (PANI–PU) copolymer networks. Capacitor performance (frequency-independent capacitance density $\sim$ 10 nF cm^{-2}, loss tangent = 0.1, at 200 MHz) of the as-deposited and annealed nanocomposites was found to be promising for applications in radio frequency (RF) technologies.

In addition to $BaTiO_3$/polymer binary systems, ternary nanocomposites containing two inorganic materials ($BaTiO_3$ and SiO_2) coated with polymers (*e.g.* polyimide (PI)) have also been reported.[233] Silica-coated $BaTiO_3$ was prepared by a sol–gel method to improve the stability of $BaTiO_3$ nanoparticles as well as enable coupling *via* a difunctional amino-silane molecule. The polymer was coated on the surface of $BaTiO_3$–SiO_2 by a dispersion polymerization method where 3-aminopropyltriethoxysilane (APTES) was added as a coupling agent to provide a connection between the inorganic domains and the polymer matrix. FTIR analysis supported the covalent connection between the silica-coated $BaTiO_3$ and the polyimide matrix. As a result of the coupling between the polyimide matrix and the silica-coated $BaTiO_3$, the nanocomposites showed an enhanced thermal stability when compared to simpler binary systems.

In addition to silica, titanate NDZ101 has also been used to modify $BaTiO_3$ nanoparticles to establish cross-linking between $BaTiO_3$ nanoparticles and polymers.[234] NDZ101 is one kind of coupling agent possessing both alkoxy and alkyl chains. In this study, the alkoxy chains are believed to react with surface hydroxyl groups on $BaTiO_3$. Simultaneously, the long alky chains of the cross-linker entangle with the polymer component. It was found that the titanate-coated $BaTiO_3$ nanoparticles dispersed well in polyvinylidene difluoride matrices. It was further verified by FT-IR that coupling occurred at both the particle–titanate interface and the titanate–polymer interface. The coated $BaTiO_3$/PVDF nanocomposites showed improved dielectric performance with increased breakdown strengths as high as 250 kV mm^{-1}, peak energy densities of 4 J cm^{-1}.[234] It is clear that titanate plays a role in improving the connectivity between the inorganic and organic components of the nanocomposite.

5.2.2. "Grafting-from" methods. In the previous section, surfactant polymers/oligomers or small molecules formed the organic layer on the surface of inorganic particles *via* charged or polar interactions to facilitate the dispersion of $BaTiO_3$ in various polymer matrices. However, the adsorption/desorption equilibrium of the organic molecules at the inorganic surface usually prevents the formation of a robust and permanent polymer shell and leads to increased current leakage and lowered breakdown voltage when the ratio of inorganic particles in the polymer matrix is high as well as gradually over time.[226] The stability of such approaches is also generally limited as the particles gradually aggregate over time. One way to alleviate this problem is to perform *in situ* polymerizations which afford simple, low-cost and more stable means of dispersing particles within polymer matrices.[229] To further improve the inorganic–organic interfacial stability, core@shell-structured nanoparticles dispersed in polymer nanocomposites have been widely investigated using different grafting-from polymerization techniques.[220]

Recently, a novel strategy known as surface-initiated reversible addition–fragmentation chain transfer polymerization (SI-RAFT) was used to improve the interface between the ferroelectric polymer poly(vinylidenedifluoride-*co*-hexafluoro propylene) (P(VDF–HFP)) and $BaTiO_3$ nanoparticles.[228] In this work, the surface of $BaTiO_3$ was functionalized with a fluoropolymer called 1*H*,1*H*,2*H*,2*H*-heptadecafluorodecyl acrylate (PHFDA) to form a core–shell $BaTiO_3$–PHFDA nanocomposite (Fig. 39). Subsequently, the core@shell nanoparticles were mixed with the ferroelectric polymer P(VDF–HFP) to achieve a high dielectric permittivity nanocomposite. Owing to the favorable interaction between the PHFDA surface polymers and the P(VDF–HFP) polymer matrix (*i.e.* both fluoropolymers), the $BaTiO_3$ nanoparticles exhibited good dispersion and high quality interfaces with the polymer matrix. Using this approach, both high energy densities and low dielectric losses were observed. In the case of 50% volume fraction of $BaTiO_3$–PTFEA, the breakdown strength of the nanocomposites was found to be 182 kV mm^{-1} with a maximum energy density of 6.23 J cm^{-3} (a 50% increase relative to pure P(VDF–HFP)). The breakdown strength does decrease with increased particle loading. However, the decrease levels off at around 182 kV mm^{-1} whereas the maximum energy density continues to rise. The advantage of this SI-RAFT technique is that it makes tuning the shell thickness and grafting density very simple as all this requires is longer reaction times and

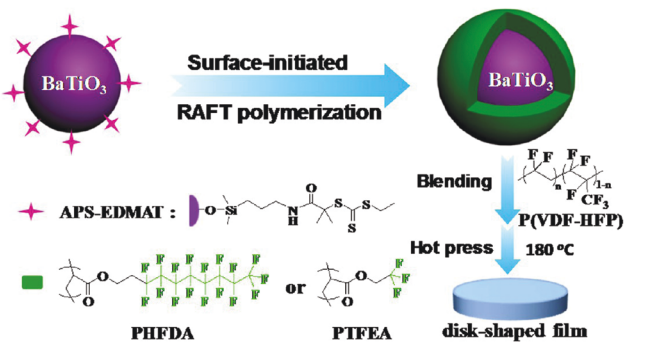

Fig. 39 Schematic illustration of the preparation of fluoropolymer@$BaTiO_3$ core–shell nanoparticles *via* SI-RAFT and P(VDF–HFP) nanocomposite films *via* hot pressing of suspensions. Produced with permission.[228] Copyright 2013, American Chemical Society.

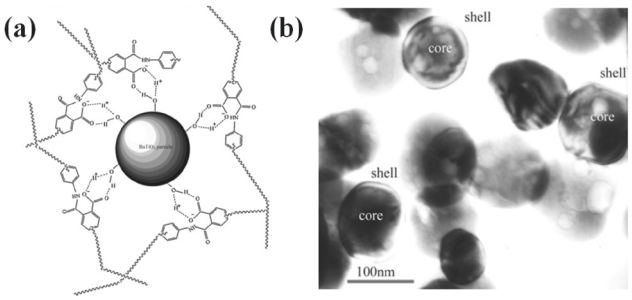

Fig. 40 (a) Proposed mechanism of poly(amic acid) (PAmA) adsorption onto $BaTiO_3$ particles; (b) TEM image of a $BaTiO_3$/polyimide (PI) composite film cross-section obtained by *in situ* polymerization. Reproduced with permission.[235] Copyright 2008, Wiley.

higher ratios of polymer surface initiator. Consequently, this allows performance properties to be easily adjusted.[228]

Marks *et al.* reported an *in situ* polymerization technique to synthesize $BaTiO_3$/polypropylene nanocomposites.[229] To build a perfect interfacial region between $BaTiO_3$ nanoparticles and the polymer matrix, a shell of Al_2O_3 was first coated on the surface of the $BaTiO_3$ nanoparticles to accommodate the large permittivity contrast between the $BaTiO_3$ nanoparticles ($\varepsilon_r \sim 50$–6000) and the polypropylene ($\varepsilon_r \sim 2.25$). Next, a metallocene catalyst ([*rac*-ethylenebisindenyl]zirconium dichloride ($EBIZrCl_2$)) was adhered to the Al_2O_3-coated $BaTiO_3$ nanoparticles and in the process activated. *In situ* polymerization of isotactic polypropylene from the nanoparticle surfaces effectively prevented aggregation to yield well-dispersed nanoparticles in the nanocomposite. The nanocomposites showed leakage currents on the order of 10^{-7} to 10^{-9} A cm^{-2} at a field strength of 10 kV mm^{-1}. They also showed low dielectric losses over the 100 Hz to 1 MHz frequency range. These performance properties, coupled with the inexpensive materials makes propylene-grafted Al_2O_3-coated $BaTiO_3$ nanocomposites highly attractive for energy storage devices.

Due to its high thermal and chemical stability, ease of film casting, high mechanical strength and high electrical breakdown strength, polyimide (PI) has been widely investigated as a dielectric material. The synthesis of $BaTiO_3$–PI nanocomposites has drawn considerable attention in recent years. In contrast to conventional mixing techniques, such as melt mixing and solution mixing, $BaTiO_3$–PI nanocomposites are prepared by the *in situ* polymerization of poly(amic acid) (PAmA) followed by the *in situ* imidization of PAmA to yield $BaTiO_3$–PI with improved performance.[235] More specifically, this approach can be broken down into four steps. First, the $BaTiO_3$ nanoparticles are dispersed in a solvent to form a suspension. Second, PAmA is formed by polymerization in the suspension. At this time, PAmA is adsorbed onto the $BaTiO_3$ nanoparticle surfaces forming core@shell structures that do not aggregate within the PI matrix (Fig. 40a and b). Third, films are cast on clear glass plates. Lastly, the PAmA is converted to PI by thermal imidization. The solvent is also driven off at this step to yield the final PI matrix containing well-dispersed $BaTiO_3$. Results show a fairly high breakdown strength for the composites (67 kV mm^{-1}). This is likely a result of the formation of the core@shell-like structure which supports the homogeneous dispersion of $BaTiO_3$ particles in the matrix as well as minimized the presence of voids in the nanocomposite. Table 2 summarizes the examples listed above.

6. General observations and future outlook

The controlled synthesis and characterization of $BaTiO_3$ at low dimensions, including $BaTiO_3$-containing composites, has had a profound influence on the current trend toward the greater miniaturization of $BaTiO_3$-based electronic devices. This review summarizes the most recent progress in three key aspects of $BaTiO_3$ nanomaterials. First, chemical synthesis methods for producing high-quality $BaTiO_3$ nanocrystals are presented. Second, the dielectric and ferroelectric properties of $BaTiO_3$ nanocrystal clusters and individual $BaTiO_3$ nanocrystals are investigated using both theoretical modeling and piezoresponse force microscopy (PFM). Lastly, viable $BaTiO_3$ surface functionalization

Table 2 Summary of $BaTiO_3$–polymer nanocomposites: preparation method and their dielectric properties

$BaTiO_3$	Polymer matrix	Method	Dielectric constant	Breakdown strength	Ref.
PFBPA–$BaTiO_3$ nanoparticle, 30–50 nm	P(VDF–HFP)	*Grafting-to*	$\varepsilon_r = 37 \pm 2$ at 1 kHz (50% filler)	210 ± 50 kV mm^{-1}	106
$BaTiO_3$ nanoparticles	PVDF	*Grafting-to*: a silane coupling agent act as a bridge between the filler and the polymer matrix	$\varepsilon_r = 50$ at 100 kHz (40% filler), loss tangent <0.05 below 100 kHz	—	219
$BaTiO_3$ particles	TEGDA TMPTA TDDMA	*Grafting-to*: photopolymerization	Dielectric losses of the composites increases in the order of TDDMA < TMPTA < PEGDA	—	231
Silica-coated $BaTiO_3$ nanoparticles, 30–40 nm	Polyimide	*Grafting-to*: dispersion polymerization method	—	—	233
Titanate-coated $BaTiO_3$ nanoparticles	PVDF	*Grafting-to*:	$\varepsilon_r = 30$ at 1 kHz (22% filler)	250 kV mm^{-1}	234
$BaTiO_3$ nanoparticles	P(VDF–HFP)	*Grafting-from*: SI-RAFT	$\varepsilon_r = 45$ at 1 kHz (50% filler)	182 kV mm^{-1}	228
Al_2O_3-coated $BaTiO_3$ nanoparticles, Al_2O_3 coating ~10 nm	Polypropylene	*Grafting-from*: *in situ* polymerization	$\varepsilon_r = 18$ at 1 kHz (40% filler)	10 kV mm^{-1}	229
$BaTiO_3$ nanoparticles	Polyimide	*Grafting-from*: *in situ* polymerization	$\varepsilon_r = 20$ at 10^3–10^6 Hz (40% filler)	67 kV mm^{-1}	235

strategies for realizing $BaTiO_3$/polymer nanocomposites with high energy storage densities are presented.

Despite the significant progress made so far in the controlled synthesis of $BaTiO_3$ nanocrystals with well-defined morphologies (*e.g.*, nanodots, nanorods, nanocubes and nanowires) and crystal structures (*e.g.*, cubic, tetragonal), they are still of lower quality in comparison to other well-established nanomaterials such as metals and semiconductors. For example, one-dimensional $BaTiO_3$ nanostructures (*e.g.*, nanowires and nanorods) still have large size distributions and poorly controlled morphologies (Section 3). As discussed previously, these one-dimensional structures are more promising building blocks for realizing nanoscale electronic,[87] optical,[236] and mechanical[237] devices as they retain wire-like connectivity and efficiently transfer the stress, charge and heat throughout the system. It is clearly challenging to realize one-dimensional $BaTiO_3$ nanostructures. However, certain crystal growth mechanisms, such as orientated attachment,[238–240] and catalyst-assisted growth,[241,242] are promising for producing high-quality one-dimensional nanostructures. This has yet to be explored. Moreover, other interesting anisotropic nanostructures are of great scientific and technological interest including tetrapods[243,244] and hyperbranched nanocrystals.[245] These have also not yet been reported. With continued progress in soft chemical techniques, more high quality one dimensional nanostructures may be produced.

Another important area requiring extensive research is the tailoring of the crystal structure of $BaTiO_3$ to push its critical size to even smaller values. The critical size of $BaTiO_3$ currently reported is 50 nm, below which $BaTiO_3$ nanocrystals are in the cubic phase that lacks ferroelectric properties. The size effect thus limits the utilization of $BaTiO_3$ in high-density energy/information storage. Based on the core–shell model (Section 2),[75,76] the surface chemistry and structure can also influence the ferroelectric behavior of the nanocrystals.[57] Thus, it is feasible to convert the cubic structure into the tetragonal phase at low dimensions through surface engineering such as ligand modification and second phase coating. Various techniques, including ligand modification,[104] metal coating,[107] and template confinement,[57] have proven effective for suppressing the presence of the cubic phase. However, these strategies are still far from seeing use in practical applications and a clear understanding of the basic mechanisms remains unclear. With progress in characterization techniques, especially those capable of probing the local structure and properties such as scanning probe techniques,[246–248] near-field Raman spectra,[249–252] and atomic probe microscopy,[253,254] it is likely that a systematic understanding of the effects of surface modification on ultimate crystal structure and dielectric properties can be realized. This in turn will provide the guidance to develop new strategies for improving device performance by preserving the ferroelectric properties at smaller sizes (5–15 nm based on theoretical predictions).[255]

In addition, current work on $BaTiO_3$–polymer nanocomposite systems mainly uses strongly binding modifiers to improve the dispersion of $BaTiO_3$ nanocrystals within polymer matrices. While there are limited works reporting on directly grafting high molecular weight polymers onto the $BaTiO_3$ surface, it is the most efficient approach to date to obtain dispersions of nanocrystals in polymer matrices. With advances in polymeric grafting techniques, we anticipate rapidly evolving research in this field. Various types of interesting dielectric polymers, such as PVDF and PI, can be directly grafted onto the $BaTiO_3$ surface. Different kinds of grafting chemistry will also be developed to enable strong chemical bonding for improved performance (*i.e.*, reduced leakage current and higher breakdown voltage). Additionally, the interaction between polymers and $BaTiO_3$ nanocrystals in nanocomposites is usually weak, particularly in the solution state. Owing largely to the adsorption–desorption dynamics of surface grafting,[256] large-scale phase separation can occur after long-time storage or with various post treatments. One way to address these concerns is the template approach. This technique employs amphiphilic block copolymers to guide the growth of nanocrystals. We envision that microphase-separated structures and/or micelles of amphiphilic diblock copolymers composed of a hydrophilic block and hydrophobic dielectric block (*e.g.*, poly(acrylic acid)-*b*-polyvinylidene fluoride (PAA-*b*-PVDF)) may be exploited as templates to synthesize nanocrystals that are intimately and permanently connected with dielectric polymers due to the strong affinity of inorganic precursors to the hydrophilic block (*e.g.*, PAA).[50] Importantly, since the two blocks in the amphiphilic block copolymer templates are covalently linked, the resulting nanocomposites[50] are expected to be much more stable than those prepared by direct grafting strategies that rely on the coordination interaction between nanocrystals and ligand functional groups.

Conflicts of interest

There are no conflicts to declare.

Acknowledgements

We gratefully acknowledge the support from the National Science Foundation (NSF CMMI 1562075 and DMR 1709420) and the Airforce Office of Scientific Research (AFOSR; FA9550-16-1-0187).

References

1 D. N. Donahoe, M. Pecht, I. K. Lloyd and S. Ganesan, *Microelectron. Reliab.*, 2006, **46**, 400–408.
2 Y. Sakabe, Y. Takeshima and K. Tanaka, *J. Electroceram.*, 1999, **3**, 115–121.
3 F. Azough, R. Al-Saffar and R. Freer, *J. Eur. Ceram. Soc.*, 1998, **18**, 751–758.
4 H. J. McSkimin, *J. Acoust. Soc. Am.*, 1959, **31**, 1519–1522.
5 H. U. Kim, W. H. Lee, H. V. R. Dias and S. Priya, *IEEE Trans. Ultrason. Eng.*, 2009, **56**, 1555–1568.
6 G. H. Haertling, *J. Am. Ceram. Soc.*, 1999, **82**, 797–818.
7 T. F. Hueter and E. Dozois, *J. Am. Ceram. Soc.*, 1952, **24**, 85–86.
8 R. J. Meyer, R. E. Newnham, A. Amin and B. M. Kulwicki, *J. Am. Ceram. Soc.*, 2003, **86**, 934–938.

9 A. C. Dent, C. R. Bowen, R. Stevens, M. G. Cain and M. Stewart, *J. Eur. Ceram. Soc.*, 2007, **27**, 3739–3743.
10 C. M. Landis and R. M. McMeeking, *Ferroelectrics*, 2001, **255**, 13–34.
11 J. Liu, Z. J. Shen, W. L. Yao, Y. H. Zhao and A. K. Mukherjee, *Nanotechnology*, 2010, **21**, 075706.
12 P. T. Lin, Z. Liu and B. W. Wessels, *J. Opt. A: Pure Appl. Opt.*, 2009, **11**, 075005.
13 J. M. Marx, O. Eknoyan, H. F. Taylor, Z. Tang and R. R. Neurgaonkar, *Appl. Phys. Lett.*, 1995, **67**, 1381–1383.
14 T. Takenaka, H. Nagata, Y. Hiruma, Y. Yoshii and K. Matumoto, *J. Electroceram.*, 2007, **19**, 259–265.
15 D. Liu and J. Y. Li, *Appl. Phys. Lett.*, 2003, **83**, 1193–1195.
16 R. Maranganti and P. Sharma, *Phys. Rev. B: Condens. Matter Mater. Phys.*, 2009, **80**, 054109.
17 J. L. Ruglovsky, J. Y. Li, K. Bhattacharya and H. A. Atwater, *Acta Mater.*, 2006, **54**, 3657–3663.
18 H. Z. Jin and J. Zhu, *J. Appl. Phys.*, 2002, **92**, 4594–4598.
19 S. Ezhilvalavan and T. Y. Tseng, *Mater. Chem. Phys.*, 2000, **65**, 227–248.
20 M. H. Yeh, Y. C. Liu, K. S. Liu, I. N. Lin, J. Y. M. Lee and H. F. Cheng, *J. Appl. Phys.*, 1993, **74**, 2143–2145.
21 D. E. Kotecki, J. D. Baniecki, H. Shen, R. B. Laibowitz, K. L. Saenger, J. J. Lian, T. M. Shaw, S. D. Athavale, C. Cabral, P. R. Duncombe, M. Gutsche, G. Kunkel, Y. J. Park, Y. Y. Wang and R. Wise, *IBM J. Res. Dev.*, 1999, **43**, 367–382.
22 A. Rasul, J. Zhang, D. Gamota, M. Singh and C. Takoudis, *Solid State Ionics*, 2010, **518**, 7024–7028.
23 Y. Jang, W. H. Lee, Y. D. Park, D. Kwak, J. H. Cho and K. Cho, *Appl. Phys. Lett.*, 2009, **94**, 183301.
24 Q. J. Cai, Y. Gan, M. B. Chan-Park, H. B. Yang, Z. S. Lu, C. M. Li, J. Guo and Z. L. Dong, *Chem. Mater.*, 2009, **21**, 3153–3161.
25 I. Salaoru and S. Paul, *J. Optoelectron. Adv. Mater.*, 2008, **10**, 3461–3464.
26 V. N. Shut, S. V. Kostomarov and A. V. Gavrilov, *Inorg. Chem.*, 2008, **44**, 905–910.
27 W. Preis and W. Sitte, *Solid State Ionics*, 2006, **177**, 3093–3098.
28 G. Ahmad, M. B. Dickerson, Y. Cai, S. E. Jones, E. M. Ernst, J. P. Vernon, M. S. Haluska, Y. Fang, J. Wang, G. Subrarnanyarn, R. R. Naik and K. H. Sandhage, *J. Am. Ceram. Soc.*, 2008, **130**, 4–5.
29 D. S. Smith, N. Ghayoub, I. Charissou, O. Bellon, P. Abelard and A. H. Edwards, *J. Am. Ceram. Soc.*, 1998, **81**, 1789–1796.
30 G. H. Kwei, A. C. Lawson, S. J. L. Billinge and S. W. Cheong, *J. Phys. Chem.*, 1993, **97**, 2368–2377.
31 W. P. Mason and B. T. Matthias, *Phys. Rev.*, 1948, **74**, 1622–1636.
32 J. C. Slater, *Phys. Rev.*, 1950, **78**, 748–761.
33 H. Takahasi, *J. Phys. Soc. Jpn.*, 1961, **16**, 1685–1689.
34 J. F. Scott, *Ferroelectrics*, 2005, **316**, 13–21.
35 W. Borland and J. J. Felten, *2001 Proceedings of International Symposium on Microelectronics*, 2001, vol. 4587, pp. 452–457.
36 V. K. Varadan, V. V. Varadan and K. A. Jose, *Electronics and Structures for Mems*, 1999, vol. 3891, pp. 266–275.
37 K. Akamatsu, T. Tsuruoka and H. Nawafune, *J. Am. Chem. Soc.*, 2005, **127**, 1634–1635.
38 X. G. Peng, L. Manna, W. D. Yang, J. Wickham, E. Scher, A. Kadavanich and A. P. Alivisatos, *Nature*, 2000, **404**, 59–61.
39 C. B. Murray, D. J. Norris and M. G. Bawendi, *J. Am. Chem. Soc.*, 1993, **115**, 8706–8715.
40 Y. Yin and A. P. Alivisatos, *Nature*, 2005, **437**, 664–670.
41 S. H. Sun, C. B. Murray, D. Weller, L. Folks and A. Moser, *Science*, 2000, **287**, 1989–1992.
42 Q. Song and Z. J. Zhang, *J. Am. Chem. Soc.*, 2004, **126**, 6164–6168.
43 Y. W. Jun, Y. M. Huh, J. S. Choi, J. H. Lee, H. T. Song, S. Kim, S. Yoon, K. S. Kim, J. S. Shin, J. S. Suh and J. Cheon, *J. Am. Chem. Soc.*, 2005, **127**, 5732–5733.
44 M. H. Frey and D. A. Payne, *Phys. Rev. B: Condens. Matter Mater. Phys.*, 1996, **54**, 3158–3168.
45 T. M. Shaw, S. Trolier-McKinstry and P. C. McIntyre, *Annu. Rev. Mater. Sci.*, 2000, **30**, 263–298.
46 Z. Zhao, V. Buscaglia, M. Viviani, M. T. Buscaglia, L. Mitoseriu, A. Testino, M. Nygren, M. Johnsson and P. Nanni, *Phys. Rev. B: Condens. Matter Mater. Phys.*, 2004, **70**, 024107.
47 M. P. McNeal, S. J. Jang and R. E. Newnham, *J. Appl. Phys.*, 1998, **83**, 3288–3297.
48 U. A. Joshi and J. S. Lee, *Small*, 2005, **1**, 1172–1176.
49 S. O'Brien, L. Brus and C. B. Murray, *J. Am. Chem. Soc.*, 2001, **123**, 12085–12086.
50 B. Jiang, X. Pang, B. Li and Z. Lin, *J. Am. Chem. Soc.*, 2015, **137**, 11760–11767.
51 Z. Deng, Y. Dai, W. Chen, X. M. Pei and J. H. Liao, *Nanoscale Res. Lett.*, 2010, **5**, 1217–1221.
52 N. Z. Bao, L. M. Shen, A. Gupta, A. Tatarenko, G. Srinivasan and K. Yanagisawa, *Appl. Phys. Lett.*, 2009, **94**, 253109.
53 S. Adireddy, C. K. Lin, B. B. Cao, W. L. Zhou and G. Caruntu, *Chem. Mater.*, 2010, **22**, 1946–1948.
54 J. J. Urban, W. S. Yun, Q. Gu and H. Park, *J. Am. Chem. Soc.*, 2002, **124**, 1186–1187.
55 Y. B. Mao, S. Banerjee and S. S. Wong, *Chem. Commun.*, 2003, 408–409.
56 H. Nakano and H. Nakamura, *J. Am. Ceram. Soc.*, 2006, **89**, 1455–1457.
57 N. Nuraje, K. Su, A. Haboosheh, J. Samson, E. P. Manning, N. L. Yang and H. Matsui, *Adv. Mater.*, 2006, **18**, 807–811.
58 K. C. Huang, T. C. Huang and W. F. Hsieh, *Inorg. Chem.*, 2009, **48**, 9180–9184.
59 A. F. Demirors and A. Imhof, *Chem. Mater.*, 2009, **21**, 3002–3007.
60 R. L. Brutchey and D. E. Morse, *Angew. Chem., Int. Ed.*, 2006, **45**, 6564–6566.
61 G. A. Schneider, T. Scholz, J. Munoz-Saldana and M. V. Swain, *Appl. Phys. Lett.*, 2005, **86**, 192903.
62 F. Felten, G. A. Schneider, J. M. Saldana and S. V. Kalinin, *J. Appl. Phys.*, 2004, **96**, 563–568.

63 S. V. Kalinin and D. A. Bonnell, *Appl. Phys. Lett.*, 2001, **78**, 1116–1118.
64 J. L. Jones, *J. Electroceram.*, 2007, **19**, 67–79.
65 M. Yashima, T. Hoshina, D. Ishimura, S. Kobayashi, W. Nakamura, T. Tsurumi and S. Wada, *J. Appl. Phys.*, 2005, **98**, 014313.
66 Y. Noda, K. Akiyama, T. Shobu, Y. Kuroiwa, H. Nakao, Y. Morii and H. Yamaguchi, *Ferroelectrics*, 1998, **217**, 1–7.
67 A. Harrison, R. Ibberson, G. Robb, G. Whittaker, C. Wilson and D. Youngson, *Faraday Discuss.*, 2003, **122**, 363–379.
68 C. L. Jia and K. Urban, *Science*, 2004, **303**, 2001–2004.
69 C. L. Jia, S. B. Mi, K. Urban, I. Vrejoiu, M. Alexe and D. Hesse, *Nat. Mater.*, 2008, **7**, 57–61.
70 H. Blank and S. Amelinckx, *Appl. Phys. Lett.*, 1963, **2**, 140–142.
71 A. Schilling, T. B. Adams, R. M. Bowman, J. M. Gregg, G. Catalan and J. F. Scott, *Phys. Rev. B: Condens. Matter Mater. Phys.*, 2006, **74**, 024115.
72 C. Fang, D. X. Zhou and S. P. Gong, *Mod. Phys. Lett. B*, 2010, **24**, 2161–2170.
73 J. Petzelt, *Ferroelectrics*, 2010, **400**, 117–134.
74 Y. Dror, R. D. Levi, S. Baltianski and Y. Tsur, *J. Electrochem. Soc.*, 2006, **153**, F137–F143.
75 T. Hoshina, S. Wada, Y. Kuroiwa and T. Tsurumi, *Appl. Phys. Lett.*, 2008, **93**, 192914.
76 T. Tsurumi, T. Hoshina, H. Takeda, Y. Mizuno and H. Chazono, *IEEE Trans. Ultrason. Eng.*, 2009, **56**, 1513–1522.
77 N. Bao, L. Shen, G. Srinivasan, K. Yanagisawa and A. Gupta, *J. Phys. Chem. C*, 2008, **112**, 8634–8642.
78 R. Buonsanti, V. Grillo, E. Carlino, C. Giannini, T. Kipp, R. Cingolani and P. D. Cozzoli, *J. Am. Chem. Soc.*, 2008, **130**, 11223–11233.
79 K. Žagar, F. Hernandez-Ramirez, J. D. Prades, J. R. Morante, A. Rečnik and M. Čeh, *Nanotechnology*, 2011, **22**, 385501.
80 M. Teresa Buscaglia, C. Harnagea, M. Dapiaggi, V. Buscaglia, A. Pignolet and P. Nanni, *Chem. Mater.*, 2009, **21**, 5058–5065.
81 T. W. Odom, J.-L. Huang, P. Kim and C. M. Lieber, *J. Phys. Chem. B*, 2000, **104**, 2794–2809.
82 M. Bockrath, W. Liang, D. Bozovic, J. H. Hafner, C. M. Lieber, M. Tinkham and H. Park, *Science*, 2001, **291**, 283–285.
83 T. Thurn-Albrecht, J. Schotter, G. A. Kästle, N. Emley, T. Shibauchi, L. Krusin-Elbaum, K. Guarini, C. T. Black, M. T. Tuominen and T. P. Russell, *Science*, 2000, **290**, 2126–2129.
84 J. Hu, T. W. Odom and C. M. Lieber, *Acc. Chem. Res.*, 1999, **32**, 435–445.
85 Y. S. Zhao, H. Fu, A. Peng, Y. Ma, Q. Liao and J. Yao, *Acc. Chem. Res.*, 2010, **43**, 409–418.
86 J. J. Urban, J. E. Spanier, O. Y. Lian, W. S. Yun and H. Park, *Adv. Mater.*, 2003, **15**, 423–426.
87 Y. Cui and C. M. Lieber, *Science*, 2001, **291**, 851–853.
88 D. Damjanovic, *Rep. Prog. Phys.*, 1998, **61**, 1267.
89 J. Hong and D. Fang, *Appl. Phys. Lett.*, 2008, **92**, 012906.
90 Y. Huan, X. Wang, J. Fang and L. Li, *J. Eur. Ceram. Soc.*, 2014, **34**, 1445–1448.
91 D. McCauley, R. E. Newnham and C. A. Randall, *J. Am. Ceram. Soc.*, 1998, **81**, 979–987.
92 Y. Aikawa, Y. Iwazaki and T. Suzuki, *J. Ceram. Soc. Jpn.*, 2010, **118**, 1057–1061.
93 Y. Yang, X. H. Wang, C. K. Sun and L. T. Li, *Nanotechnology*, 2009, **20**, 055709.
94 A. D. Handoko and G. K. L. Goh, *Sci. Adv. Mater.*, 2010, **2**, 16–34.
95 S. Berger, *Trans. Indian Inst. Met.*, 2005, **58**, 1141–1156.
96 S. G. Lu, B. R. Li, C. L. Mak and K. H. Wong, *Int. J. Inorg. Mater.*, 2004, **19**, 1231–1239.
97 J. Kiat, C. Bogicevic, P. Gemeiner, A. Al-Zein, F. Karolak, N. Guiblin, F. Porcher, B. Hehlen, L. Yedra and S. Estradé, *Phys. Rev. B: Condens. Matter Mater. Phys.*, 2013, **87**, 024106.
98 Z. Wang, J. Keith Nelson, H. Hillborg, S. Zhao and L. S. Schadler, *Compos. Sci. Technol.*, 2013, **76**, 29–36.
99 R. R. Mehta, B. D. Silverman and J. T. Jacobs, *J. Appl. Phys.*, 1973, **44**, 3379–3385.
100 G. Zhang, D. Brannum, D. Dong, L. Tang, E. Allahyarov, S. Tang, K. Kodweis, J.-K. Lee and L. Zhu, *Chem. Mater.*, 2016, **28**, 4646–4660.
101 S. V. Kalinin, C. Y. Johnson and D. A. Bonnell, *J. Appl. Phys.*, 2002, **91**, 3816–3823.
102 D. G. Popescu, M. A. Husanu, L. Trupin, L. Hrib, L. Pintilie, A. Barinov, S. Lizzit, P. Lacovig and C. M. Teodorescu, *Phys. Chem. Chem. Phys.*, 2015, **17**, 509–520.
103 Y. Zhang, J. Hong, B. Liu and D. Fang, *Nanotechnology*, 2009, **21**, 015701.
104 C. W. Beier, M. A. Cuevas and R. L. Brutchey, *Langmuir*, 2010, **26**, 5067–5071.
105 J. E. Spanier, A. M. Kolpak, J. J. Urban, I. Grinberg, O. Y. Lian, W. S. Yun, A. M. Rappe and H. Park, *Nano Lett.*, 2006, **6**, 735–739.
106 P. Kim, S. C. Jones, P. J. Hotchkiss, J. N. Haddock, B. Kippelen, S. R. Marder and J. W. Perry, *Adv. Mater.*, 2007, **19**, 1001–1005.
107 M. B. Park and N. H. Cho, *Appl. Surf. Sci.*, 2005, **244**, 418–421.
108 F. D. Morrison, D. C. Sinclair and A. R. West, *J. Appl. Phys.*, 1999, **86**, 6355–6366.
109 H. F. Cheng, T. F. Lin, C. T. Hu and I. N. Lin, *J. Am. Ceram. Soc.*, 1993, **76**, 827–832.
110 M. T. Buscaglia, M. Bassoli and V. Buscaglia, *J. Am. Ceram. Soc.*, 2005, **88**, 2374–2379.
111 U. Manzoor and D. K. Kim, *J. Mater. Sci. Technol.*, 2007, **23**, 655–658.
112 V. V. Bhat, M. V. R. Rao and A. M. Umarji, *Mater. Res. Bull.*, 2003, **38**, 1081–1090.
113 A. Y. Fasasi, F. A. Balogun, M. K. Fasasi, P. O. Ogunleye, C. E. Mokobia and E. P. Inyang, *Sens. Actuators, A*, 2007, **135**, 598–604.
114 Z. Y. Wang, J. Hu and M. F. Yu, *Nanotechnology*, 2007, **18**, 235203.

115 A. Ianculescu, D. Berger, C. Matei, P. Budrugeac, L. Mitoseriu and E. Vasile, *J. Electroceram.*, 2010, **24**, 46–50.
116 S. O. Kang, B. H. Park and Y. I. Kim, *Cryst. Growth Des.*, 2008, **8**, 3180–3186.
117 J. Q. Qi, T. Peng, Y. M. Hu, L. Sun, Y. Wang, W. P. Chen, L. T. Li, C. W. Nan and H. L. W. Chan, *Nanoscale Res. Lett.*, 2011, **6**, 466.
118 T. Ould-Ely, M. Luger, L. Kaplan-Reinig, K. Niesz, M. Doherty and D. E. Morse, *Nat. Protoc.*, 2011, **6**, 97–104.
119 A. Testino, M. T. Buscaglia, V. Buscaglia, M. Viviani, C. Bottino and P. Nanni, *Chem. Mater.*, 2004, **16**, 1536–1543.
120 N. T. K. Thanh, N. Maclean and S. Mahiddine, *Chem. Rev.*, 2014, **114**, 7610–7630.
121 H. Zhan, X. Yang, C. Wang, J. Chen, Y. Wen, C. Liang, H. F. Greer, M. Wu and W. Zhou, *Cryst. Growth Des.*, 2012, **12**, 1247–1253.
122 V. K. LaMer and R. H. Dinegar, *J. Am. Chem. Soc.*, 1950, **72**, 4847–4854.
123 S. Puri, *Phase Transitions*, 2004, **77**, 407–431.
124 W. Ostwald, *Z. Phys. Chem.*, 1900, **34**, 495.
125 A. L. Rogach, D. V. Talapin, E. V. Shevchenko, A. Kornowski, M. Haase and H. Weller, *Adv. Funct. Mater.*, 2002, **12**, 653–664.
126 D. S. Wang, T. Xie, Q. Peng, S. Y. Zhang, J. Chen and Y. D. Li, *Chem. – Eur. J.*, 2008, **14**, 2507–2513.
127 M. Froba and A. Reller, *Prog. Solid State Chem.*, 1999, **27**, 1–27.
128 M. L. Steigerwald and L. E. Brus, *Acc. Chem. Res.*, 1990, **23**, 183–188.
129 C. D. Donega, P. Liljeroth and D. Vanmaekelbergh, *Small*, 2005, **1**, 1152–1162.
130 G. Demazeau, *C. R. Chim.*, 2009, **12**, 933–942.
131 G. Demazeau, A. Largeteau and S. Darracq, *Z. Naturforsch., B: Chem. Sci.*, 2010, **65**, 1007–1014.
132 M. Takesue, H. Hayashi and R. L. Smith, *Prog. Cryst. Growth Charact. Mater.*, 2009, **55**, 98–124.
133 S. J. Chen, X. T. Chen, Z. L. Xue, J. H. Zhou, J. Li, J. M. Hong and X. Z. You, *J. Mater. Chem.*, 2003, **13**, 1132–1135.
134 J. S. Lee and S. C. Choi, *J. Eur. Ceram. Soc.*, 2005, **25**, 3307–3314.
135 A. Cabanas and M. Poliakoff, *J. Mater. Chem.*, 2001, **11**, 1408–1416.
136 J. Libera and Y. Gogotsi, *Carbon*, 2001, **39**, 1307–1318.
137 J. O. Eckert, C. C. Hung-Houston, B. L. Gersten, M. M. Lencka and R. E. Riman, *J. Am. Ceram. Soc.*, 1996, **79**, 2929–2939.
138 Y. Xie, Y. T. Qian, W. Z. Wang, S. Y. Zhang and Y. H. Zhang, *Science*, 1996, **272**, 1926–1927.
139 P. Praserthdam, M. Inoue, O. Mekasuvandumrong, W. Thanakulrangsan and S. Phatanasri, *Inorg. Chem. Commun.*, 2000, **3**, 671–676.
140 S. Chaianansutcharit, O. Mekasuwandumrong and P. Praserthdam, *Cryst. Growth Des.*, 2006, **6**, 40–45.
141 C. H. Song, A. M. Stephan, S. K. Jeong, Y. J. Hwang, A. R. Kim and K. S. Nahm, *J. Electrochem. Soc.*, 2006, **153**, A390–A395.
142 S. Biswas, S. T. Kar and S. Chaudhuri, *Mater. Sci. Eng., B*, 2007, **142**, 69–77.
143 X. Y. Chen, L. M. Huang and Q. Z. Li, *J. Phys. Chem. B*, 1997, **101**, 8460–8467.
144 P. Justin, S. K. Meher and G. R. Rao, *J. Phys. Chem. C*, 2010, **114**, 5203–5210.
145 A. P. Moura, L. S. Cavalcante, J. C. Sczancoski, D. G. Stroppa, E. C. Paris, A. J. Ramirez, J. A. Varela and E. Longo, *Adv. Powder Technol.*, 2010, **21**, 197–202.
146 W. K. Tan, K. A. Razak, K. Ibrahim and Z. Lockman, *J. Alloys Compd.*, 2011, **509**, 820–826.
147 Z. Qin, Q. L. Liao, Y. H. Huang, L. D. Tang, X. H. Zhang and Y. Zhang, *Mater. Chem. Phys.*, 2010, **123**, 811–815.
148 J. A. Wang, M. Hojamberdiev, Y. H. Xua and J. H. Peng, *Mater. Chem. Phys.*, 2011, **125**, 82–86.
149 K. Ozeki, H. Aoki and T. Masuzawa, *Appl. Surf. Sci.*, 2010, **256**, 7027–7031.
150 K. Ding, W. E. Seyfried, N. Pester and E. Seyfried, *Geochim. Cosmochim. Acta*, 2010, **74**, A234.
151 N. Sasirekha, B. Rajesh and Y.-W. Chen, *Ind. Eng. Chem. Res.*, 2008, **47**, 1868–1875.
152 H. Hayashi, T. Noguchi, N. M. Islam, Y. Hakuta, Y. Imai and N. Ueno, *J. Cryst. Growth*, 2010, **312**, 1968–1972.
153 X. Zhu, J. Zhu, S. Zhou, Z. Liu, N. Ming and D. Hesse, *J. Cryst. Growth*, 2005, **283**, 553–562.
154 I. J. Clark, T. Takeuchi, N. Ohtori and D. C. Sinclair, *J. Mater. Chem.*, 1999, **9**, 83–91.
155 S. Wei, Lu, B. I. Lee, Z. Lin Wang and W. D. Samuels, *J. Cryst. Growth*, 2000, **219**, 269–276.
156 J.-M. Han, M.-R. Joung, J.-S. Kim, Y.-S. Lee, S. Nahm, Y.-K. Choi and J.-H. Paik, *J. Am. Ceram. Soc.*, 2014, **97**, 346–349.
157 X. Wang, J. Zhuang, Q. Peng and Y. Li, *Nature*, 2005, **437**, 121–124.
158 Z. Zhou, C. C. Bowland, B. A. Patterson, M. H. Malakooti and H. A. Sodano, *ACS Appl. Mater. Interfaces*, 2016, **8**, 21446–21453.
159 M. Niederberger, G. Garnweitner, N. Pinna and M. Antonietti, *J. Am. Chem. Soc.*, 2004, **126**, 9120–9126.
160 M. Niederberger, N. Pinna, J. Polleux and M. Antonietti, *Angew. Chem., Int. Ed.*, 2004, **43**, 2270–2273.
161 H.-W. Lee, S. Moon, C.-H. Choi and D. K. Kim, *J. Am. Ceram. Soc.*, 2012, **95**, 2429–2434.
162 C. S. Chan, G. De Stasio, S. A. Welch, M. Girasole, B. H. Frazer, M. V. Nesterova, S. Fakra and J. F. Banfield, *Science*, 2004, **303**, 1656–1658.
163 A. E. Henkes and R. E. Schaak, *Inorg. Chem.*, 2008, **47**, 671–677.
164 Y. Y. Liang, M. G. Schwab, L. J. Zhi, E. Mugnaioli, U. Kolb, X. L. Feng and K. Mullen, *J. Am. Chem. Soc.*, 2010, **132**, 15030–15037.
165 F. Zhang and D. Y. Zhao, *Nano Res.*, 2009, **2**, 292–305.
166 A. Stein and R. C. Schroden, *Curr. Opin. Solid State Mater. Sci.*, 2001, **5**, 553–564.
167 D. L. Li, H. S. Zhou and I. Honma, *Nat. Mater.*, 2004, **3**, 65–72.

168 D. H. Wang, H. M. Luo, R. Kou, M. P. Gil, S. G. Xiao, V. O. Golub, Z. Z. Yang, C. J. Brinker and Y. F. Lu, *Angew. Chem., Int. Ed.*, 2004, **43**, 6169–6173.
169 W. Y. Dong, Y. J. Sun, C. W. Lee, W. M. Hua, X. C. Lu, Y. F. Shi, S. C. Zhang, J. M. Chen and D. Y. Zhao, *J. Am. Chem. Soc.*, 2007, **129**, 13894–13904.
170 P. M. Rørvik, T. Grande and M.-A. Einarsrud, *Adv. Mater.*, 2011, **23**, 4007–4034.
171 Y. Luo, I. Szafraniak, N. D. Zakharov, V. Nagarajan, M. Steinhart, R. B. Wehrspohn, J. H. Wendorff, R. Ramesh and M. Alexe, *Appl. Phys. Lett.*, 2003, **83**, 440–442.
172 Y. Y. Chen, B. Y. Yu, J. H. Wang, R. E. Cochran and J. J. Shyue, *Inorg. Chem.*, 2009, **48**, 681–686.
173 S. J. Limmer, S. Seraji, Y. Wu, T. P. Chou, C. Nguyen and G. Z. Cao, *Adv. Funct. Mater.*, 2002, **12**, 59–64.
174 D. Chen, H. Zhang, R. Chen, X. Deng, J. Li, G. Zhang and L. Wang, *Phys. Status Solidi A*, 2012, **209**, 714–717.
175 Y. Yang, W. Xiaohui, S. Changku and L. Longtu, *Nanotechnology*, 2009, **20**, 055709.
176 Z. B. Lei, J. M. Li, Y. G. Zhang and S. M. Lu, *J. Mater. Chem.*, 2000, **10**, 2629–2631.
177 J. P. Vernon, Y. N. Fang, Y. Cai and K. H. Sandhage, *Angew. Chem., Int. Ed.*, 2010, **49**, 7765–7768.
178 N. Nuraje, X. Dang, J. Qi, M. A. Allen, Y. Lei and A. M. Belcher, *Adv. Mater.*, 2012, **24**, 2885–2889.
179 H. Liu, C. Hu and Z. L. Wang, *Nano Lett.*, 2006, **6**, 1535–1540.
180 X. Pang, L. Zhao, W. Han, X. Xin and Z. Lin, *Nat. Nanotechnol.*, 2013, **8**, 426–431.
181 H. Xu, Y. Xu, X. Pang, Y. He, J. Jung, H. Xia and Z. Lin, *Sci. Adv.*, 2015, **1**, e1500025.
182 B. Li, C. Zhang, B. Jiang, W. Han and Z. Lin, *Angew. Chem., Int. Ed.*, 2015, **54**, 4250–4254.
183 B. Li, W. Han, B. Jiang and Z. Lin, *ACS Nano*, 2014, **8**, 2936–2942.
184 B. Jiang, C. Han, B. Li, Y. He and Z. Lin, *ACS Nano*, 2016, **10**, 2728–2735.
185 M. He, X. Pang, X. Liu, B. Jiang, Y. He, H. Snaith and Z. Lin, *Angew. Chem.*, 2016, **55**, 4280.
186 P. Setasuwon and S. Kijamnajsuk, *Smart Mater.*, 2008, **55-57**, 161–164.
187 B. Roy, S. P. Ahrenkiel and P. A. Fuierer, *J. Am. Ceram. Soc.*, 2008, **91**, 2455–2463.
188 Z. W. Song, J. F. Ma, H. Y. Sun, W. Wang, Y. Sun, L. J. Sun, Z. S. Liu and C. Gao, *Ceram. Int.*, 2009, **35**, 2675–2678.
189 Y. B. Mao, S. Banerjee and S. S. Wong, *J. Am. Chem. Soc.*, 2003, **125**, 15718–15719.
190 H. Deng, Y. C. Qiu and S. H. Yang, *J. Mater. Chem.*, 2009, **19**, 976–982.
191 I. U. Arachchige and S. L. Brock, *Acc. Chem. Res.*, 2007, **40**, 801–809.
192 M. Niederberger, *Acc. Chem. Res.*, 2007, **40**, 793–800.
193 S. C. Padmanabhan, S. C. Pillai, J. Colreavy, S. Balakrishnan, D. E. McCormack, T. S. Perova, Y. Gun'ko, S. J. Hinder and J. M. Kelly, *Chem. Mater.*, 2007, **19**, 4474–4481.
194 M. Veith, S. Mathur, N. Lecerf, V. Huch, T. Decker, H. P. Beck, W. Eiser and R. Haberkorn, *J. Sol-Gel Sci. Technol.*, 2000, **17**, 145–158.
195 M. C. Gust, N. D. Evans, L. A. Momoda and M. L. Mecartney, *J. Am. Ceram. Soc.*, 1997, **80**, 2828–2836.
196 M. Kamalasanan, N. D. Kumar and S. Chandra, *J. Appl. Phys.*, 1994, **76**, 4603–4609.
197 M. Kamalasanan, N. D. Kumar and S. Chandra, *J. Appl. Phys.*, 1993, **74**, 5679–5686.
198 S. Liu, L. Huang, W. Li, X. Liu, S. Jing, J. Li and S. O'Brien, *Nanoscale*, 2015, **7**, 11766–11776.
199 Y. Hao, X. Wang, J. Kim and L. Li, *J. Am. Ceram. Soc.*, 2014, **97**, 3434–3441.
200 F. A. Rabuffetti and R. L. Brutchey, *J. Am. Chem. Soc.*, 2012, **134**, 9475–9487.
201 B. A. Hernandez, K. S. Chang, E. R. Fisher and P. K. Dorhout, *Chem. Mater.*, 2002, **14**, 480–482.
202 C. Ahn, K. Rabe and J.-M. Triscone, *Science*, 2004, **303**, 488–491.
203 K. Terabe, M. Nakamura, S. Takekawa, K. Kitamura, S. Higuchi, Y. Gotoh and Y. Cho, *Appl. Phys. Lett.*, 2003, **82**, 433–435.
204 A. Gruverman and S. V. Kalinin, *J. Mater. Sci.*, 2006, **41**, 107–116.
205 J. Munoz-Saldana, M. J. Hoffmann and G. A. Schneider, *J. Mater. Chem.*, 2003, **18**, 1777–1786.
206 W. S. Yun, J. J. Urban, Q. Gu and H. Park, *Nano Lett.*, 2002, **2**, 447–450.
207 S. Ray, Y. V. Kolen'ko, D. Fu, R. Gallage, N. Sakamoto, T. Watanabe, M. Yoshimura and M. Itoh, *Small*, 2006, **2**, 1427–1431.
208 C.-V. Cojocaru, C. Harnagea, F. Rosei, A. Pignolet, M. A. F. Van den Boogaart and J. Brugger, *Appl. Phys. Lett.*, 2005, **86**, 183107.
209 Z. Y. Wang, A. P. Suryavanshi and M. F. Yu, *Appl. Phys. Lett.*, 2006, **89**, 082903.
210 V. K. Thakur and R. K. Gupta, *Chem. Rev.*, 2016, **116**, 4260–4317.
211 Z.-M. Dang, J.-K. Yuan, J.-W. Zha, T. Zhou, S.-T. Li and G.-H. Hu, *Prog. Mater. Sci.*, 2012, **57**, 660–723.
212 E. Tuncer, S. M. Gubański and B. Nettelblad, *J. Appl. Phys.*, 2001, **89**, 8092–8100.
213 Z.-M. Dang, Y. Shen and C.-W. Nan, *Appl. Phys. Lett.*, 2002, **81**, 4814–4816.
214 W. Lü, J. Dong and Z.-Y. Li, *Phys. Rev. B: Condens. Matter Mater. Phys.*, 2000, **63**, 033401.
215 Y. Kobayashi, T. Tanase, T. Tabata, T. Miwa and M. Konno, *J. Eur. Ceram. Soc.*, 2008, **28**, 117–122.
216 P. Barber, S. Balasubramanian, Y. Anguchamy, S. Gong, A. Wibowo, H. Gao, H. J. Ploehn and H.-C. Zur Loye, *Materials*, 2009, **2**, 1697–1733.
217 J. J. Li, J. Claude, L. E. Norena-Franco, S. Il Seok and Q. Wang, *Chem. Mater.*, 2008, **20**, 6304–6306.
218 S. S. Tripathy and A. M. Raichur, *J. Dispersion Sci. Technol.*, 2008, **29**, 230–239.
219 Z. M. Dang, H. Y. Wang and H. P. Xu, *Appl. Phys. Lett.*, 2006, **89**, 112902.

220 Z. M. Dang, J. K. Yuan, S. H. Yao and R. J. Liao, *Adv. Mater.*, 2013, **25**, 6334–6365.
221 Z. Pan, L. Yao, J. Zhai, B. Shen and H. Wang, *Compos. Sci. Technol.*, 2017, **147**, 30–38.
222 D. Kang, G. Wang, Y. Huang, P. Jiang and X. Huang, *ACS Appl. Mater. Interfaces*, 2018, **10**, 4077–4085.
223 D. He, Y. Wang, X. Chen and Y. Deng, *Composites, Part A*, 2017, **93**, 137–143.
224 Z. Pan, L. Yao, J. Zhai, D. Fu, B. Shen and H. Wang, *ACS Appl. Mater. Interfaces*, 2017, **9**, 4024–4033.
225 Y. Xie, Y. Yu, Y. Feng, W. Jiang and Z. Zhang, *ACS Appl. Mater. Interfaces*, 2017, **9**, 2995–3005.
226 H. M. Jung, J. H. Kang, S. Y. Yang, J. C. Won and Y. S. Kim, *Chem. Mater.*, 2010, **22**, 450–456.
227 C. A. Grabowski, S. P. Fillery, H. Koerner, M. Tchoul, L. Drummy, C. W. Beier, R. L. Brutchey, M. F. Durstock and R. A. Vaia, *Nanocomposites*, 2016, **2**, 117–124.
228 K. Yang, X. Huang, Y. Huang, L. Xie and P. Jiang, *Chem. Mater.*, 2013, **25**, 2327–2338.
229 Z. Li, L. A. Fredin, P. Tewari, S. A. DiBenedetto, M. T. Lanagan, M. A. Ratner and T. J. Marks, *Chem. Mater.*, 2010, **22**, 5154–5164.
230 P. Kim, N. M. Doss, J. P. Tillotson, P. J. Hotchkiss, M. J. Pan, S. R. Marder, J. Y. Li, J. P. Calame and J. W. Perry, *ACS Nano*, 2009, **3**, 2581–2592.
231 R. Popielarz, C. K. Chiang, R. Nozaki and J. Obrzut, *Macromolecules*, 2001, **34**, 5910–5915.
232 A. Biswas, I. S. Bayer, P. C. Karulkar, A. Tripathi, D. K. Avasthi, M. G. Norton and J. B. Szczech, *Appl. Phys. Lett.*, 2007, **91**, 212902.
233 L. X. Gao, Q. P. Liu, Z. W. Gao and Y. Lin, *Polym. Compos.*, 2008, **29**, 1160–1164.
234 X. L. Dou, X. L. Liu, Y. Zhang, H. Feng, J. F. Chen and S. Du, *Appl. Phys. Lett.*, 2009, **95**, 132904.
235 Z. M. Dang, Y. Q. Lin, H. P. Xu, C. Y. Shi, S. T. Li and J. B. Bai, *Adv. Funct. Mater.*, 2008, **18**, 1509–1517.
236 J. F. Scott, *Ferroelectrics*, 1998, **206**, 365–379.
237 J. T. Hu, T. W. Odom and C. M. Lieber, *Acc. Chem. Res.*, 1999, **32**, 435–445.
238 M. Ethayaraja and R. Bandyopadhyaya, *Langmuir*, 2007, **23**, 6418–6423.
239 R. L. Penn and J. F. Banfield, *Science*, 1998, **281**, 969–971.
240 J. Li, X. Hong, D. Li, K. Zhao, L. Wang, H. Z. Wang, Z. L. Du, J. H. Li, Y. B. Bai and T. J. Li, *Chem. Commun.*, 2004, 1740–1741.
241 F. D. Wang, A. G. Dong, J. W. Sun, R. Tang, H. Yu and W. E. Buhro, *Inorg. Chem.*, 2006, **45**, 7511–7521.
242 M. Kuno, *Phys. Chem. Chem. Phys.*, 2008, **10**, 620–639.
243 B. Q. Sun, E. Marx and N. C. Greenham, *Nano Lett.*, 2003, **3**, 961–963.
244 I. Gur, N. A. Fromer and A. P. Alivisatos, *J. Phys. Chem. B*, 2006, **110**, 25543–25546.
245 Y. W. Jun, H. W. Chung, J. T. Jang and J. Cheon, *J. Mater. Chem.*, 2011, **21**, 10283–10286.
246 T. Kudernac, S. B. Lei, J. Elemans and S. De Feyter, *Chem. Soc. Rev.*, 2009, **38**, 402–421.
247 J. Kim and K. B. Song, *Micron*, 2007, **38**, 409–426.
248 J. Loos, *Adv. Mater.*, 2005, **17**, 1821–1833.
249 M. S. Dresselhaus, G. Dresselhaus, R. Saito and A. Jorio, *Phys. Rep.*, 2005, **409**, 47–99.
250 M. Liess, S. Jeglinski, Z. V. Vardeny, M. Ozaki, K. Yoshino, Y. Ding and T. Barton, *Phys. Rev. B: Condens. Matter Mater. Phys.*, 1997, **56**, 15712–15724.
251 Z. Q. Tian and B. Ren, *Annu. Rev. Phys. Chem.*, 2004, **55**, 197–229.
252 V. Myroshnychenko, J. Rodriguez-Fernandez, I. Pastoriza-Santos, A. M. Funston, C. Novo, P. Mulvaney, L. M. Liz-Marzan and F. J. G. de Abajo, *Chem. Soc. Rev.*, 2008, **37**, 1792–1805.
253 M. K. Miller and R. G. Forbes, *Mater. Charact.*, 2009, **60**, 461–469.
254 T. F. Kelly and M. K. Miller, *Rev. Sci. Instrum.*, 2007, **78**, 031101.
255 S. V. Kalinin, A. N. Morozovska, L. Q. Chen and B. J. Rodriguez, *Rep. Prog. Phys.*, 2010, **73**, 056502.
256 X. H. Ji, D. Copenhaver, C. Sichmeller and X. G. Peng, *J. Am. Chem. Soc.*, 2008, **130**, 5726–5735.
257 S. Hong, J. Woo, H. Shin, J. U. Jeon, Y. E. Pak, E. L. Colla, N. Setter, E. Kim and K. No, *J. Appl. Phys.*, 2001, **89**, 1377–1386.

